AD-A271 870

ION PAGE

Public n
gathers
collects
Own re

age 1 hour per response, including the time for reviewing instructions, searching existing data sources,
e collection of information. Send comments regarding this burden estimate or any other aspect of this
/ashington Headquarters Services, Directorate for Information Operations and Reports, 1215 Jefferson
nagement and Budget, Paperwork Reduction Project (0704-0188), Washington, DC 20503.

1. AGENCY USE ONLY (Leave blank)	2. REPORT DATE 1993 June 24	3. REPORT TYPE AND DATES COVERED Final 87 SEPT 01 - 92 FEB 29

4. TITLE AND SUBTITLE	5. FUNDING NUMBERS
Microanalysis of Deformation of ~~~~ SOIL	G-AFOSR-87-0346 2302/CS

6. AUTHOR(S)

Peter Smart[1], N. Keith Tovey[2], Mark W. Hounslow[2], Xiaoling Leng[1], + Xiaohong Bai[1]

7. PERFORMING ORGANIZATION NAME(S) AND ADDRESS(ES)	8. PERFORMING ORGANIZATION REPORT NUMBER
1. Civil Engineering Department, Glasgow University, Glasgow G12 8QQ, UK. 2. School of Environmental Sciences, University of East Anglia, Norwich NR4 7TJ, UK.	.

9. SPONSORING/MONITORING AGENCY NAME(S) AND ADDRESS(ES)	10. SPONSORING/MONITORING AGENCY REPORT NUMBER
AFOSR/NA Bolling AFB DC 20332-6448 N A	AFOSR— 87-0346

11. SUPPLEMENTARY NOTES

12a. DISTRIBUTION/AVAILABILITY STATEMENT	12b. DISTRIBUTION CODE
Approved for Public Release - Distribution Unlimited	

13. ABSTRACT (Maximum 200 words)

Prediction of the behaviour of soil subject to a wide range of stresses is of interest in the design of Air Force strategic and tactical facilities and requires accurate determination of the soil properties for the environmental conditions under consideration. This study helps to link behaviour and environment through the microstructure.

New methods of image analysis were developed for electron + optical microscopy. These showed the micromechanics of deformation to be more complicated than had been imagined. Initially, all samples had horizontal preferred orientation. In drained and undrained normally-consolidated kaolin: from 0-8% strain, the specimens appeared to bed down with increased strength of anisotropy; from 8-16% strain, this tendency appeared to reverse; at about 16% strain, failure planes developed non-conformably. In over-consolidated kaolin: from 0-8% strain, there appeared to be slight bedding down, followed at once by non-conformable development of failure planes.

14. SUBJECT TERMS	15. NUMBER OF PAGES
Soil properties; micromechanics; microstructure; image analysis	5 + 87
	16. PRICE CODE

17. SECURITY CLASSIFICATION OF REPORT	18. SECURITY CLASSIFICATION OF THIS PAGE	19. SECURITY CLASSIFICATION OF ABSTRACT	20. LIMITATION OF ABSTRACT
UNCLASSIFIED	UNCLASSIFIED	UNCLASSIFIED	UL

MICROANALYSIS OF DEFORMATION OF SOIL

Final Report on AFOSR Grant 87-0346

24 June 1993

Peter Smart[1], N.Keith Tovey[2],
Mark W.Hounslow[2], Xiaoling Leng[1] and Xiaohong Bai[1]

Abstract

The behavior of soil subject to a wide range of stresses is of interest in the design of Air Force strategic and technical facilities. For an adequate facility design, it is important to determine accurately the soil properties for the loading and environmental conditions under consideration. As a result, the survivability and vulnerability of AF facilities can be better predicted.

The objective of the work reported here was to explain the mechanical properties of fine-grained soils in terms of the inter-particle and inter-aggregate effects which control them. Through this study, structures of natural soils can be better described and catalogued.

The approach was to use electron and polarizing optical microscopy to study changes in clay microstructure under different stress conditions by using different stress paths in triaxial tests.

New methods of image analysis were developed for both types of microscopy. Use of these new techniques has shown that the micromechanics of deformation are more complicated than might have been imagined. Initially, all samples had horizontal preferred orientation. In both drained and undrained normally-consolidated kaolin: from 0-8% strain, the specimens appeared to bed down with an increase in strength of anisotropy: from 8-16% strain, this tendency appeared to reverse: and, at about 16% strain, failure planes developed non-conformably. In over-consolidated kaolin: from 0-8% strain, there appeared to be very slight bedding down, followed immediately by the non-conformable development of failure planes.

1 Glasgow University, Glasgow G12 8QQ, Scotland.
2 University of East Anglia, Norwich NR4 7TJ, England.

TABLE OF CONTENTS

Contents, continued.

Tables

Figures

Contents, continued.

-----oooooOooooo-----

Chapter 1

INTRODUCTION

1.1 INTRODUCTION

The principal objective of this investigation has been to observe the changes
in microstructure of clay soils as they were deformed; in particular, the
changes during triaxial shear in samples of kaolin have been studied under
three conditions: normally consolidated drained shear; over-consolidated
drained shear; and normally consolidated undrained shear. These changes were
found to be more complex than had originally been anticipated; and the results
obtained provide a test set against which micro-mechanical computations may be
evaluated. These results are reported in Chapters 5, 6, and 7, respectively,

The changes of the microstructure during deformation were measured using new
methods of image analysis for both electron and optical microscopy which were
specially developed for this work. Both sets of methods represent considerable
advances over what was available before; and considerable interest has been
shown in this side of the work. These new methods are reported in Chapters 3
and 4.

Almost all of the scanning electron microscopy used the back-scattered mode of
observation on samples which had been impregnated and ground to reveal plane
cross-sections, the work representing one of the first major studies using
this technique.

The mechanical testing procedures are reported in Chapter 2.

Publications resulting from this project are listed in Appendix 1. Other
references are in Appendix 2. Figures and Tables are placed at the end of each
chapter.

1.2 SCHEDULE

During the first year of the research, the main emphasis was directed to con-
structing three medium pressure filter presses to a new design, instrumenting
these and the triaxial rigs, tuning the specimen preparation techniques,
investigating and standardizing the optimum conditions of observation in the
scanning electron microscope, and setting up the systems to acquire, archive
and analyze images.

The normally consolidated drained series of tests was started first; and,
apart from a short pause whilst the medium pressure filter presses were

stripped and checked. the over-consolidated drained series followed
immediately. Experimental work on this series continued until the final days
of the project. The normally consolidated undrained series of tests was con-
ducted in parallel using other apparatus.

The hardware for image archiving and analysis was expanded steadily throughout
the life of the project; and testing and tuning the new algorithms and imple-
menting further new ideas was also a continuous task.

1.3 HYPOTHESES

The materials studied were kaolin; and almost all the particles were small
flat plates. It was expected from earlier work (e.g. Smart 1966b, Smart and
Tovey 1981) that most or all of these plates would come together face-to-face
in sub-parallel arrangements to form groups called domains. It was also
expected (loc. cit.) that, when failure planes formed, the plates within the
planes would be rearranged to lie parallel to the planes. The immediate inter-
est, therefore, was how the plates and domains would behave during pre-peak
shear deformation. The initial hypotheses may be summarized as:

1. Domains grow in size and gradually turn into a preferred direction parallel
to the failure plane. Fig. 1.1.a; this hypothesis dates back to an observation
of Smart (1966c).
2. Domains act as rigid bodies and slip into closer packing without sig-
nificant change in size or internal packing, Fig. 1.1.b; this hypothesis
springs from McConnachie's (1974) study of consolidation.
3. Domains retain their general identity, orientation, and relative position,
whilst strain is accommodated by minor changes in their size accompanied by
small changes in particle packing as the latter slip over one another, Fig.
1.1.b.
4. Domains break into smaller domains; and some of the fragments rotate into
new directions, Fig. 1.1.c.

It had also been suggested (Smart 1985) that deformation increases the
anisotropy of isotropic clays and decreases the anisotropy of strongly
anisotroipc clays, i.e. that there may be a critical anisotropic state just as
there is a critical void ratio. The basis for this suggestion is summarized in
Fig. 1.2, which shows the change in anisotropy during shear deformation versus
the initial anisotropy, the measurements were made by polarizing micro-
photometry, c.f. Chapter 4. The figure also shows a regression line, which is
significant at the 7 % level. Since, the measurements were made by various
workers at various times using various apparatus, and since various clays were
tested under various conditions in various apparatus; this level of sig-
nificance is reasonably high. The implication is that deformation may be
accommodated by two different mechanisms in strongly and weakly anisotropic
clays, respectively. (The figure is based on data of Andrawes et al. 1975,
Bondarik et al. 1970, McKyes and Yong 1971, Omer 1978, Shibakova 1970, Smart
1966a, Smart and Dickson 1979.)

.4 ADMINISTRATION

The work was funded by AFOSR for four years and. including no-cost extensions. the period of study was from 1 Sep 1987 until 29 Feb 1992.

The work was split between the University of Glasgow (Glasgow) and the University of East Anglia (UEA). The work in Glasgow then attracted additional funding, and all the work there became completely integrated as indicated below.

The work had been planned by Drs.Smart and Tovey, who were responsible for supervising the work in Glasgow and UEA, respectively. The following Assistants were directly employed:

Dr.Mark W.Hounslow	UEA	RA.1.A	1 Feb 88–31 Aug 91	
Mrs.(now Dr.) Xiaoling Leng	Glasgow	RA.1.A	1 Sep 88–31 Dec 90	
Dr.Olumuyiwa A.Awoleye	Glasgow	RA.1.A	1 Jan 91–30 Apr 91	
Miss J.P.Desty	UEA	Casual	1 Apr 91–30 Jun 91	
	Glasgow*	RA.1.B	1 Jul 91–31 Oct 91	
Mrs.(now Dr.) Xiaohong Bai	Glasgow	RA.1.A	1 Oct 91–31 Dec 91	
Miss M.D.Martinez	Glasgow*	RA.1.B	1 Nov 91–29 Feb 92	

* worked at UEA.

Mrs.Leng continued to contribute to the project whilst supported by SERC from 1 Jan 1991 until 31 Dec 1992. Mrs.Bai was supported for three years by Taiyuan University of Technology. As an undergraduate, Miss Martinez had completed a study of Intensity Gradient Formulae before taking up employment.

A study of Hough transforms was undertaken for us by Mr.(now Prof.Dr.) Luciano da F.Costa and Dr.Mark B.Sandler, King's College, London. supported by FAPESP, Brazil; and further image analysis was undertaken by Mr.Daisheng Luo and Dr.James E.S.MacLeod, Department of Electrical Engineering, Glasgow. supported by the University of Sichuan.

Babcock Power plc, who had already checked the design calculations for the medium pressure filter presses, also gave some specialized help in their fabrication. SERC Transputer Initative provided additional image analysis facilities in Glasgow; to which RSRE contributed some software.

Interim Reports were submitted on 26 Oct 1988, 26 Oct 1989, 8 Jul 1990 (Continuation Proposal), and 28 Jan 1991. Drs.Smart and Tovey attended AFOSR Contractors' Meeting, Boston, 1987. Dr.Smart made presentations to AFOSR, Washington. and AF Geotechnical Laboratory, Albuquerque, 1990: Dr.Tovey made a presentation to AF Geotechnical Laboratory, Albuquerque, 1990. Dr.Smart attended AFOSR Contractors' Meeting, Albuquerque, 1992. Dr.Leng attended AFOSR Contractors' Meeting, Boston, 1993.

As a result of the work funded by AFOSR, Drs.Smart, Tovey, and Hounslow have received subsequent funding from either SERC or NERC; Drs.da Costa and Bai expect to receive support from their national bodies; and Dr.Leng has put forward equally important proposals.

-----ooooooOooooo-----
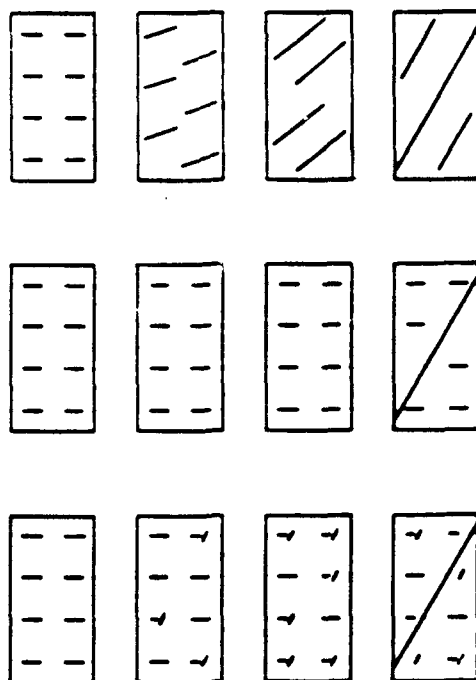
Fig. 1.1 Hypothetical modes of deformation: two-dimensional idealization.
        Left: Original structure.   Right: At failure.
        a. Top: Hypothesis 1. Domains grow larger and re-align.
        b. Center: Hypothesis 2. Domains slip into closer packing, or
                        Hypothesis 3. Particles slip within domains.
        c. Bottom: Hypothesis 4. Domains break into smaller domains.
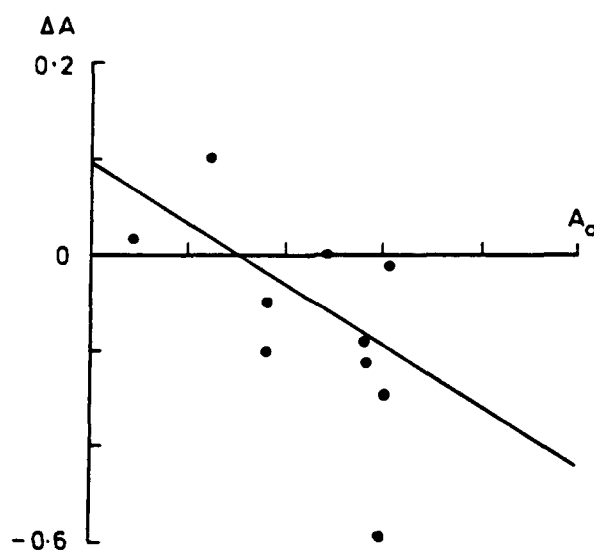
Fig. 1.2 Change of Anisotropy vs. Initial Anisotropy during shear deformation
                of clay (from Smart 1993).

GEOTECHNICAL PROCEDURES

2.1 INTRODUCTION

This Chapter reports the preparation and procedures used for the three series of triaxial tests for which microstructural measurements were obtained: normally consolidated drained shear; over consolidated drained shear; and normally consolidated undrained shear.

Each series of microstructural measurements required replicate samples at various stages of deformation; and, in order to produce series of samples which were homogeneous (i.e. having the same internal microstructure and properties) and repeatable (i.e. all of each series the same). clay was mixed to a slurry. consolidated uniaxially in specially designed filter presses. reduced to standard size. and consolidated triaxially. The details of this mechanical preparation and of the triaxial testing itself are given below. The stress-strain curves for the three main series of tests will be shown with the other main results in Chapters 5, 6, and 7.

2.2 MATERIALS

The clay used in all the tests was Speswhite Kaolin obtained from English Clays Lovering and Pochin Ltd. The material had been hydraulically mined from weathered granite near St.Austell, Cornwall, after which it had been screened and classified using various physical and chemical treatments which did not include grinding. One batch was used for the drained tests. and a second and nominally identical batch was used for the undrained tests, see Table 2.1. X-ray diffraction showed the material to be predominately kaolinite with less than 5 % quartz and illite. Some peaks were diffuse. suggesting the kaolinite to be slightly disordered. X-ray mapping indicated that the potassium and iron impurities were mainly associated with the larger particles. Electron microscopy confirmed the platy nature of the particles.

2.3 FILTER PRESSES

2.3.1   Introduction

This Section describes the medium and low pressure filter presses which were used for the drained and undrained samples, respectively; details of their use are in the next Section.

2.3.2   Medium pressure filter presses

The drained samples were prepared in a set of three medium pressure filter presses illustrated in Fig. 2.1. Saturated clay is contained in the upper part of a double acting piston-cylinder arrangement, and water (or oil) under pressure is supplied under the piston. Porous stones above and below the clay permit the pore water to escape up out of the top cap and down through the piston rod, which is hollow. Flexible tubing conducts this water to a suitable receptacle, which must be above the level of the top cap to prevent the hollow piston rod from drying out. U-rings around the porous stones prevent the slurry from escaping past the stones.

The general procedure was as follows. First, the top cap was removed. the lower part of the cylinder was deaired through an air vent plug in the piston. the piston was lowered as far as possible. the lower porous stone fitted. the sides of the cylinder greased. a filter paper placed over the lower porous stone. and the cylinder carefully filled with slurry. Then, the slurry was leveled using a special scraper, the top filter paper and porous stone fitted. an insert laid over these, the top cap replaced, and pressure admitted, see below.   When the cake was ready, the inlet valve was shut, the top cap removed, and the cake extruded by careful use of the inlet valve.

These filter presses were designed to produce filter cakes 4 inches (100 mm) high and 5 inches (125 mm) diameter from slurries which were not unduly aggressive and which were free from strongly abrasive constituents: there was provision to add a protective layer 0.02 inches thick within the bore should this have become necessary. The material is Type 316 stainless steel (see BS 970: 1970).

The base plate contains a specially designed non-return valve fitted at the high pressure inlet, a safety valve, and a port for a pressure transducer. Movement of the piston can be monitored from the piston rod.

The stress calculations had been made in accordance with BS 5500: 1985 as Category 3 constructions. i.e. the welds would be accepted on the basis of visual inspection. taking the operating pressure as 250 psi (1725 kPa) for an air-water pressure source and 500 psi (3450 kPa) for pure hydraulic pressure. The corresponding standard test pressure would then have been 1000 psi. However. both the original source of material and the original arrangements for welding had to be changed at the last moment, so it was decided to test at 600 psi. The maximum operating pressure, therefore, was 150 psi (1035 kPa), which was just above the maximum pressure available. It is thought that, if a high pressure source were available, and if the presses could be run in an enclosed environment. then, by increasing the dimensions, applying full inspection and improving the top seal, a working pressure of at least 1000 psi could be obtained with this design of filter press.

In making the stress calculations, some difficulty was experienced in deciding the proper uplift pressure on the top cap. The usual method of calculation assumes leakage from the bore radially outwards along the gasket. taking full internal pressure at the bore, and assuming that this decreases uniformly until it is completely relieved at the pitch radius of the bolts. This assumption is not quite safe for a slurry. which might be extruded slowly enough for it to dry out and harden at or beyond the pitch radius. so that full pressure

could build up to a greater extent than is generally assumed. Consequently, the underside of the top cap was relieved with an upward-sloping cut in an attempt to control the behavior of any slurry which was extruded. No extrusion of slurry was reported during operation; but there was leakage during the proving tests, and these were completed by tightening the bolts to a greater torque than had been calculated. It is not known whether the method of calculation was faulty (although it was taken from BS 5500: 1985 and had been checked independently), or whether the material properties of the gasket had been wrongly estimated, or whether the relief had permitted the top cap to flex and rise.

The operating temperature was specified as 7 to 50 degrees Centigrade.

2.3.3 Low pressure filter presses

The undrained samples were prepared in a set of three low pressure filter presses of the same basic design as the medium pressure filter presses, but made from quarter-inch thick plastic. These presses had been used earlier by Dickson and Smart (1979), and no trouble was experienced with them apart from occasional minor breakages due to the age of the plastic.

2.4 UNIAXIAL CONSOLIDATION

For the drained samples, approximately 2 kg of kaolin powder was mixed with 2.8 litres of distilled water (140 % moisture content, 3.0 Liquidity Index). The slurry was whisked until smooth in a large food mixer, de-aired by vigorous shaking under low vacuum, and carefully transferred to the medium pressure filter presses. Starting from a small value, the pressure was doubled daily up to 700 kPa. During the uniaxial consolidation, the samples decreased in height from 320 mm to 140 mm, approximately, (56 % strain).

To make one undrained sample, 2.5 kg of kaolin powder was mixed with 3 kg of de-aired water (120 % moisture content, 2.56 liquidity index). The slurry was mixed in a Z-bladed mixer for 2 hours under a vacuum of approximately 500 mm Hg. The slurry was then consolidated uniaxially in the low pressure filter presses, see Table 2.2. The friction in each press had been estimated by noting the pressure required to move the piston when the press was empty, and the pressures applied were increased accordingly.

In addition to the main series of tests, an additional series of 8 normally consolidated drained samples was made in which everything was done in exactly the same way as in the main series, except that a gauze was drawn up through the slurry after initial placement in the filter press with a view to improving the homogeneity of the samples. However, the microstructural examination showed that the wakes of the wires persisted in the samples throughout uniaxial consolidation, triaxial consolidation, and shear deformation. It is understood that a similar result had been obtained elsewhere, but details are lacking. Towards the end of the study, one of the filter presses was extended and filled by sedimentation: this appeared to be a more promising method, but it is slower, so more presses would be required.

2.5 TRIAXIAL CONSOLIDATION

One standard triaxial test sample 3 inches high x 1.5 inches diameter (75 mm x 37 mm) was cut from each filter cake. Although 6 samples were cut at inclinations between 30° and 90°; all of the main series of samples were vertically.

Standard triaxial testing apparatus was used.

For the normally consolidated drained samples, drainage was from the top, with pore pressure measurement at the bottom. No back pressure was used. because obtaining the highest possible effective pressure was more important than achieving perfect saturation. The cell pressure was increased by stages to 700 kPa.

The procedure for the over-consolidated drained samples followed that for the normally consolidated samples. except that the cell pressure was finally reduced from 700 kPa to 100 kPa.

For the undrained samples, drainage was from the bottom. with a plain plastic cap at the top. A back pressure of 0.5 bar was applied. The cell pressures are in Table 2.3.

2.6 TRIAXIAL DEFORMATION

For the drained samples, the strain rate was chosen at approximately 5 % per day. so that the normally consolidated samples would fail after 4 days shearing, approximately. Despite this slow strain rate, the pore pressures sometimes rose to 15 kPa at 4 % strain approximately, falling thereafter.

For the undrained samples, a strain rate of 0.15 mm/min was chosen to limit the effects of time lag in the pore pressure measuring system. equalization of non-uniform pore pressures. and rate dependent effects.

2.7 RECOVERY OF THE SAMPLES

The measurements of the microstructure were destructive, so it was necessary to stop the triaxial deformation at various strains, in order that these measurements could be made. Control samples at 0 % strain were obtained by setting up samples as if they were to be sheared. omitting all shear deformation. and recovering the samples immediately after the triaxial consolidation stage.

After stopping the triaxial deformation and releasing the axial load, the cell and pore pressures were reduced slowly, after which the samples were removed from the triaxial machines. They were then sliced longitudinally in half with a cheesewire along the plane of symmetry if one had formed. One half of the sample was used to determine the moisture content, and the other half was prepared for microstructural examination as described in the next Chapter.

-----ooooo0ooooo-----
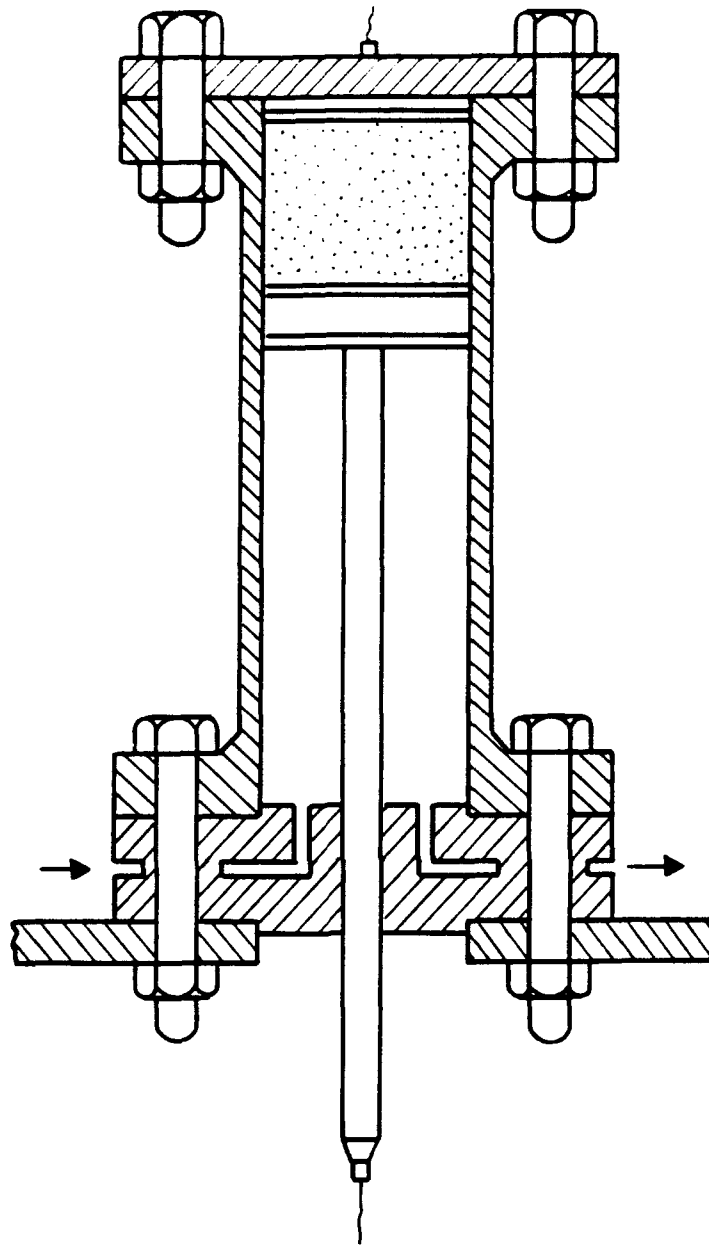
Fig. 2.1 Medium pressure filter press.

Table 2.1   Properties of Speswhite Kaolin

	Drained	Undrained	Pure	
SiO_2	47.0	46.2	46.6	% by wt
Al_2O_3	37.8	38.7	39.5	% by wt
Fe_2O_3	0.6	0.56	0.0	% by wt
TiO_2		0.09		% by wt
CaO		0.20		% by wt
MgO		0.20		% by wt
K_2O	)1.2	1.01		% by wt
Na_2O	)	0.07		% by wt
H_2O*	13.1	13.14	14.0	% by wt
pH		5.0		
finer than 10 μm		99.5		% by wt
finer than 2 μm		78-83		% by wt
mean grain size	0.7			μm
specific gravity	2.6	2.62		
liquid limit	69	67.5		%
plastic limit	34	37.0		%
plasticity index	35	32.5		%
refractive index	1.56	1.56		

* or loss on ignition.

Table 2.2   Pressures applied, low pressure filter presses, bar

Nominal	Press 1	Press 2	Press 3	hours
0.125	0.245	0.245	0.225	24
0.250	0.370	0.370	0.350	24
0.500	0.620	0.620	0.600	24
1.000	1.120	1.120	1.100	168

Table 2.3   Cell pressures applied, undrained samples

pressure, bar	1	2	4	7
duration, day	1	1	1	2

ELECTRON MICROSCOPY

3.1 INTRODUCTION

This Chapter reports the methods of electron microscopy and of image analysis which were used to study the structures of the samples which had been deformed in the triaxial tests. Virtually all of the electron microscope observations were made using the back-scattered mode, which was itself relatively new, so some improvements in preparation techniques had to be made for it. The automatic methods of image analysis which were used to extract quantitative information from the electron micrographs were almost entirely novel; and the development and testing of these new methods was a major task. These methods are discussed in turn below: Fig. 3.1 shows a typical scanning electron micrograph; and Figs. 3.2 and 3.3 summarize the principal analyses made in Glasgow and UEA, respectively.

3.2 SCANNING ELECTRON MICROSCOPY

3.2.1   Introduction

The first steps are to prepare the samples for scanning electron microscopy, to examine them in the microscope, and to digitize the electron micrographs. This Section describes these steps.

3.2.2   Impregnation

At the end of each triaxial test, the samples were first sliced into two halves longitudinally, as described in the last Chapter. Then, the samples were impregnated following the methods described by Smart and Tovey (1982).

The usual procedure for the drained tests was to cut sub-samples sized 20 mm square by 10 mm thick. These were placed face down in a foil dish and immersed directly in acetone. The acetone was changed several times at 24 hour intervals. When all water had been removed by the acetone, a mixture of Araldite AY18, Hardener HZ18, and 1-2 % di-n-butyl phthalate, diluted with an equal volume of acetone, was introduced into the sample. The acetone was allowed to evaporate slowly from the mixture, which was topped up as necessary to keep the sample submerged; then the resin was left for 2-3 days to harden. Finally, it was cured at 40 degrees C.

For the undrained tests, complete half samples were usually impregnated. These were placed face down in a small dish and packed round with sand; the small dish was then placed in a larger dish fitted with a drain. Both dishes were carefully flooded with 25 % acetone in water; then, at intervals of one or two days, the outer dish was drained and refilled in turn with 50 %, 75 % and 100

% acetone. At least three changes of 100 % acetone were used. When all the
water had been removed by the acetone. a mixture of 100 parts Vestopal W. 1
part initiator, 0.5 parts activator, (by weight), and 200-300 parts acetone
(by volume), was added to the small dish. The acetone was allowed to evaporate
slowly from the mixture, which was topped up as necessary to keep the sample
submerged; then the resin was hardened at room temperature. Finally, it was
cured at 60°C for 48 hours.

Especially during the early stages of the study, ethanol and methanol were
used to remove the pore water. and then acetone was used to replace the
methanol.

3.2.3   Grinding

When the impregnated samples had hardened, 2 mm was ground off the face to
remove the disturbed zone. Then sub-samples were cut, ground and polished to
prepare a block for observation in the scanning electron microscope. The final
surface should be flat and free not only from scratches and pluck marks but
also from smearing. Conventional methods of grinding thin sections for optical
microscopy do often leave a thin smeared zone at the surface; and the require-
ments for scanning electron microscopy are more demanding. The success of this
project owes much to the skill and patience of Mr.I.Marshall. who was
responsible for improving the final preparation technique and preparing the
blocks* The samples were ground successively on emery cloth Nos. 240 and 600
lubricated by water and 6 μm and 1μm diamond lubricated with Hyprez fluid
(supplied by Engis Ltd.).

3.2.4   Coating

The polished blocks were mounted on specimen stubs using silver dag and then
coated with carbon.

3.2.5   Observation

For the drained samples. almost all of the scanning electron microscopy was
done using the Hitachi S-4.0 SEM in the School of Environmental Sciences in
UEA. Digitized images were acquired by a Link Analytical interface (which is
also capable of X-ray micro-analysis). converted to Semper format by a PC. and
fed into the image archiving system described below. The whole route from SEM
through to the archive is hard-wired. For the undrained samples. electron
micrographs were digitized and recorded by a computer which is an integral
part of the Cambridge 360 SEM in Glasgow; they were then passed to a second
computer which is close-coupled to the first, where they were stored
temporarily on hard disk. At the end of a session, the micrographs were down-
loaded to a half-inch magnetic tape, which can hold about 250 micrographs and
forms the primary archive. Duplicate copies of about 5% of the images were
stored on floppy discs for the Nimbus image analyzer.

The main series of micrographs were obtained using the back-scattered mode:
some additional micrographs were obtained using the secondary electron mode
for comparative purposes. Untilted samples were used. This technique presents

---

* Mr. A.A. Burnett prepared the blocks in Glasgow.

a cross-sectional view of the sample, which simplifies the image analysis.
Contrast in the back-scattered mode arises primarily from atomic number con-
trast, so that particles in general appear bright against a dark background of
resin-filled pores. Fig. 3.1. The incident electrons penetrate some distance
into the sample, and there is some spreading of electrons within the sample
before they escape back to the collector. Thus, some particles which are
actually below the true surface may be seen more or less faintly; and also
there is some softening of the contrast.

All the digitized micrographs (images) taken for this study have 512 rows of
512 pixels each and are digitized to 256 gray levels. Usually the images were
taken from a vertical face aligned as far as possible with a plane of symmetry
in the sample. In UEA, 34 images were usually taken from each sample as fol-
lows:

number of images	nominal magnification	image width mm
24	x2000	0.056
6	x1000	0.113
4	x500	0.225

In Glasgow, 26 images were usually taken from each sample as follows:

number of images	nominal magnification	image width mm
25	x4000	0.025
1	x800	0.120

The main analyses were made using the x2000 and x4000 images, with the others
held in reserve. As far as possible, the images in UEA were spaced at 1 mm
centers in two traverses of 12 images, one being horizontal and the other
vertical, the images in Glasgow were spaced at 2 mm centers in a 5 x 5 array.
In UEA, with the exception of some of the earlier samples, the contrast was
standardized at the start of each batch of images by observing a specially
prepared block, which contained large areas of clear Araldite and large quartz
grains. The gray level on the Araldite was adjusted to 0, and that on the
quartz to 221. Images of the areas used for this adjustment were also
digitized.

3.3 IMAGE ANALYSIS

3.3.1   Introduction

At the start of this project, both universities installed PC-based versions of
the Semper image analysis system; for convenience, the PC in Glasgow is called
Nimbus. These effectively replaced the main-frame and Quantimet systems which
had been in use previously. By now, the original installations have been pro-
gressively improved. In Glasgow, additional support from SERC led to the use
of transputers. In UEA, net-worked PCs and a Sun workstation have been added,
all running Semper.

3.3.2   Image archives

Each digitized image required 0.25 MB storage space. In round terms, each of the three major experiments used 40 samples and 25 images from each, i.e. 1000 SEM images per experiment, excluding all subsidiary and supporting images and experiments. Each of these experiments also used about 1000 optical images. In addition, there has been a necessity to store processed images ready for subsequent stages of analysis; and the data bank of raw results is also large.

The image analysis facility in UEA by now consists of an network of 80286, 80386, and 80486 PCs, all connected by D-link, so that each computer can read the hard disk of any other, Fig. 3.4. The network also contains a Sun workstation, a Gigabyte hard disk, optical disk reader, and tape drive. The SEM itself is connected to the net as indicated above; and there is another connection to the University's main network and central Vax computer. Thence, there is a JANET connection to Glasgow. These facilities have been expanded gradually, and there have been some changes in practice as new facilities were added. In general, images are kept on the Gigabyte hard disk and copied from there to the computers when required. Duplicate copies are kept in the archiving system connected to the Vax; and third copies of a large proportion of the collection have been stored on optical disks or magnetic tapes. The archiving system has not been trouble free, and from our experience, we are inclined to recommend that important data should be held in triplicate. All the images originating from UEA are stored in Semper format.

Early in the project, some images were transferred from UEA to Glasgow by electronic transfer from UEA's Vax to Glasgow's ICL mainframe. However, for small quantities of representative or special images, it was more convenient to send floppy disks by post; and for large quantities, images were copied from UEA's Vax, onto Vax-type tapes, sent to Glasgow, read into a Vax there, and transferred thence to the Meiko computer. Images sent from UEA are stored in home/psmart/uea.

In Glasgow, when each tape from the SEM is full, the Computing Service copies it via a Sun workstation and Ethernet to the CPU of the Meiko (which is an embedded Sun board), and thence to the Meiko's main disk, where they are stored in directories called home/psmart/bai. psmart is used for archiving only, and all workers in the group have read-only access to it. A separate sub-directory, /tapeN, where N is a single-digit number, holds all the images from one half-inch tape. Due to peculiarities in the file-handling systems, the Glaswegian micrographs were reordered before being down-loaded to the half-inch tapes, and the original file name was moved into the file; therefore, files are given new names, /fileDDD, where DDD is a three digit number starting at 001. The format then becomes: header (file name) 512 bytes; header (original) 512 bytes; 512 lines x 512 bytes each. All the files from one tape are then inspected; the images are presented on one screen at about 4 second intervals, whilst the new and original file names are shown on another screen and listed to file. The list enables the images to be reordered correctly by logging onto psmart and using a home-made Unix command to swap pairs of file numbers; and the visual presentation enables bad images to be spotted and moved to the ends of the batches containing them. After the final reordering, the scanning program is used again to list the names and numbers of the images to a catalogue; comments are edited in; and the catalogue is saved. During analysis from a Sun workstation, two windows can be opened, both can log onto

different sets of transputers. one of which can do the work. whilst the other
reads the catalogue. Fig. 3.5.

3.3.3   Image analysis hardware and software

In UEA, the image analysis hardware consists of the net-worked computers
described above. Most of the PCs are equipped with frame stores and secondary
monitors to display the images: the Semper software image processing routines
can be run on any of these PCs. The Sun workstation has its own Semper soft-
ware and uses a window on its main monitor for displaying images. There is a
considerable difference in processing speed between the fastest and the
slowest of these computers: and this is taken into account when allocating
work to them. The Sun is capable of running several processes in parallel: and
it has generally proved to be faster (in terms which include operator time) to
place several medium sized standard jobs on it rather than one very large one.

All image analysis in UEA is done using the Semper system. Apart from interac-
tive use for occasional tasks. programs are written in the Semper language and
left to run unattended. perhaps for 24 hours or overnight. There are facili-
ties in the Semper system both to call Fortran sub-routines which are external
to the Semper package proper or to import these sub-routines into the Semper
package as extra 'verbs' (commands). The work has involved a combination of
all these methods of operation.

A different course of development was followed at Glasgow. During the first
year of the project. an 80386 PC with Semper frame-store was installed. This
was used for display; but, as a matter of convenience. external Fortran
programs were used for the novel algorithms which were being developed. These
new algorithms were running very slowly; and there was a memory restriction
even though the code had been written to read-and-process line-by-line. At
this stage. SERC loaned another PC with a T4 transputer. and the improved
speed and simplified management of memory provided an excellent development
environment. This was upgraded. first to 4 T4 transputers, then to 6 T8
transputers with a second monitor. and finally to the Meiko computer (which is
a University central facility). Full advantage has not yet been taken of the
Meiko: because the main programs written for the 6-transputer system were fast
enough. and so priority has been given to algorithm development. In practice.
although the IPLIB image analysis package is available, all code used for the
Transputers has been specially written. because so much of it was novel.

The general arrangement of (our part of) the Meiko is shown in Fig. 3.5. The
'top' or 'master' transputer communicates with the terminal, reads images from
disk, passes these and commands to the other transputers, receives results,
and combines these results as necessary. The four central transputers,
'workers'. each receive one-quarter of the image and process that; inter-
mediate results are swapped between these processors as necessary. The 'dis-
play' transputer presents images on the secondary monitor; it may also do some
processing of the recombined computed images. Each transputer has 4 MB RAM,
which is barely enough. At one time, separate versions of the programs were
maintained to analyze either one or a series of micrographs; but most of the
single-image programs are being phased out. Future programs will probably con-
tain pre-processing transputers before the workers, and post-processing
transputers after them; although this will increase the starting up time,

adding these extra transducers into the pipe will not affect the rate of processing. The Meiko is now usually run from a Sun workstation, so it is possible to log onto two sets of transputers at once, which helps when developing parallel programs, reading the file catalogue, etc.

After returning SERC's PC and transputers, Nimbus was fitted with a single T8 transputer and a third monitor, see Fig. 3.6. At present, there is a choice of using Semper or the transputer; in theory, by using Windows, both systems could be used at once. New programs are usually written on the transputer, for which there are Occam, Fortran, and C compilers; but most work uses both systems. All of the optical microscopy reported in the next chapter used this PC. Images were digitized by Semper using a thermionic camera, which was preferred to avoid the problems of re-digitizing which arise unless special precautions are taken with CCD cameras; and the calculations were made by the transputer. These images were stored on floppy disks after the calculations had been completed.

3.4 IMAGE RECTIFICATION

3.4.1 Introduction

Before analyzing the digitized electron micrographs, a number of steps were taken to rectify defects in them. These steps are discussed in turn below.

3.4.2 Impregnation and grinding defects

Occasionally, during scanning electron microscopy, the location of the recorded area was changed slightly to avoid patches where either the impregnation or the grinding was defective.

3.4.3 Charging

Occasionally, during scanning electron microscopy, some areas of the samples charged up and became brighter than they should have been. These areas were few and small; moreover, both of the principal methods of analysis used here, i.e. intensity gradient methods and the method used to obtain black-and-white images, minimize the effect of charging. Therefore, no special measures were employed.

3.4.4 Mineralogical variations

A few of the clay particles appeared brighter than average; this was attributed to differences in composition such as an increase in iron content. The effect was small and rare and no special measures were employed.

3.4.5   Over-run

Occasionally, some of the particles looked as if they had very small holes within them. This was attributed to malfunction of the analogue-to-digital converter: i.e. pixels which should have been (*maxgrey* + *n*) were recorded as *n*. In other words, instead of being digitized to 8 bits, the intensities had been digitized to 9 bits, and the most significant bit had been discarded. A short Semper program was written to patch these holes empirically; and a second program was used to check whether this had been successful.

3.4.6   Electrical interference

During the course of the investigation, it became apparent that the electrical circuits within the scanning electron microscope and digitizer were being affected by electrical interference, either from within the instruments, or from nearby apparatus, or from the power supplies. This interference was discovered when Fourier transforms of images of plain resin blocks were inspected: the power spectrum was found to have large peaks, which were unrelated to the structureless blocks, and which usually occurred in the same places. These peaks were also found in the power spectra of the micrographs of the samples proper. Similar effects have since been reported to us by other image analysts.

To mitigate this artifact, the power spectrum was searched, and the peaks were located and masked out. The rectified image was then recovered by taking the inverse Fourier transform. In practice, the power spectrum has a natural peak at its center; so the masking was confined to the outer part of the power spectrum.

This operation was combined with a deconvolution of the point spread function, see Wiener filtering below.

3.4.7   Signal-to-noise ratio

Close inspection of the electron micrographs showed that they were granulated very finely due to high frequency noise. This noise was measured for each batch of micrographs by finding the variance, v_n, of the gray levels in clear areas of the control micrographs which had been taken on the plain resin blocks.

To obtain the signal-to-noise ratio of an ordinary micrograph, the variance, v_t, of its gray levels was found. Thence, the signal to noise ratio, s_r, was calculated from:

$$s_r = \mathrm{sqrt}(\ (v_t - v_n)\ /\ v_n\ ) \qquad\qquad (3.1).$$

3.4.8   Point spread function

When scanning electron micrographs are being formed, an electron beam is directed at the sample. Some of the incident electrons are reflected as backscattered electrons; some liberate secondary electrons of low energy; and some

ire absorbed. In the back-scattered mode of operation. both the back-scattered
and the secondary electrons are collected and contribute to the intensity.
Although the incident beam is of very small diameter. the electrons in it
enter the sample and are spread: so the received signal contains contributions
from regions around the theoretical point of contact (Smart and Tovey, 1982.
Chapter 6). This effect leads to a blurring of the image and some loss of con-
trast. The mathematical description of the blurring is known as the optical
transfer function or as the point spread function. For an electron microscope.
it is expected that the shape is Gaussian (Lewis and Sakrison, 1975; Guan and
Ward. 1989).

The point spread function was measured from electron micrographs of small par-
ticles of dirt which were seen on the plain resin blocks. The particles
selected were small enough to be effectively point sources. Their intensity
profiles were measured. averaged rotationally about the peak positions. and
then averaged collectively. A Gaussian profile was fitted to this final
average profile. This gave an overall spread diameter of 11.4 pixels at x2000
magnification, corresponding to a Gaussian rms radius of 11.4/8 pixels or
0.156 microns.

3.4.9   Wiener filtering

After masking the electrical interference from the Fourier transform of an
image. Wiener filtering was used to sharpen the image by removing the blur:

$$F(u,v) = G(u,v) \ H*(u,v) \ / \ \{mod(H(u,v)^2) + 1/s_r^2\} \qquad (3.2),$$

where $G(u,v)$ is the masked power spectrum of the image;
       $H(u,v)$ is the power spectrum of the point spread function;
      $H*(u,v)$ is the complex conjugate of the point spread function.

The rectified image was recovered from $F(u,v)$ by taking the inverse transform.
An example is shown in Fig.3.7. Fast Fourier transforms were used throughout
these calculations.

(Further details are given by: Stroke et al.. 1971. who used optical process-
ing; Lewis and Sakrison, 1975; Bates and McDonnel, 1986; Gonzalez and Wintz,
1987; Guan and Ward, 1989.)

3.4.10   Missing scan lines

Some of the electron micrographs taken in Glasgow were found to contain miss-
ing scan lines. During the inspection mentioned above, for each image, the sum
of the gray levels is calculated for each line of the file including the two
headers. Confidence limits for these sums are set at three standard deviations
from the mean. In our case, the headers should lie outside the limits: so the
program shows (a) how many header lines lie within the limits; and (b) how
many ordinary lines lie outside them. Suspect images are re-examined one-by-
one and removed if necessary. At the time of writing, some of these images
have also been found to have 'jumbled' scan lines, which are found during the
visual examination; and we are considering using similar confidence limits for
'mean chord lengths' to search for these.

3.5 INTENSITY GRADIENT ANALYSIS

The clay used in these studies consists almost entirely of flat plates. The electron micrographs show a planar cross-section through the material, in which most of the plates appear as thick lines. Apart from a few areas where the plates are jumbled together randomly, there is generally strong local preferred orientation; many of the micrographs also show an overall preferred orientation. Intensity gradient analysis was used to measure both the strength and direction of this overall preferred orientation.

In an electron micrograph showing bright particles against a dark background, the intensity gradient, grad I, is a vector, whose value is high at the edges of the particles, and whose direction is perpendicular to those edges. The analysis starts by calculating the intensity gradient:

$$U = \text{grad } I \qquad\qquad (3.3).$$

$$U = \text{mod grad } I \qquad\qquad (3.4).$$

$$A = \text{arg grad } I \qquad\qquad (3.5).$$

As a general rule, the 20.14-formula is used, because this formula appears to suit the work in hand. The formula uses the 20 nearest pixels and was derived from a least squares fit for the first 14 differential coefficients in a two dimensional Taylor series (Smart and Tovey, 1988a). To avoid cases close to A = atan (0/0), pixels are labelled 'undecided' if U is smaller than an arbitrary limit. The default value for this limit is 3 pixels, where, for convenience, the term 'pixel' is used as a measure of length; but higher values may sometimes be needed.

The results are often summarized in an unweighted rosette frequency histogram plot of orientation for each image, Fig. 3.8.a. Earlier studies using this approach often gave spiky rosettes; but a combination of a better digitization, a more sophisticated formula, better choice of the limit for the undecided case, and a more appropriate histogram bin size, has resulted in reasonably smooth rosettes. The best fitting ellipse was found for the rosette for each image, and an Index of Anisotropy, I_A, found from:

$$I_A = (\textit{major axis} - \textit{minor axis})/ \textit{minor axis} \qquad (3.6).$$

3.6 MAPPING BY TOP-CONTOURING

The clay structure consisted mainly of groups of particles showing strong local preferred orientation which are called domains here. There were also some random clusters of plates. Two new algorithms were developed to map these features ready for measurement.

The first of these algorithms to be developed maps domains and random clusters by first encoding A into a limited number of directions, and then smoothing the encoded image (Smart et al. 1988). Typically, 4, 8, or 12 directions are used. The first successful implementation used a T414 transputer in a PC; but the main development used six T800 transputers in a PC. This algorithm has now been moved to the Meiko without change apart from some simplification and the

use of a different graphics board. A Semper version has been written: and this is now available via Synoptics Ltd.

The encoded image is smoothed by selecting the most popular direction from the histogram of encoded angles within a large circular uniform filter (see Appendix 3.1). The filter is typically of 20 pixels radius. Reflection is used to avoid leaving unprocessed borders. If more than an arbitrary number of pixels within the filter have undecided angles, then the pixel in the map is labelled undecided: by default, the code uses the radius of the filter as this limit, and, in the current work, it is rarely if ever exceeded. The pixel in the map is labelled 'random' if the difference between the maximum and the mean of the histogram is below a limit, EXC %, which may be set arbitrarily, but which is by default set by:

EXC = 200.*SQRT(-LOG(PROB)/NIF)*NOD*SIN(PI/NOD) / PI   (3.7),

where NOD is the number of directions, NIF is the number of pixels in the filter, and PROB is the probability.

The difference between the maximum and the mean is thought to be more robust than the difference between the maximum and the minimum in cases in which only one direction differs from the others. A bias may arise if the histogram has two or more equal maxima, and the present code contains one of several algorithms which were considered to minimize this bias.

As far as we know, no similar analysis had ever been reported: so some time was spent in testing the values of the various limits, in deciding the radius of the filter and how many directions to use, and in deciding the magnification and the other instrumental settings on the microscope.

The most difficult parameter to fix was the radius of the filter, because there was originally thought to be no predetermined optimum size for it. The only rule found was: to smooth away features of a given size, use a filter of a slightly larger size. In the main series of micrographs to be analyzed, there were features of all sizes, so the final choice of radius for the filter was made on the basis of visual assessment by a panel of experienced microscopists. The nominal value chosen was 19 pixels: but the code increases the nominal radius by 0.4 pixels to improve the circularity of filters less than 8 pixels radius. Subsequently, a modified chi-square test was used to test this choice. The image was mapped at various radii: the areas were averaged over all radii: and the sum of the squares of the errors of the original areas from the corresponding averages was treated as an error function. The result for a typical image is in Fig. 3.9.a. The choice of 19 pixels was also supported by some consistency ratio results and by a preliminary study of the semi-variogram, both of which are discussed below.

This algorithm, which was called topcontouring by its author, was a great step forward in the field of soil microstructural analysis. It is faster than the alternative method described in the next Section.

3.7   CONSISTENCY RATIO MAPPING

3.7.1   Consistency ratio mapping per se

Consistency ratio mapping is the second of the new algorithms to be developed for mapping clay structures. It is more accurate than topcontouring, slightly slower, and requires more memory; it maps domains and random clusters by first smoothing the vector field, U, then testing for randomness and segmenting the oriented areas into a limited number of equally spaced directions (Smart, 1990, Smart & Leng, 1991). An example is shown in Fig.3.1. The equations are:

$$X = \Sigma\ U \cos 2A \qquad\qquad (3.8).$$

$$Y = \Sigma\ U \sin 2A \qquad\qquad (3.9).$$

$$S = \Sigma\ U \qquad\qquad\qquad (3.10).$$

$$R = \sqrt{(X^2 + Y^2)} \qquad\qquad (3.11).$$

$$C = R/S \qquad\qquad\qquad (3.12).$$

$$T = \tfrac{1}{2} \operatorname{atan}\ (Y/X) \qquad\qquad (3.13).$$

C is called the consistency ratio (see Smart and Tovey, 1982, Section 12.1.4 for a review). If S is small, T must be labelled undecided and mapped accordingly. If:

$$C\ <\ \sqrt{\{\ (1/N)\ \ln\ (1/P)\ \}} \qquad\qquad (3.14),$$

where N is the number of (decided) pixels in the filter, and P is the probability of obtaining a greater consistency ratio by chance, then the pixel is mapped as random.

For analyzing clay structure, the angle is multiplied by 2 at the start of the calculation and divided by 2 at the end, because the small linear features have two-fold symmetry. (Smart and Leng, 1991, have extended the concept to chromatic mapping, which lacks this symmetry.)

In addition to making the calculations within the smoothing filter, they were also made for each image and for each sample to provide an alternative measure of preferred orientation.

Further, calculating consistency ratio as a function of size of filter showed that it fell rapidly at first as the size of the filter increased, then it appeared to level off at a level representative of the image as a whole. In Fig.3.9.b, which is for an image of nominal magnification of x500, the breakpoint seems to occur at about 5 pixels radius, corresponding to 20 pixels radius for a magnification of x2000. This result gave some further support for the choice of size of filter for the main analysis (see also Section 3.10.6 below).

Consistency ratio mapping was implemented on the Meiko by rewriting the relevant parts of the kernel of the topcontouring code. The memory requirement is 4 MB per transputer (see the method of calculation given by Smart and Leng,

1990a). The Semper version is a direct development of the top-contouring
program.

Although consistency ratio mapping is slower than top-contouring, it is
theoretically preferable and easier to set up, since less parameters have to
be chosen. The main analyses reported below used consistency ratio mapping
with a radius of 10 pixels. The results presented below are for domains mapped
into 4, 8 or 12 directions; there is also a random class. Although some points
in the preceding intensity gradient analysis must be labelled undecided, the
number of pixels which remained undecided after either top-contouring or con-
sistency ratio mapping was either zero or negligible. Mapping into four direc-
tions allows the original images to be colored: e.g.:

horizontal domains	green
down-left domains	blue
vertical domains	red
down-right domains	yellow
random clusters	purple or white

In UEA, the consistency ratio maps are compressed by chord length coding and
stored; the practice in Glasgow is to re-calculate if necessary.

3.7.2   Post-processing

After the electron micrographs had been mapped, the mapped features were
measured using the standard routines provided by the Semper image analysis
package. To assess the capability of this package, and to compare alterna-
tives, 25 separate measurements were made on each domain of each image for
both drained series (see Appendix 3.2). Many of these measurements were effec-
tively alternatives: for example, Feret diameters, equivalent circular
diameter, and mean square root of the principal second moments, all measure
domain size. It was then possible to select from the alternatives those
measurements which were most useful; and this experience was used to reduce
the number of measurements made for the undrained series.

Fig. 3.10 compares the Index of Anisotropy calculated from intensity gradient
analysis with the average number of domains in each image obtained by con-
sistency ratio mapping using eight directions for the normally-consolidated
series of tests. The good agreement gave some confidence in these new methods
of image analysis.

3.7.3   Chord size analysis

The standard methods which are used in image analysis to measure features
assume that all the features are comparable in size and that most of them lie
wholly within the field of view. The maps produced here were more complicated.
In some cases, they did conform to these assumptions; in other cases, there
were very large domains which overlapped one or more edges of the micrograph.
To obtain an alternative estimate of the sizes of the mapped features, the
average chord size was calculated. The images are scanned from left to right.
For each line, the average chord length was first obtained as usual discarding
the incomplete chords at each end. Then, if these incomplete chords were

larger than the average, they were brought back into the calculation. Thus, a
global average for left-to-right scanning was obtained. The calculation was
then repeated for top-to-bottom scanning. The values used below are the
averages of the two results.

3.8 BLACK-AND-WHITE IMAGES

As an alternative to intensity gradient analysis and the mappings based on it,
black-and-white images were obtained by thresholding the gray levels after
Wiener filtering. The threshold was chosen automatically by comparing each
pair of adjacent pixels whilst scanning the image from top to bottom and thus
generating a relative contrast histogram $C(t)$. During the scan, each pair of
adjacent pixels was considered. Let I_a and I_b be the gray levels of such a
pair of pixels, and let $I_b > I_a$. Then, for every gray level T between I_a and
I_b, a contribution given by:

$$dC(T) \quad = \quad \min \ (T-I_a, \ I_b-T) \qquad\qquad (3.15).$$

was added to the relative contrast histogram. The peak of the relative con-
trast histogram based on all adjacent pairs in the whole image was accepted as
the threshold: pixels brighter than the threshold were mapped as particles;
other pixels were mapped as voids.

Before adopting this method, several others were tried. For simple images, the
histogram of gray levels has two well-defined peaks, one each for particles
and voids, and a well-defined and broad trough between; for these images, it
is easy to select a satisfactory threshold near the middle of the trough. In
our case, the blurring caused by the size of the point spread function caused
the two peaks to overlap and suppress the trough; so this method was
inapplicable. Since the intensity gradient is expected to be a maximum at an
edge, it was expected that the gray level corresponding to the greatest
intensity gradient would be acceptable as the threshold; Kohler (1981) reviews
methods based on this concept. This concept was tested using both 3x3 and 5x5
filters to calculate mod grad I; then, for each gray level, mod grad I was
summed and divided by the number of pixels which had that gray level to give
an average contrast histogram; finally, the gray level at the peak of the
relative contrast histogram was tested as a threshold. This method proved to
be unsatisfactory, and, as noted by Kohler (1981), the result is dependent
upon the actual formula used for mod grad I. The idea of considering only
adjacent pixels was introduced by Kohler (1981); but he normalized the con-
tributions to the relative contrast histogram by dividing each contribution
from each pair of pixels by the total number of contributions from that pair
of pixels:

$$dC_K(T) \quad = \quad \min \ (T-I_a, \ I_b-T) \ / \ (I_b \ - \ I_a) \qquad (3.16).$$

Kohler's version was found to place too much weight on the contributions from
the brighter particles and was unsatisfactory here. Our decision to scan
vertically rather than horizontally was taken after trying both alternatives:
there was little difference between them, and vertical scans were chosen
because more particles were horizontal than vertical.

Fig. 3.7 shows an image thresholded by this method. Note the sharpening of the image obtained by Wiener filtering and the better representation of the size and shape of the voids given by thresholding after filtering.

3.9 POROSITY ANALYSIS

3.9.1 Introduction

Two methods were developed to measure the local porosity based respectively on the original gray images and on those produced by Wiener thresholding.

3.9.2 Gray level method

By analogy with X-ray micro-analysis, the porosity, p, of an individual pixel is given approximately by:

$$p = (I_s - I)/(I_s - I_v) \qquad (3.17).$$

where I_s and I_v are the gray levels corresponding to pure solids and pure voids respectively. This method was developed for use in images in which the finest voids are smaller than the pixels with a view to measuring the porosity of each class of domain. The results quoted by Smart and Leng (1990a) for a mapped image were obtained in this way. If necessary, a gamma correction should be performed before making this analysis.

For the undrained samples, smoothed porosity, p, was plotted as a function of smoothed orientation, T, calculated using Eqn.3.13, e.g. Fig.3.8.d. As a general rule, porosity was lowest areas aligned in the direction of preferred orientation. The smoothed porosity was also used for density field mapping, see below.

3.9.3 Black-and-white method

After Wiener filtering and thresholding, an estimate of the porosity was calculated from the black-and-white images by counting the numbers of pixels which had been labelled as particle and void respectively. Fig. 3.11 compares the porosity found by image analysis with the moisture content found gravimetrically; although not perfect, the agreement between the two methods gives some confidence in the accuracy of the method used to threshold the images.

3.10 SUBSIDIARY ANALYSES

3.10.1 Introduction

In addition to the main set of algorithms developed in this study, several others were developed, assessed, or suggested; and these additional approaches are summarized below.

3.10.2   Enhanced orientation analysis

Intensity gradient analysis had originally been developed in soil micro-
structural analysis to measure the anisotropy of samples as seen in scanning
electron microscopes by obtaining the polar histogram of A. These were often
almost elliptical, whereas Proctor (1975), whilst working for one of us, had
shown that some at least of the hand mapping data followed semi-circular
normal distributions. The consistency ratio mapping program was therefore
modified to give an enhanced orientation analysis by providing histograms
instead of maps (Leng and Smart, 1991). The polar histograms of the smoothed
angle, T, give a stronger and clearer indication of preferred particle
orientation than do those of A, Fig.3.8.c. These histograms sometimes show a
few strong peaks, suggesting a multi-modal semi-circular normal distribution;
these peaks seem to be in agreement with subjective examination of the images.
It is thought that the polar histogram of A is elliptical, because noise from
the ends of the linear features and from other sources has degraded the 'true'
distribution. It is also possible to plot the strength of orientation,
measured for example by C or by the mean value of R, against the direction of
orientation, T, Fig.3.8.b.

3.10.3   Hough transforms

The concept of multi-modal semi-circular normal distributions was given some
support by an alternative analysis using Hough transforms which was made for
us by Luciano da Costa and Mark B.Sandler at King's College, London (Costa et
al, 1991a, 1991b).

3.10.4   Method of veins and convex hull

Some further support for the concept of multi-modal semi-circular normal dis-
tributions was given by a novel method of analysis, called the method of
veins, which was invented by Daisheng Luo (Electrical Engineering Department,
Glasgow University). In this method, the edges of the particles are followed
and recorded as chain code (Joyce Loebl, 1985); then, for each particle in
turn, the chain code is reduced to provide a measure of the orientation of
that particle (Lou et al., 1992). Mr. Lou went on to analyses the particles by
superimposing the convex hull, i.e. the figure formed by the enveloping
tangents, from which he took the longest diameter as an indicator of orienta-
tion. These two methods were developed whilst the top-contouring method was
first being implemented as an insurance against its failure, and we also con-
sidered finding the principal axes of each and every particle; but all these
methods would now seem to duplicate other findings and have not been used in
the main analysis.

3.10.5   Enhanced orientation mapping

Rather than mapping the domains into predetermined directions, it would be
preferable to map them into the directions indicated by the enhanced orienta-
tion analysis. At the time of writing, this is yet to be implemented; no dif-
ficulty is foreseen in choosing the directions interactively from the
histogram of T, but more experience seems desirable before attempting to have

the directions chosen automatically. It is thought that this method of
enhanced orientation mapping may produce an extra class of area in which small
packets of sub-parallel particles are mixed together randomly.

3.10.6   Semi-variogram

Complete semi-variograms for all lags up to one-quarter image size were calcu-
lated experimentally for a few micrographs following Webster and Oliver
(1990). Cross-sections of one of these is shown in Fig. 3.9.c. As a first
approximation, the circular model semi-variogram (Webster and Oliver, 1990,
p.229) was fitted to these results, giving a range of 18 pixels. A least
squares fit was used, so this fit was objective not subjective. Some interest-
ing observations follow.

1. The range of the semi-variogram, which represents the average distance
between two pixels which are quite un-related to each other, was comparable to
the size of the filter which had been selected for top-contouring and con-
sistency ratio mapping. This observation increased our confidence in our
choice of size of radius for these algorithms.

2. The range of the semi-variogram varied in direction, thus giving for the
first time, a definite indication of the ratio of the axes which should be
used if the circular filter were to be replaced by an elliptical one.

3. Some long range order was apparent. This observation led to the develop-
ment of the analysis described below under Density Field Mapping.

4. The nugget variance, i.e. the extrapolated variance at zero lag, was zero,
suggesting that the magnification could have been lowered without serious loss
of fine detail and with a gain in the size of the area examined.

These observations, which were made recently by Dr.Leng, require further
development and are the subject of a research application by her.

3.10.7   Density field mappingg

After discovering long range order in the semi-variograms, the variability of
the density field of the undrained samples was analyzed. Instead of density
itself, the local porosity was calculated by the gray level method within the
same large uniform filter as was used for consistency ratio mapping. An
intensity gradient analysis was made of the porosity field and compared with
the results from the original intensity gradient method and from enhanced
orientation analysis. To obtain the scale of the variation of porosity, the
porosity field was segmented at the mean value for the sample, and a chord
size analysis made.

3.10.8   Further porosity analysis

After images have been Wiener filtered and thresholded, the voids are clearly
distinguished from the particles. Two methods have been considered to extract
further information about the voids. In one method, the voids, which are long

and tortuous, could be sub-divided at their 'necks' and the pieces analyzed
individually. Alternatively, the particles could be dilated repeatedly by
increasing amounts, thus giving a pore size distribution.

-----ooooooOooooo-----

Appendix 3.1 LARGE UNIFORM FILTERS

The filters used here are necessarily large, typically 20 pixels radius, containing about 1300 pixels. However, the algorithms used are additive. Therefore, uniform filters were specified to limit the work required as the filter traverses the image. At each pixel in a line, the trailing edge of the filter is dropped and a new leading edge is added. Thus, for example, only 82 pixels around the perimeter are involved, a reduction of more than 90 %. The shape of the filter is defined by the half chord lengths, e.g RHS(P), where P is the distance of the chord from the center of the filter. Circular filters are used to minimize spurious orientation effects. The filter radius is specified in pixels, but 0.4 is added because this was found to improve the circularity of circles up to 7 pixels radius. For a nominal radius of 1, the eight nearest neighbors are used; and for a nominal radius of 0, the four nearest neighbors are used. In the Fortran versions, the two sides of the filter are defined separately:

$$LHS(-P) = RHS(P) \qquad\qquad (3.18).$$

so that shapes such as inclined ellipses could be used if necessary. Square, rectangular, and straight-line filters are also possible.

For moving from line to line, the top edge is dropped and a new bottom edge is added. The top and bottom of the filter are defined by TOP(U) and BOT(U), respectively, where U is the distance of the chord from the center. A separate set of registers is maintained for the first pixel in each line, and it is these which are updated; then their contents are copied to the registers for the filter which traverses the line.

Three schemes were considered to avoid unnecessary tests within the double loop needed to process the whole image.

a. In the first version of the code: the image array exactly equalled its nominal size; and the first filter on each line was set up without its leading edge. Then the operations within the loop were: add leading edge; calculate; drop trailing edge. A similar procedure was used for the 'leading column' filter.
b. In the present code: the image array is extended by one line and by one column; (the extra pixels are set to zero for definiteness); and the first filter on each line is set up naturally. Then the operations within the loop are: calculate; drop trailing edge; add leading edge. At the last pixel in each line, adding the leading edge is unnecessary; but it takes less time than would repeated testing to see whether the end had been reached, and it is the simplest method to code.
c. If the image array cannot be extended, then the loop could be shortened by one pixel, and the calculations for the last pixel could be made outside the loop. This seems to demand the use of INCLUDE statements for the repeated portions of code but would perhaps make the development of new algorithms easier.

When using large filters, it is important to avoid leaving large unprocessed borders. Smart and Leng (1990a) showed how to do this by reflection; and Smart et al. (1991) have a more general discussion.

-----ooooo0ooooo-----

Appendix 3.2   MEASUREMENTS FROM DOMAIN MAPS

The following quantities were measured for all the domains and random clusters which had been mapped:

1	XREF)	Domain reference point. bottom right-most pixel
2	YREF)	
3	ID	Identification number
4	PARENT	Identification number of parent region surrounding domain
5	HOLES	Number of holes in domain
6	BACKGROUND	Flag indicating domain is a hole inside another domain
7	CONTACT	Flag indicating domain touches (overlaps) edge of image
8	XMIN)	Limits of domain in image coordinates
9	XMAX)	
10	YMIN)	
11	YMAX)	
12	HFERET	Feret diameter. horizontal
13	VFERET	vertical
14	AFERET	at 45 degrees
15	BFERET	at 135 degrees
16	HPROJ	Total projected edge length. horizontal
17	VPROJ	vertical
18	PERIMETER	Perimeter
19	AREA	Area
20	XCEN)	Centroid
21	YCEN)	
22	MMIN)	Principal second moments of area
23	MMAX)	
24	ANGLE	Orientation of principal axis of domain
25	CIRCULARITY	4*PI*AREA/PERIMETER**2

The following quantities were calculated subsequently:

1   Mean Feret diameter. estimates domain size
2   Equivalent circular radius. estimates domain size
3   SQRT(MMIN*MMAX), estimates domain size
4   Minimum Feret diameter/Maximum Feret diameter, estimates domain shape
5   MMIN/MMAX. estimates domain shape
6   (HPROJ+VPROJ)/(2*mean Feret diameter), estimates indentation
7   (HPROJ+VPROJ)/(MMIN+MMAX), estimates indentation

-----ooooooOooooo-----
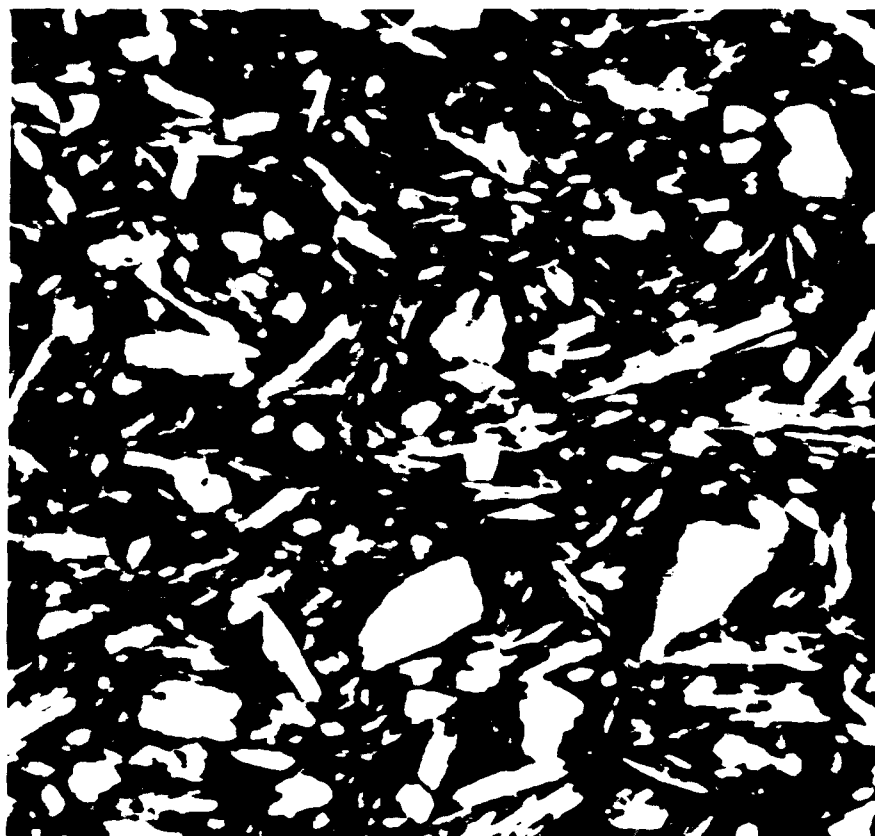
Fig. 3.1   Typical scanning electron micrograph.
Fig. 3.1.a   Original image.
56 µm square. Natural orientation: up-down = vertical:
across = horizontal.
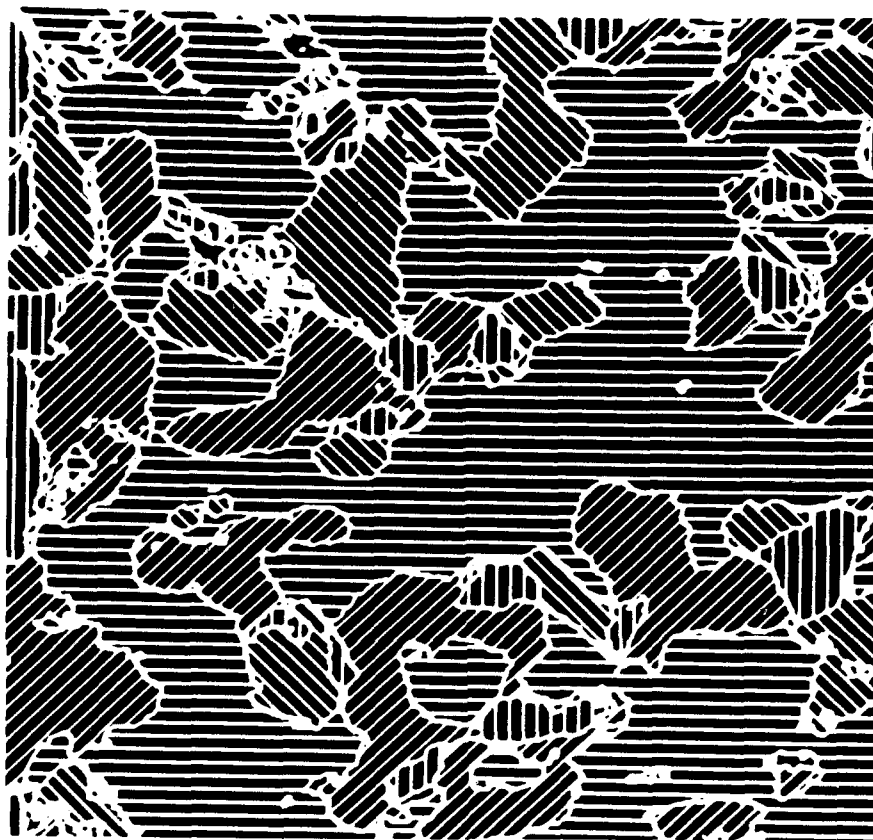(Fig. 3.1.b follows on the next page.)

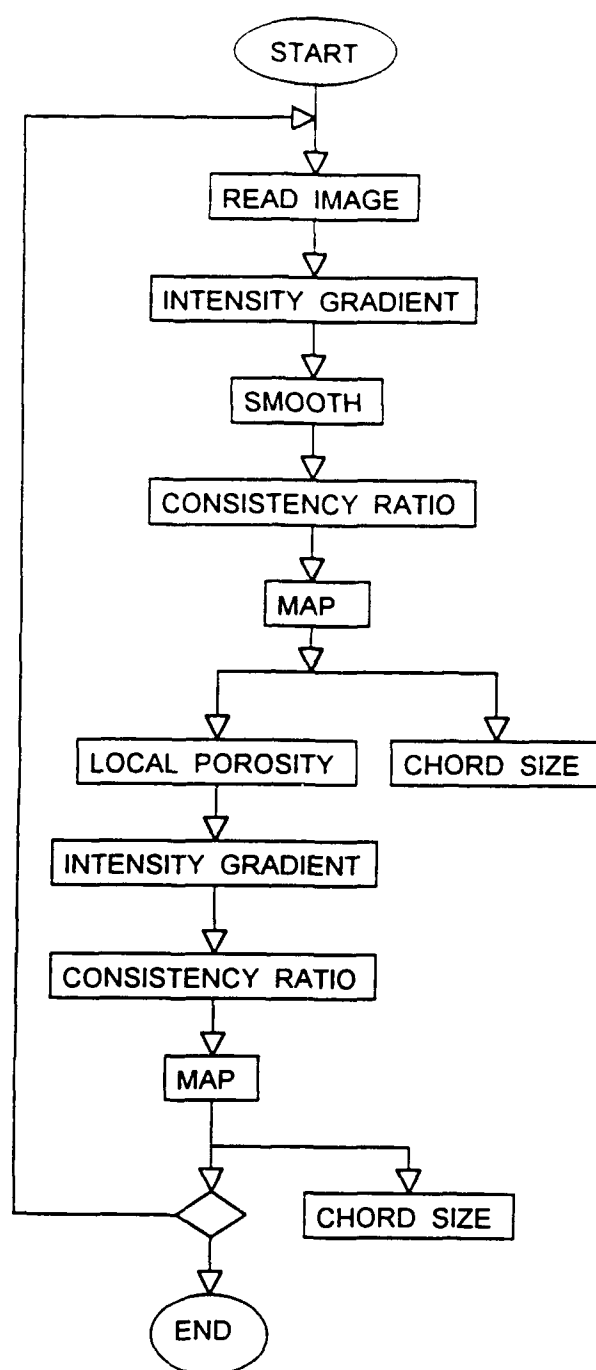Fig. 3.1.b   Consistency ratio map of Fig. 3.1.a.

Fig. 3.2 Simplified flow chart, Glasgow.

1)	Image Acquisition
2)	Compute Fourier Transform
3)	Search for Interference Peaks and Mask
4)	Determine Signal to Noise
5)	Image Reconstruction Wiener filtering
6)	Compute relative contrast histogram
7)	Threshold image
8)	Porosity Computations
9)	Domain Segmentation
10)	Porosity Computation for each domain class

Fig. 3.3 Simplified flow chart, UEA.
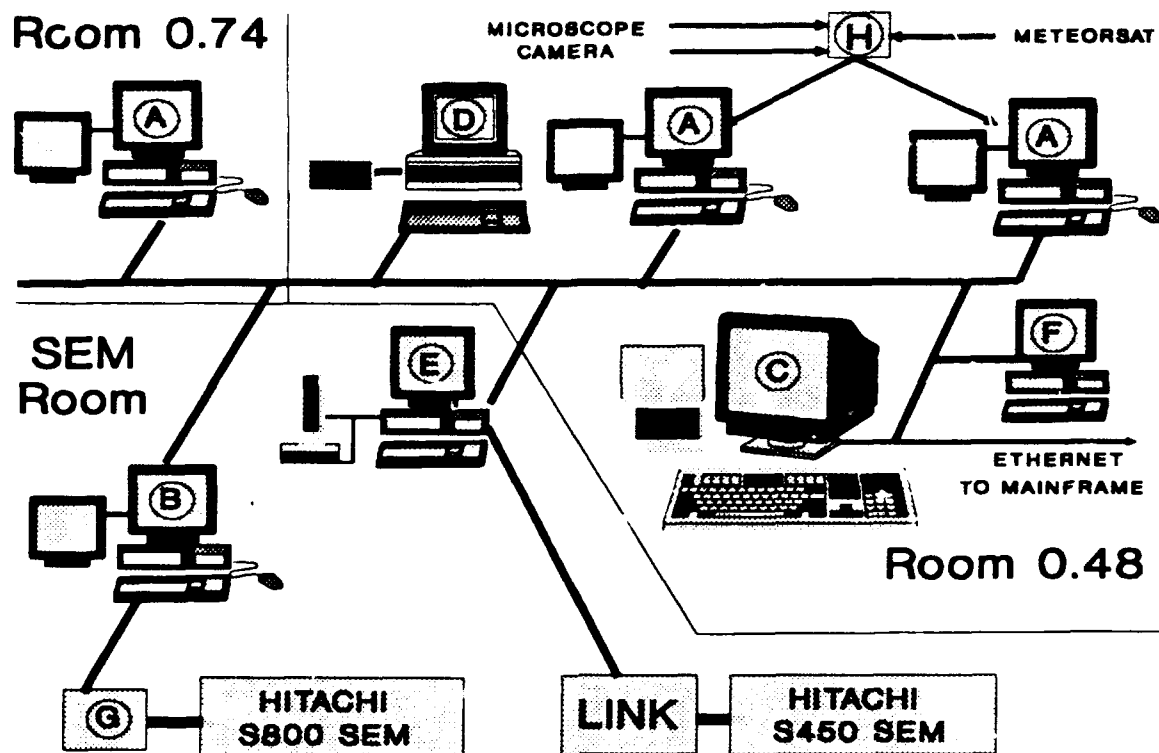
Fig. 3.4 Image analysis facility in UEA.

A. PCs with Synapse-Sprynt Frame Grabber and Semper.
B. PC with Synergy Slow Scan Frame Grabber and Semper.
C. Sun Workstation with additional hard disk.
   Exobyte tape streamer and Semper.
D. PC serving laser printer also connecting Sun to network.
E. PC with optical disk archive and tape streamer.
F. PC holding master programs and connecting Sun to network.
G. Interface between S800 SEM and Synergy Frame Grabber
H. Control switch to select various other image types.
LINK. Link Analytical digitiser for S450 SEM.

w. Windows in Sun Workstation
MO Master transputer
W. Worker transputers
GO Graphics transputer
S   Image screen
D   Disk store
T8 Independent transputer
Links are two-way, except to S
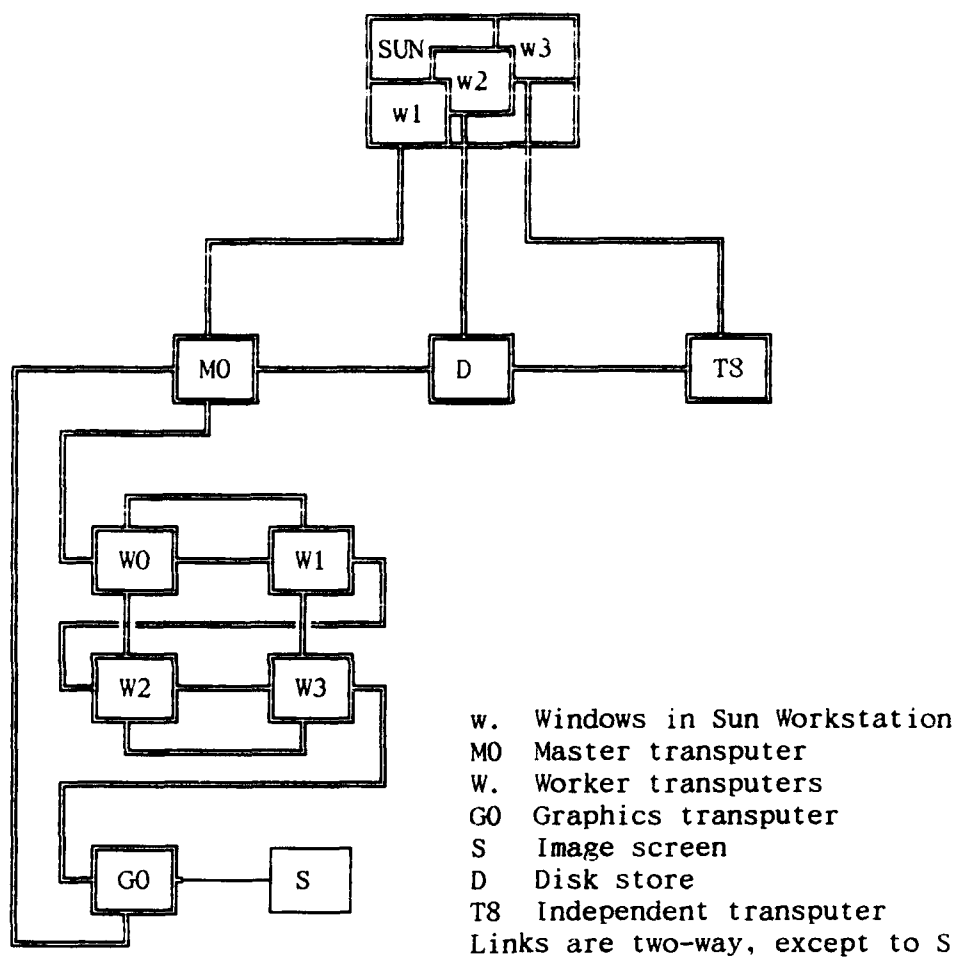
Fig. 3.5 Meiko multi-processor system at Glasgow.
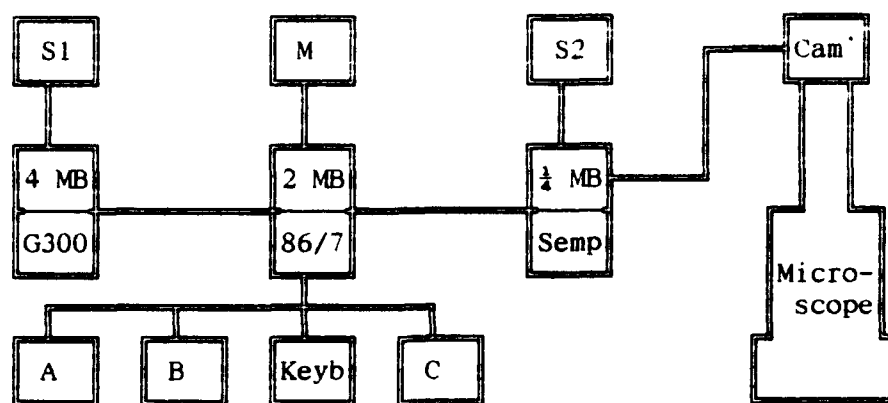
S1.S2 Image screens; M PC monitor; Cam' Camera:
G300   Transputer. graphics chip, 2 MB work'g, 2 MB video;
86/7   CPU, 2 MB = work'g, system, cache, d: ram disk. etc.;
Semp   Semper. framestore;
A.B   Floppy drives; Keyb Keyboard; C hard disk.

Fig. 3.6 Hybrid dual-processor system at Glasgow. Nimbus.
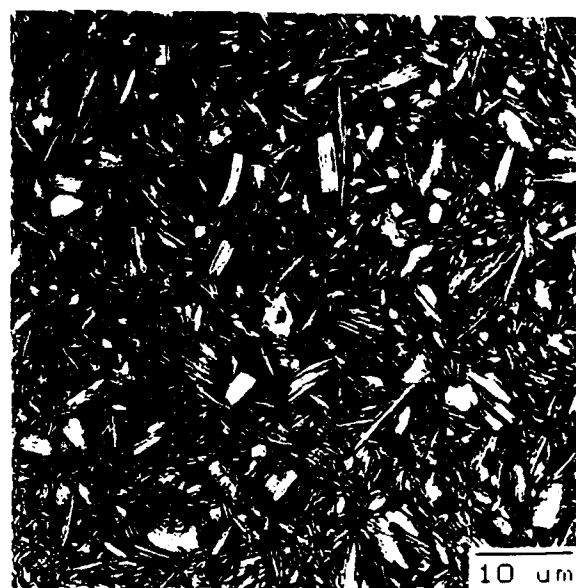
Fig. 3.7   Example of Wiener filtering.
Fig. 3.7.a   Original image.
Fig. 3.7.b   Thresholded after Wiener filtering.
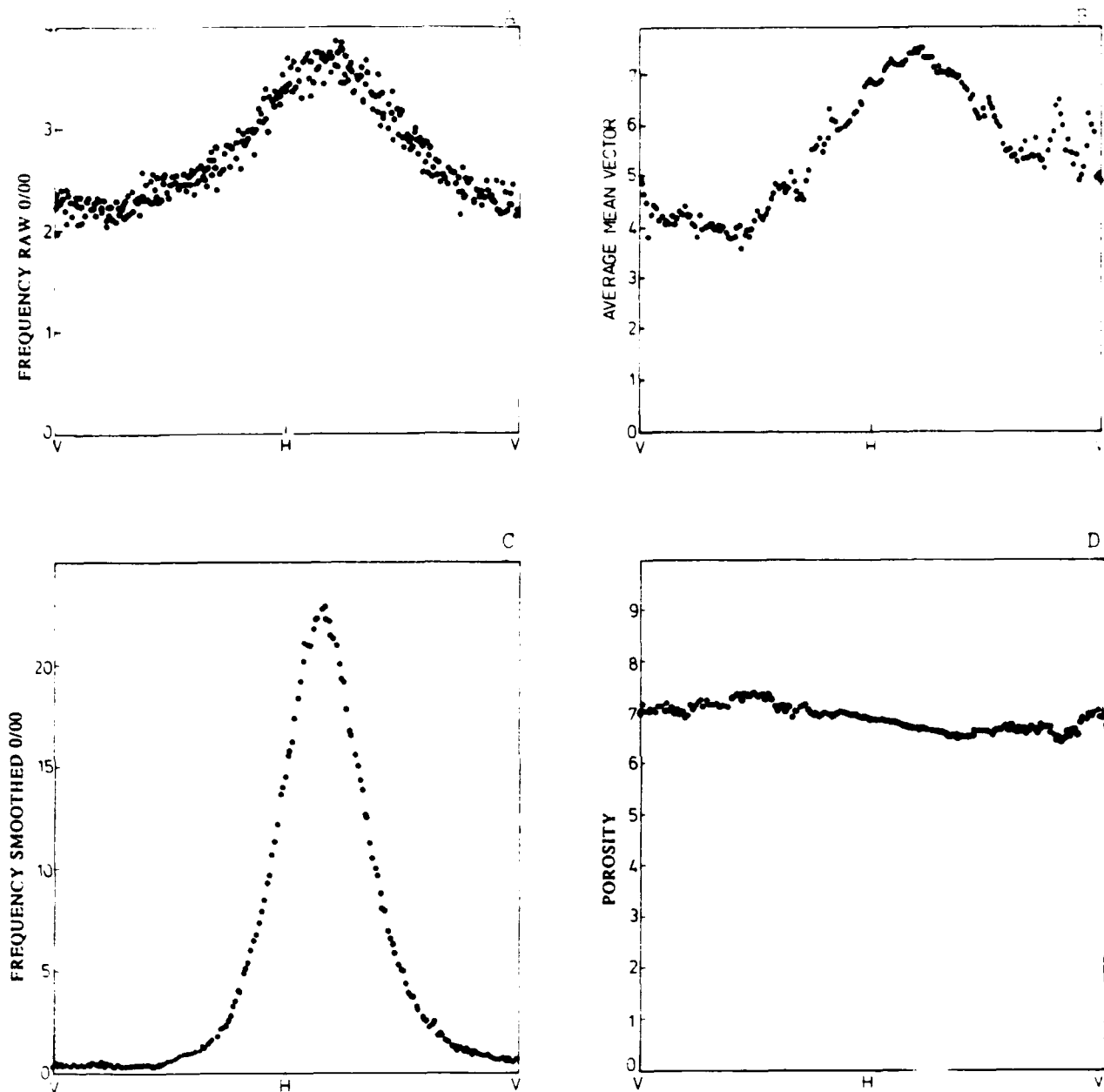
Fig. 3.8 Histograms (graphs) vs. Orientation.
Fig. 3.8.a Amount of orientation, *A*, intensity gradient analysis.
Fig. 3.8.b Strength of orientation, average mean vector.
Fig. 3.8.c Amount of orientation, *T*, consistency ratio mapping.
Fig. 3.8.d Average porosity.
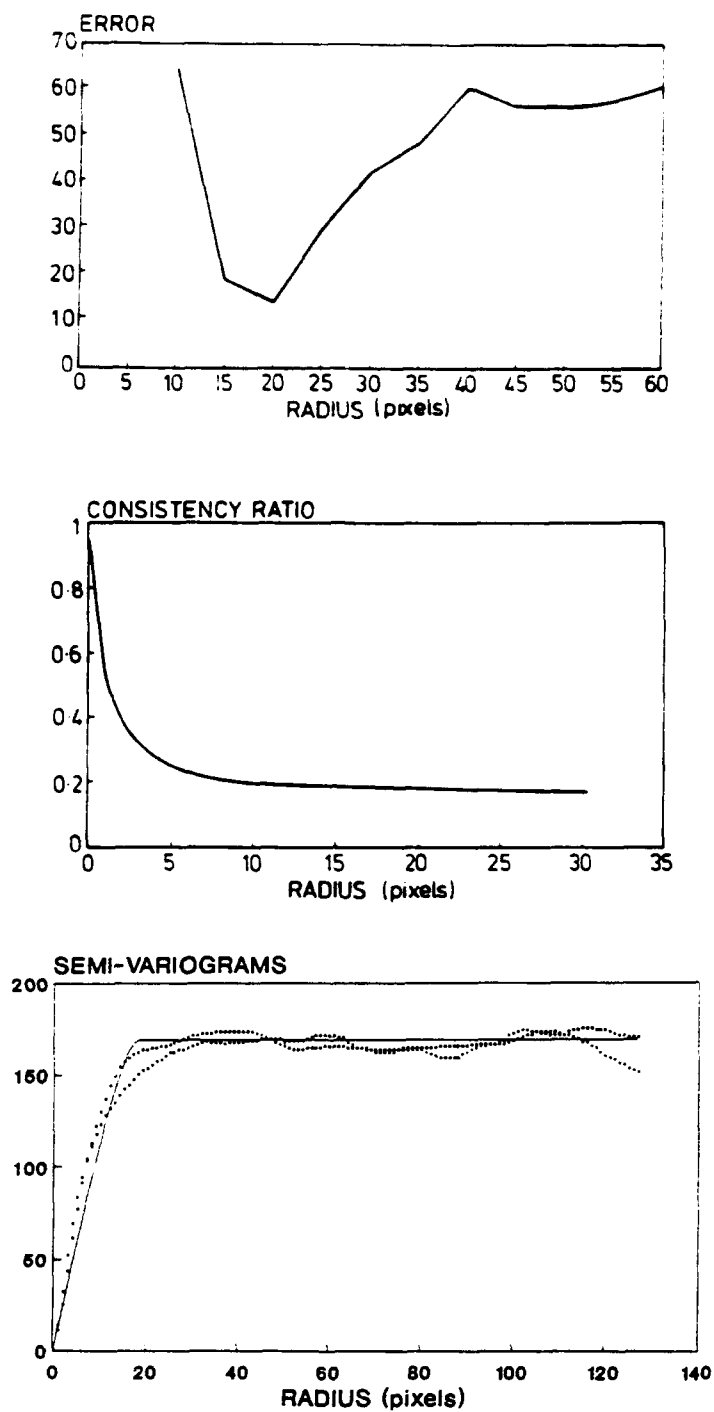
Fig. 3.9 Choice of radius of filter.
Fig. 3.9.a Modified chi-square. for Fig.1.
Fig. 3.9.b Consistency ratio. for a low magnification image.
Fig. 3.9.c Semi-variogram. circular model fitted, for Fig. 1.
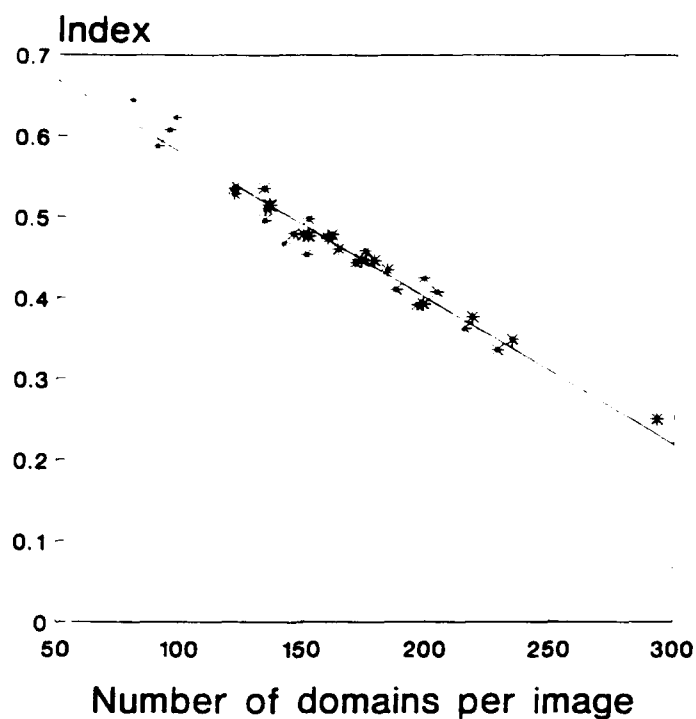
Fig. 3.10 Index of Anisotropy vs. Number of domains (SEM nc).
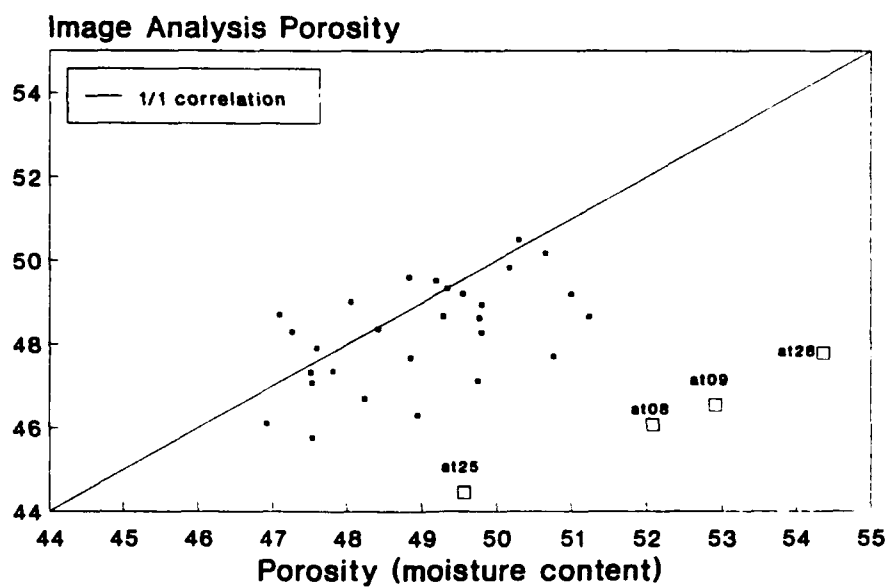
Fig. 3.11 Image analysis porosity vs. Moisture content (SEM nc).
The gravimetric moisture content is thought to be wrong for 4 samples.

OPTICAL MICROSCOPY

4.1 INTRODUCTION

Mitchell was the first to apply the technique of optical microscopy to the investigation of soil structure in geotechnical engineering in 1956 (Mitchell, 1956). Much use has been made of optical microscopy since then (e.g. Wu, 1958, Smart, 1966a; Tchalenko, 1967). The usual technique and the one which was used here employs thin sections. These were prepared conventionally from impregnated 'half-samples' similar to those used for scanning electron microscopy (see previous Chapter).

The technique for observation of micro-structural features in thin sections of clay is based on the optical properties of clay particles. A platy kaolinite particle is optically anisotropic and possesses three approximately mutually perpendicular optical axes: two almost in the plane of the particle, which are called section axes here, and one almost at right angles to this plane. The refractive indices in the directions of the section axes are approximately equal and significantly different from that in the third axial direction. When a single particle is viewed between crossed polars, it may or may not exhibit extinction and illumination; but when a thin section is examined, it transmits a variable intensity of light depending on: the orientation of the optical axes of the particles in the thin section, the refractive indices of the mineral, the thickness of the thin section, the wave length and the intensity of the light. This transmitted intensity varies as the thin section is rotated with respect to the direction of polarization. For a certain thin section, assuming that its thickness is uniform, under a certain light, the intensity of light transmitted through the thin section depends only on the orientation of the optical axes of the particles in the thin section and the related positions of the optical axes of the particles and of the direction of the light. Thus, if kaolinite particles are arranged in a random style within a sample, a thin section in any direction through the sample does not exhibit extinction or illumination, since the optical axes of the particles are also distributed randomly. When such a thin section is rotated between crossed polars, the intensity of transmitted light remains constant throughout the 360°. If the particles are oriented with their planar surfaces parallel, extinction and illumination will occur in thin sections cut from the sample in particular directions. When a thin section is cut parallel to the orientation planes and viewed between crossed polars, no change shows in illumination with rotation, since the refractive indices in the directions of the section axes of the particles are approximately equal; but, when a thin section is cut normally to the plane of preferred orientation, four stages of extinction and illumination occur between crossed polars, since the optical axes of the particles lie in preferred directions. Hence, measurement of the transmitted light intensities may be used as an indirect measurement of the particle orientation. This Chapter gives a review of a previous method and introduces three new and improved methods.

4.2 POLARIZING MICRO-PHOTOMETRIC ANALYSIS. PMPA

Previous work has used Polarizing Micro-Photometric Analysis. PMPA. for a
microscope with crossed polars and a thin section between them. for the
intensity of light. the transfer function is (e.g. Smart. 1966a):

$$I = 0.5 \sin^2 2\emptyset \sin^2 \delta/2 \qquad (4.1).$$

where $\emptyset$ is the angle between the section axes and the axes of the polars: δ is
the phase difference after the light has passed through a thin section. which
is a function of the thickness of the thin section. d. and the wave length of
the light. l. Therefore. for areas not dark in ordinary light. the diagnosis
is:

```
┌ dark for all Ø:
│
│        ┌ for all wavelengths:
│        │
│        │        ┌ when section tilted:              Isotropic.
│        │        │
│        │        └ otherwise:                        Optic axis ⊥ section.
│        │
│        └ only for wavelength = l:       d = kl/δn. k = 1.2.......
│
└ 4 extinction positions:   Extinction directions ⊥ section axes.
     (per revolution)
```

As mentioned above. it may be found that the greater the difference between
illumination and extinction, the greater the degree of the orientation of par-
ticles. So with a microphotometer, quantitative results are obtained by
measuring the intensities of the polarized light transmitted through a section
in the illumination and extinction positions. The ratio of the two measure-
ments. or some other combination of factors dependent on them. is an indica-
tion of the degree of preferred orientation.

Smart (1966a) defined an Anisotropy Index. A_1. as:

$$A_1 = \frac{I_{max} - I_{min}}{I_{max} + I_{min}} \qquad (4.2).$$

where I is the intensity of the light transmitted. In theory. the value of the
anisotropy index A_1 ranges from 0. which indicates a random arrangement of
particles. to 1, which indicates an ideal orientation arrangement of parti-
cles. In practice, because of slight asymmetry of the measurements. an average
of four maxima and an average of four minima are used. The difference between
the formula for Anisotropy Index, A_1, here and Index of Anisotropy, I_A, used
for scanning electron microscopy was deliberate. as it was thought that the
physical conditions of measurement were different.

By means of the microphotometer, the average orientation direction of the par-
ticles can be determined too. A full-wave compensator could be used to locate
the direction of preferred orientation by comparing the colors seen with the

_olors of failure planes. However, there is a small risk of an error of 90° in
any single observation.

In the observations described here, the objective was x10 and the field of
view was 1.5 mm diameter. In general, five fields of view were observed from
one thin section from each triaxial test sample.

4.3 POLARIZING MICRO-PHOTOMETRIC MAPPING I, POLMAP

When viewed between crossed polars, the matrix of clay soil often shows dif-
fuse light and dark patches which represent information which has been diffi-
cult to extract by conventional microscopy. By using a special type of optical
microscopy and computer analysis system, the following new method has been
developed.

It is known that extinction occurs only when the section axes are parallel to
or perpendicular to the axes of polars when a thin section is viewed between a
crossed polars; and, when a quarter-wave plate is used in such a position that
the angle between the axes of the quarter-wave plate and the axis of the
polarizer is 45°, the transfer function becomes:

$$I \quad = \quad 0.5 \ (1 - \sin 2\emptyset \sin \delta) \qquad\qquad (4.3).$$

In this case, full extinction occurs when the angle between the section axes
and the axis of the polarizer becomes 45° and δ is $\sin^{-1}+1$ or this angle is
135° and δ is $\sin^{-1}-1$.

Most of the measurements discussed here were made using a Leitz Dialux-pol
microscope in which the polarizer, the analyzer, and a slot for a compensator,
are all linked together by an arm and can be rotated synchronously (see Smart
and Tovey 1982 Fig.2.1). The Leitz microscope used here has another slot which
is fixed in the body of the microscope, and which must not be used here. Some
measurements were made using a Prior-Swift MPB124 Polar Microscope in which
similar synchronous rotation was achieved by internal gearing.

To explain the method, Fig.4.1 shows a failure plane running diagonally
through a field most of which is oriented up-and-down the page: the field of
view is 0.47 mm square.

In Fig.4.1.a, the polars were crossed 'on the square', the synchronizer angle
being 90°, so the failure plane is bright; and dark areas are areas in which
the clay particles are aligned either horizontally or vertically (with respect
to the field of view). This micrograph was digitized and denoted by x2. A cor-
responding micrograph, x1, was digitized with the polars crossed 'on the
diagonal', the synchronizer angle being 45°; in this micrograph the contrast
was reversed. In the first stage of analysis, these two microphotographs were
compared to distinguish between areas oriented 'on the square' and 'on the
diagonal'. Each pixel was coded as follows:

    1   if brighter in x1 than x2, on the square;
    2   if brighter in x2 than x1, on the diagonal;
    0   otherwise, i.e. undecided.

After this preliminary coding, four more digitized micrographs were used to
distinguish horizontal from vertical and down-left from down-right. All these
micrographs were taken with a quarter-wave plate inserted in the compensator
slot and rotating synchronously with the polars.

In the second stage of analysis, only pixels coded 2 were considered, and two
micrographs taken with the synchronizer set at 90° and 0° were used. These two
micrographs are denoted q2 and q4 and are shown in Figs.4.1.c and d, respec-
tively. In one of these micrographs, the brighter areas are down-left, and in
the other they are down-right: a pragmatic method of deciding which is which
is to experiment with failure planes in which the particle alignment may be
assumed safely. Thus, the pixels which had originally been coded 2 were
recoded as follows:

> 2 if brighter in q2 than q4, i.e. down-left;
> 4 if brighter in q4 than q2, i.e. down-right;
> 0 otherwise, i.e. undecided.

Similarly, using micrographs q1 and q3, with the synchronizer set at 135° and
45°, respectively, the mapping can be completed. The result is shown in
Fig.4.1.b, where the two diagonal classes have been ruled and the up and
across areas have been left blank.

During analysis, a convenient method of presenting the results is to color the
pixels as follows:

> 1 horizontal, red;
> 2 down-left,   yellow;
> 3 vertical,   green;
> 4 down-right, blue;
> 0 undecided,   black.

The colors were chosen because thin sections such as the one used here fre-
quently show yellow and blue for the pixels coded 2 and 4 respectively when
viewed in white light with the synchronizer set at 90° and using a full-wave
compensator. Under those conditions, the other areas tend to be pink, leading
to green vertical and red horizontal. In theory, for the analytical method
used here, monochromatic light with a wave-length matched to that of the
quarter wave plate should be used; but in practice, white light was found to
be more convenient and to give similar results.

The overall anisotropy of the field of view may be assessed by considering the
number of pixels mapped into each direction: undecided, horizontal, down-left,
vertical, down-right. Following the PMPA method above, an Anisotropy Index,
A_2, obtained by this method, polarizing micro-photometric mapping (PMPM), may
be defined as follows:

$$A_2 = \frac{|(H + V) - (L + R)|}{H + V + L + R} \qquad (4.4),$$

where H, V, L and R are respectively the number of pixels mapped into the
directions: horizontal, vertical, down-left and down-right. The Anisotropy
Index, A_2, obtained from POLMAP can be compared with that given by polarizing
micro-photometric analysis (PMPA), A_1. Usually, for the same area, A_1 was a

little lower than it. These two values of A are not strictly comparable, because the PMPA measurement has been taken over a wider field of view than the POLMAP measurement. Further, the directions used for POLMAP were chosen arbitrarily beforehand, whereas the directions used for PMPA were the actual observed directions of maximum and minimum preferred orientation.

The sizes of the patches mapped by POLMAP were measured using the chord size algorithm which was described in the previous chapter.

In general, four fields from one thin section were measured for each triaxial sample using POLMAP: all the measurements quoted below were made on fields 0.47 mm square.

Three versions of another new method are indicated below.

4.4 POLARIZING MICRO-PHOTOMETRIC MAPPING II

4.4.1   Introduction

After establishing the POLMAP algorithm, a set of algorithms which obtain the orientation of each pixel was developed. Of the versions described below, POLMAP3 is the most economical; but the digitized micrographs required for POLMAP4 had already been acquired, so this version was used for the main analysis.

4.4.2   Polmap4

When a parallel beam of monochromatic light passes through a polarizer, a thin section, a quarter-wave plate, and an analyzer which is crossed with the polarizer, as mentioned above, I, the transfer function of the intensity of the light is as follows:

$$I = 0.5 (1 - \sin 2\emptyset \sin \delta) \qquad (4.5),$$

where $\emptyset$ now refers to the inclination of one of the section axes of a pixel. Then, suppose that the synchronizer is set in turn at 0°, 45°, 90°, and 135°, then, the intensity of the light at each setting may be calculated from the following functions.

$$I_0 = 0.5 (1 - \sin 2\emptyset \sin \delta) \equiv q2 \qquad (4.6),$$

$$I_{45} = 0.5 (1 - \cos 2\emptyset \sin \delta) \equiv q3 \qquad (4.7),$$

$$I_{90} = 0.5 (1 + \sin 2\emptyset \sin \delta) \equiv q4 \qquad (4.8),$$

$$I_{135} = 0.5 (1 + \cos 2\emptyset \sin \delta) \equiv q1 \qquad (4.9),$$

where q1, q2, q3 and q4, denote the corresponding micrographs. Therefore:

$$\tan 2\emptyset = \frac{I_{90} - I_0}{I_{135} - I_{45}} \qquad (4.10),$$

$$\sin \delta = \ [\ (I_0 - I_0)^2 \ + \ \ldots \ - \ \ldots \ \ \ 4.11$$

Thus, the direction of preferred orientation at each pixel can be obtained. Except that $\emptyset$ was labelled undecided if the numerator and denominator of tan $2\emptyset$ were both small. This new method was called POLMAP4.

Fig.4.2 shows a polar histogram for one field of view obtained using this method.

For mapping, the degrees were divided into groups, which were horizontal $(0°-22.5°$ and $157.5°-180°)$, down-left $(22.5°-67.5°)$, vertical $(67.5°-112.5°)$, and down-right $(112.5°-157.5°)$. Comparison with POLMAP gave satisfactory results. If desired, the degrees could be divided into a larger number of groups, say 8 or 12, for a finer mapping.

Taking the assumed intensity at each pixel as a unit vector, the Consistency Ratio, C, was calculated from:

$$X = \Sigma \cos 2\emptyset \qquad (4.12).$$

$$Y = \Sigma \sin 2\emptyset \qquad (4.13).$$

$$R = \sqrt{(X^2 + Y^2)} \qquad (4.14).$$

$$C = R/S \qquad (4.15).$$

$$T = \tfrac{1}{2} \text{ atan } (Y/X) \qquad (4.16).$$

where S is the number of decided pixels. T was labelled undecided if X and Y were both small. The values of Consistency Ratio obtained were almost always higher than the corresponding values of Anisotropy Index.

For the normally-consolidated undrained series of triaxial tests, POLMAP4 was used in addition to POLMAP.

4.4.3 Polmap3

POLMAP3 comes from the same theory as POLMAP4 and produces the same results from only three micrographs. When the synchronizer is set in turn at $0°$, $120°$, $240°$, the intensities of the light through the thin section are determined by the following functions respectively:

$$I_0 = 0.5 \ (1 - \sin 2\emptyset \sin\delta) \qquad (4.17).$$

$$I_{120} = 0.25 \ (2 + (\sin 2\emptyset + \sqrt{3} \cos 2\emptyset) \sin\delta) \qquad (4.18).$$

$$I_{240} = 0.25 \ (2 + (\sin 2\emptyset - \sqrt{3} \cos 2\emptyset) \sin\delta) \qquad (4.19).$$

Therefore: $$\tan 2\emptyset = \frac{I_{120} + I_{240} - 2I_0}{\sqrt{3} \ (I_{120} - I_{240})} \qquad (4.20),$$

$$\sin \delta = 2/3 \ \sqrt{\{(I_{120} + I_{240} - 2I_0)^2 + 3 \ (I_{120} - I_{240})^2\}} \qquad (4.21).$$

Fig.4.2 also shows the polar histogram for the same field of view obtained using POLMAP3, which has very good agreement with the result from POLMAP4.

By the same method, the Consistency Ratio may also be calculated from POLMAP3.

POLMAP3 requires three micrographs, q_0, q_{120}, and q_{240} for the Prior-Swift MPB124 Polar Microscope. For the Leitz Microscope, three micrographs q_0, q_{120}, and q_{60}, may be used, because q_{240} is unavailable and $I_{60} = I_{240}$.

Although POLMAP3 requires fewer micrographs than either POLMAP or POLMAP4, the data required for POLMAP4 had already been measured for POLMAP. Thus, it was convenient and saved time to use POLMAP4 here.

4.4.4 Polmap6

Since $I_{60} = I_{240}$, etc., POLMAP3 generalizes readily to POLMAP6, which would have been more accurate. But POLMAP6 would have required six micrographs per field, so it was not implemented.

-----oooooOooooo-----
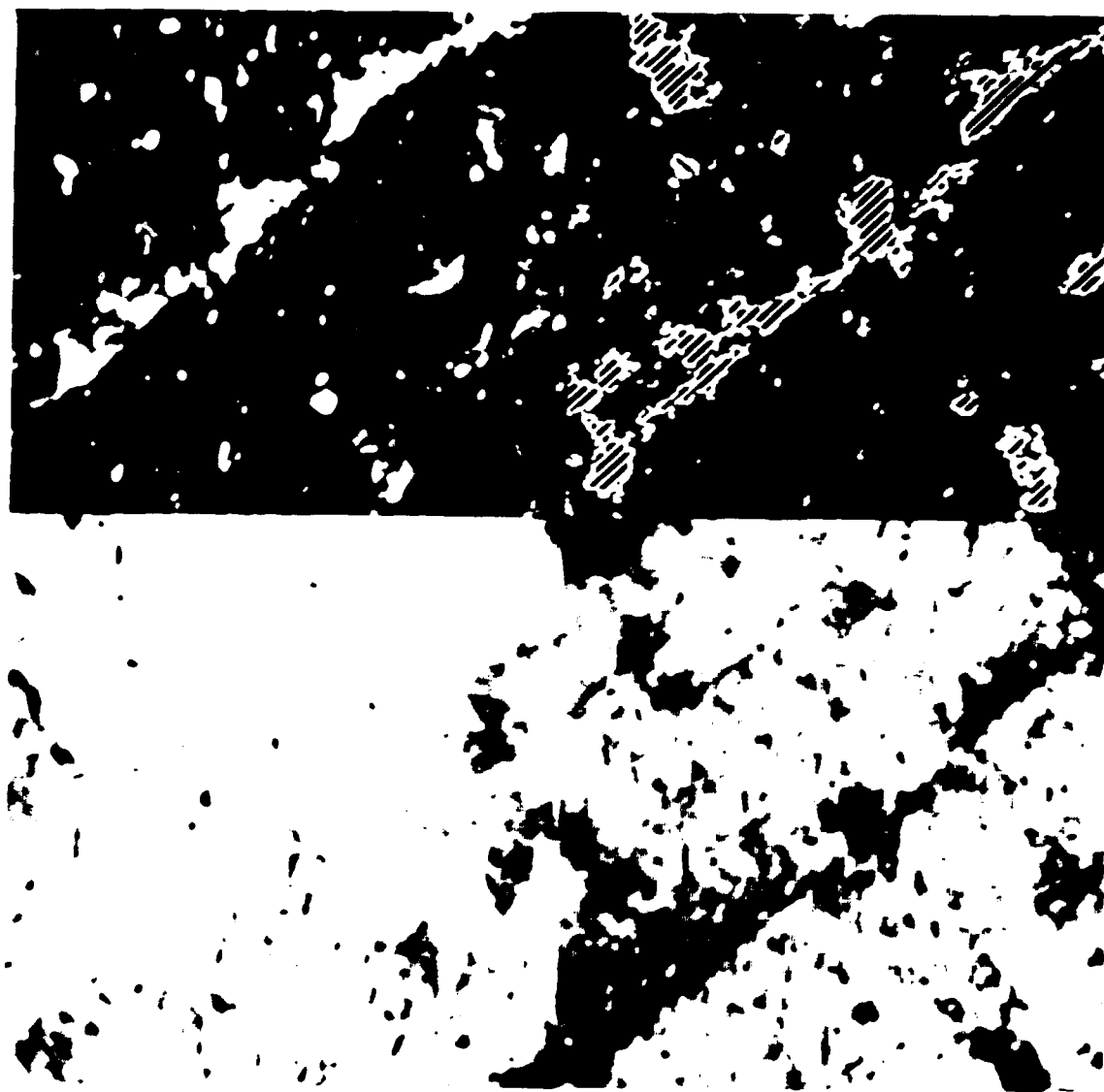
Fig. 4.1 Optical micrographs, failure plane, 0.4⁻ mm square.
Fig. 4.1.a Polars crossed on the square, x2.
Fig. 4.1.b Mapped using POLMAP, sloping directions ruled.
Fig. 4.1.c With quarter-wave plate, q2.
Fig. 4.1.d With quarter-wave plate, q4.
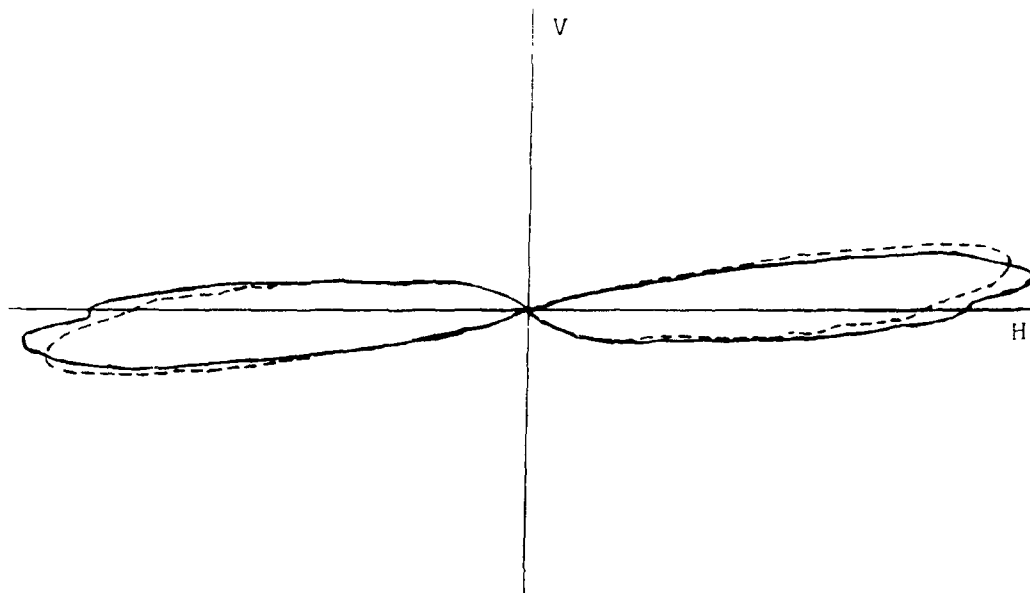
Fig. 4.2 Polar Histograms for one field 0.47 mm square.
Full line: from POLMAP4. Broken line: from POLMAP3. Oriented naturally: up-
down = vertical: across = horizontal.

NORMALLY-CONSOLIDATED DRAINED TESTS

5.1 INTRODUCTION

The new methods of micro-analysis were first applied to a series of 41 normally consolidated drained triaxial tests of Speswhite kaolin after preparation in the medium pressure filter presses. In brief: the slurry was mixed at 140 % moisture content, i.e. 303 % Liquidity Index; consolidated uniaxially to 700 kPa; consolidated triaxially to 700 kPa; strained at 5 % per day; impregnated with Araldite AY18; and prepared for microscopy.

5.2 STRESS-STRAIN BEHAVIOR

Fig. 5.1 illustrates the deviator stress vs. axial strain for typical samples from the normally consolidated undrained series, the results being much as expected. i.e. a steady rise of deviator stress to a peak value at say 16 % axial strain, at about which strain failure occurred, there being a small amount of variability from sample to sample. Fig. 5.2 shows the volumetric strain vs. axial strain for the whole normally consolidated series, each point being the end point of one test, except at the origin, where there were several control samples. As expected, the samples consolidated throughout the tests. The rate of consolidation was faster at first and then slowed considerably. there being a fairly strongly marked change of behavior at about 8 % axial strain. Also, somewhat unexpectedly perhaps, the points during the early stages of the tests were not far removed from the Ko-line, i.e. the lateral strain was almost negligible up to about 8 % axial strain (e.g. $\epsilon_l \approx -1.5$ % when $\epsilon_a = 8$ %, but $\epsilon_l \approx -7$ % when $\epsilon_a = 20$ %).

5.3 VISUAL EXAMINATION

When viewed between crossed polars with or without a full-wave plate, the kaolin often showed diffuse light and dark patches, although some fields were more uniform or had more obvious horizontal preferred orientation than others.

Visual examination of the scanning electron micrographs showed that the structure of the samples was composed mainly of diffuse domains, which tended to merge together. As indicated below, there were a few random clusters; but there were virtually no inter-domain voids in these samples. Thus, the hypothesis that shear deformation is accommodated by slip of domains into the inter-domain voids is irrelevant here; but there could still have been slip of the domains into the looser and presumably weaker random areas.

Failure planes, when they occurred, were slickensided as usual and cut through the previously-existing structure non-conformably; however, attention here is concentrated on the 'pre-peak' deformation.

The measurements discussed below were taken on fields as follows:

PMPA	1.5 mm diameter
POLMAP	0.47 mm square
SEM	0.025 mm square

5.4 PREFERRED ORIENTATION

Fig. 5.3 shows the preferred orientation vs. axial strain obtained from the polarizing micro-photometric analysis, PMPA. Here and in the graphs following, each point is the end point of one test. The results in this figure are the moduli of the algebraical average of the five values of orientation obtained from the five fields measured by this technique. and they are expressed as inclinations from the horizontal. Fig. 5.4 shows the corresponding values obtained from scanning electron microscopy using intensity gradient analysis. All the values in both graphs are low: i.e. the preferred orientation started close to the horizontal and remained close to the horizontal throughout. Thus, the hypothesis that the particles would gradually rotate into the direction of the failure plane is eliminated.

5.5 STRENGTH OF ANISOTROPY

Figs. 5.5, 5.6, and 5.7 show the strength of anisotropy vs. axial strain measured by PMPA, POLMAP, and SEM, respectively. Each point is the arithmetical average of Anisotropy Index for 5, 4, and 24 fields, respectively.

In all three graphs. the Anisotropy Index starts at a moderate value and ends at a moderate value. This is in accordance with the hypothesis that, during shear deformation, strongly anisotropic samples become less anisotropic and weakly anisotropic samples become more anisotropic; these samples appear to be on the borderline.

All three graphs appear to show a further effect. To illustrate this, quadratic regressions have been added to the first two figures. and linear regressions have been added to the early and late stages of the third figure. Although these regressions were not shown to be significant, presumably because these graphs show a larger scatter than had been anticipated from previous studies when the experiment was planned, all three graphs do seem to show a strengthening o. anisotropy during the early stages of the tests whilst the samples were consolidating with negligible lateral strain, and a weakening of anisotropy during the late stages of the tests whilst the lateral strain was increasing.

5.6 RANDOM CLUSTERS

In addition to mapping domains defined by strong internal preferred orientation of the clay plates. random clusters of clay plates were also mapped in the scanning electron micrographs. Fig. 5.8 shows the area of random clusters vs. axial strain. The total random area is fairly small. say 5 % in comparison with say 95 % domains. There might have been a trend concave upwards, which would agree with the concave downward trend for strength of anisotropy, but if so it is small.

5.7 SIZES OF FEATURES

Fig. 5.9 shows the average chord length of the areas mapped using POLMAP vs. axial strain, the trend apparently being concave upwards.

Fig. 5.10 illustrates the average size of the domains mapped in the scanning electron micrographs vs. axial strain. Trend lines are shown for horizontal, vertical, and two inclined groups of domains. The domains with horizontal preferred internal orientation were the largest: the vertical domains were the smallest; and the inclined domains were intermediate in size. Strain appears to have had negligible effect on the sizes of these domains; thus, both the hypothesis that the domains would increase in size and the hypothesis that the domains would break up and decrease in size with shear appear to be eliminated.

Fig. 5.11 shows the average size of the random clusters mapped in the scanning electron micrographs vs. axial strain. These are comparable in size to the vertical domains and seem to show a trend concave upwards.

5.8 POROSITY

Fig. 5.12 illustrates the porosity of the features mapped in the scanning electron micrographs vs. axial strain. The results here were obtained from the scanning electron micrographs after Wiener filtering and thresholding to obtain a binary 'solid-or-pore' image. The deviations from the trend lines were relatively small. Although the trend line for the total porosity obtained by gravimetric analysis was concave upwards, see the graph of volumetric strain above, the trend lines themselves were all straight. As expected, the average porosity of the random clusters was higher than that of the domains. Somewhat unexpectedly, the average porosity of the horizontal domains was higher than that of the vertical domains; as expected, the porosities of the inclined domains were intermediate between those of the horizontal and vertical domains. The fact that all the trend lines fall at the same rate suggests that the deformation of the samples is being accommodated within all parts of the structure at the same rate, i.e. that the micro-deformations are distributed uniformly throughout the samples.

5.9 SUMMARY

During the early stage of shear deformation, up to 8 % axial strain say: the lateral strain was almost negligible; the preferred orientation remained horizontal; the strength of anisotropy seemed to increase; the area of random clusters might have decreased; the sizes of the random clusters seemed to decrease; the sizes of the domains apparently remained constant; the sizes of the areas mapped by optical microscopy seemed to remain constant; and the porosity of all sectors of the structure decreased at the same rate. All this suggests uniaxial consolidation during the early stage of shear deformation, with the micro-deformations being distributed uniformly throughout all sectors of the samples.

During the late stage of shear deformation, from 8 % to 16 % axial strain say: the lateral strain increased; the preferred orientation remained horizontal.

at the strength of anisotropy seemed to decrease: the area of random clusters might have increased: the sizes of the random clusters seemed to increase: the sizes of the domains apparently remained constant. But the sizes of the areas mapped by optical microscopy seemed sometimes to increase: and the porosity of all sectors of the structure decreased at the same rate. This again suggests that the micro-deformations were distributed uniformly throughout all sectors of the samples. However, it seems that particles or domains are beginning to rotate away from the horizontal, but with equal quantities turning upwards and downwards: and that these rotations caused slight disruption to the structure. The optical microscopy suggests that there may perhaps have been a tendency to medium-scale organization, with domains in one part tending all to turn one way, and with domains in an adjacent part tending all to turn the other way.

In summary, therefore, the observations suggest that three different mechanisms were acting: one in the early stage of shear deformation as the samples bedded down: the other in the late stage of shear deformation as the samples began to be disrupted: and both these mechanisms were distinct from the formation of failure planes.

-----oooooOooooo-----

Fig. 5.1   Deviator stress vs. Axial strain (ncd).

Fig. 5.2   Volumetric strain vs. Axial strain (ncd).
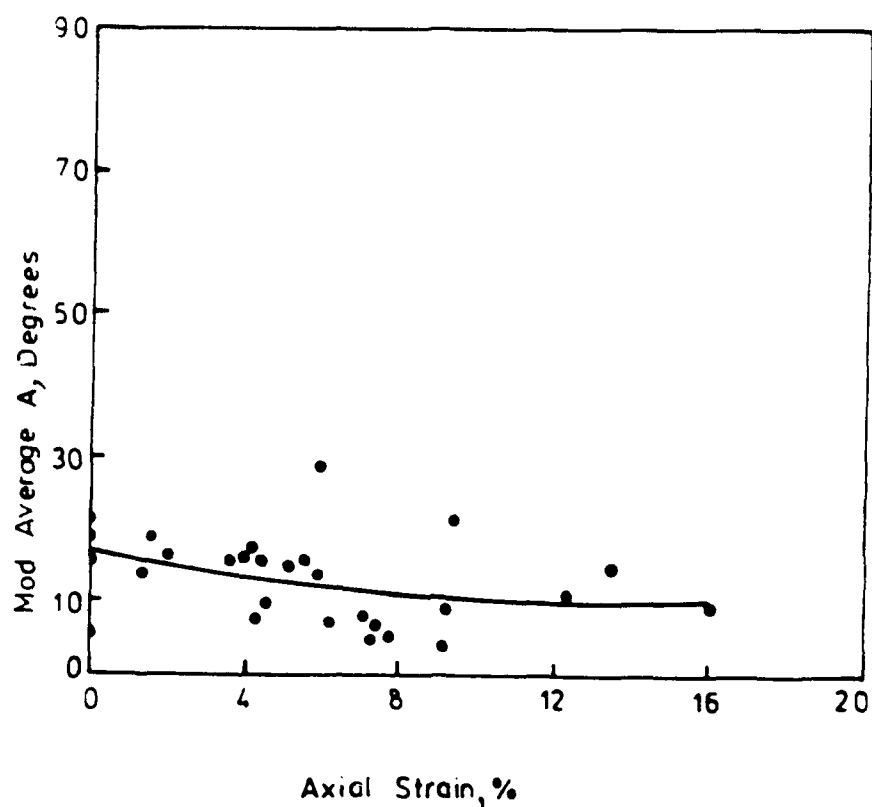
Fig. 5.3 Orientation vs. Axial strain (PMPA ncd).
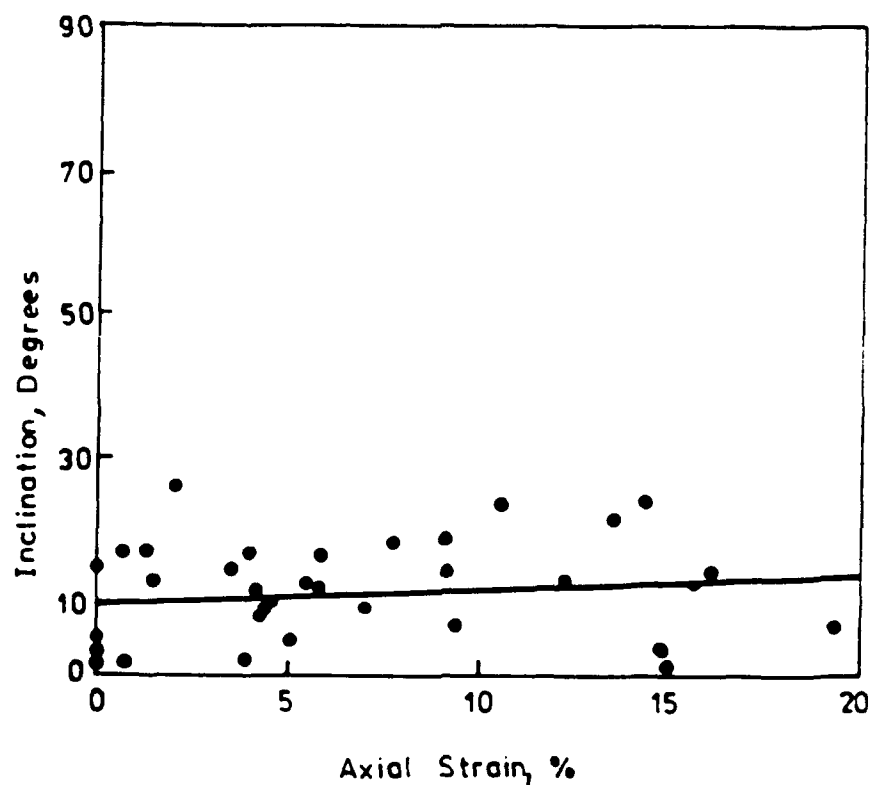
Fig. 5.4 Orientation vs. Axial strain (SEM ncd).
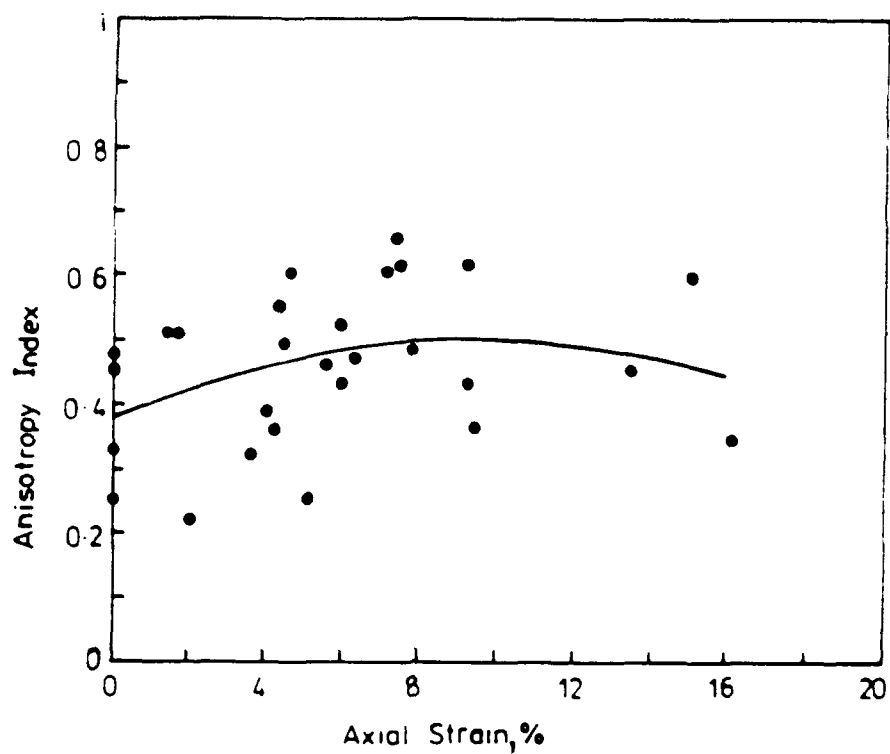
Fig. 5.5   Anisotropy Index vs. Axial strain (PMPA ncd).
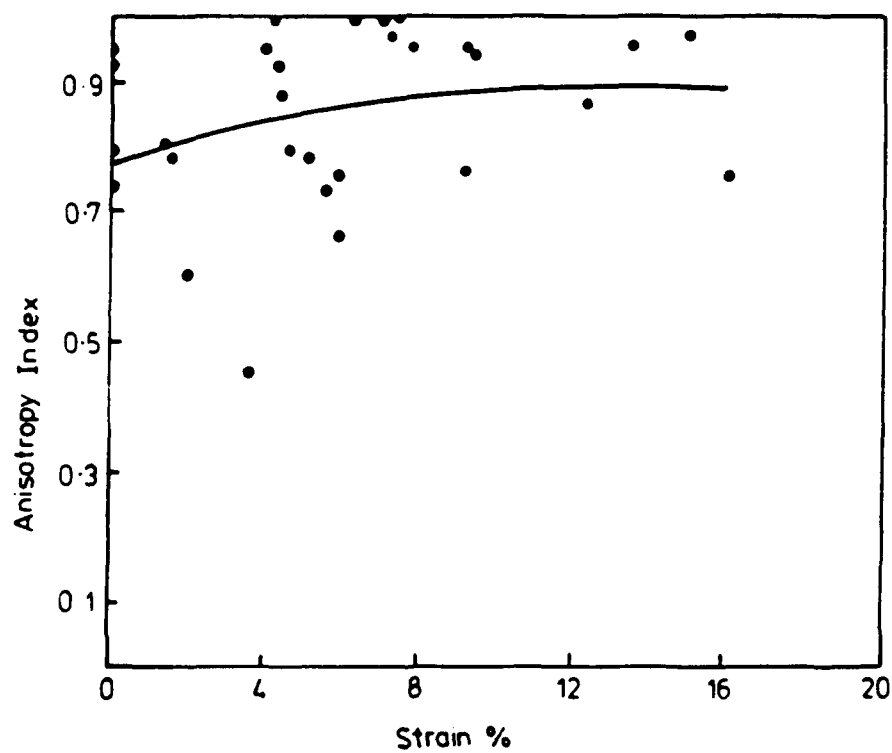
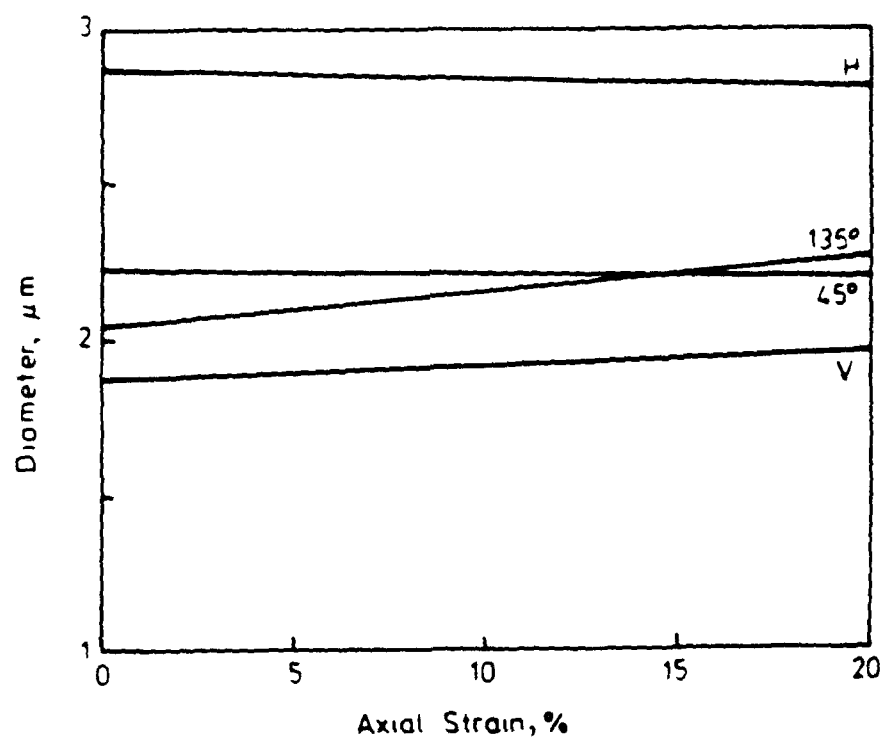Fig. 5.6   Anisotropy Index vs. Axial strain (POLMAP ncd).
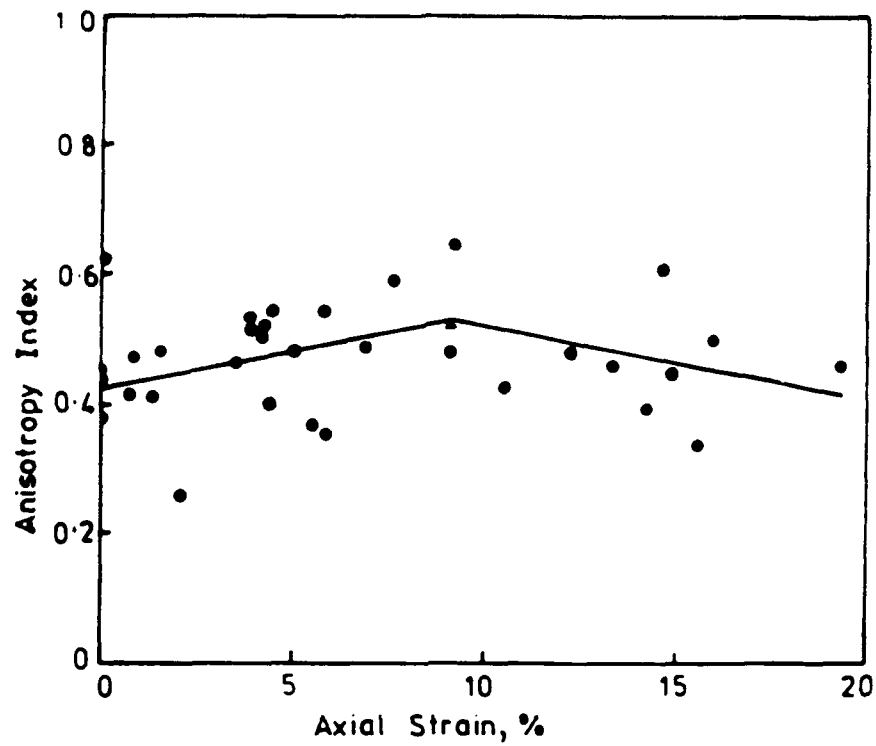
Fig. 5.7   Index of Anisotropy vs. Axial strain (SEM ncd).
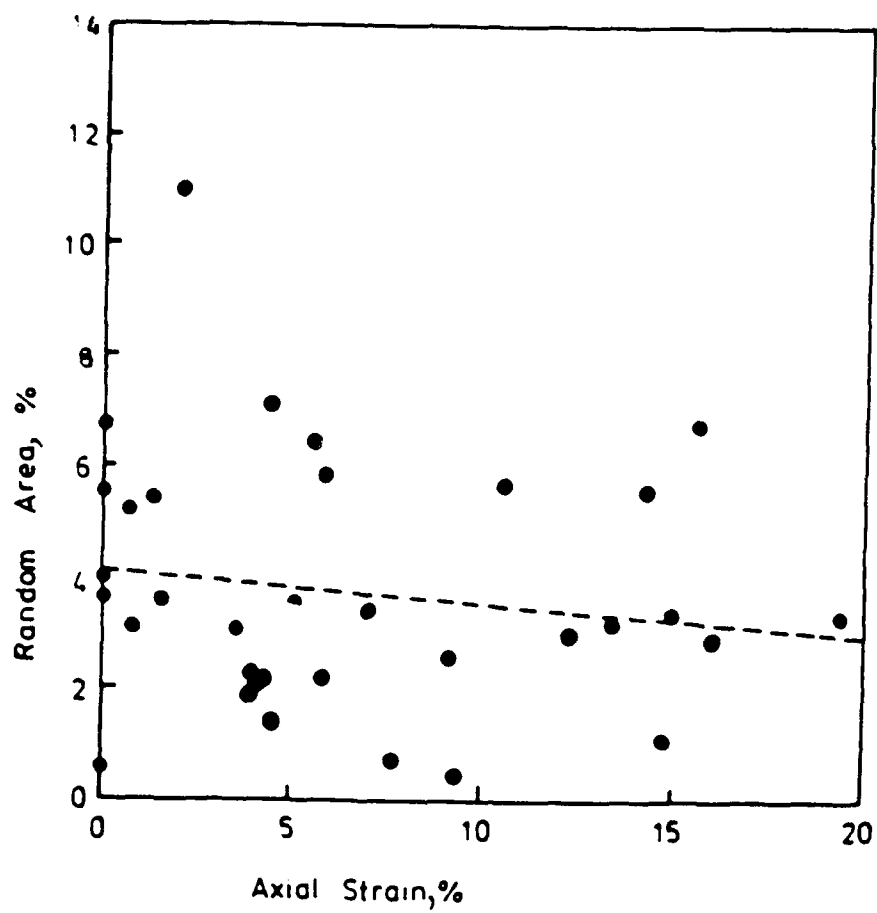
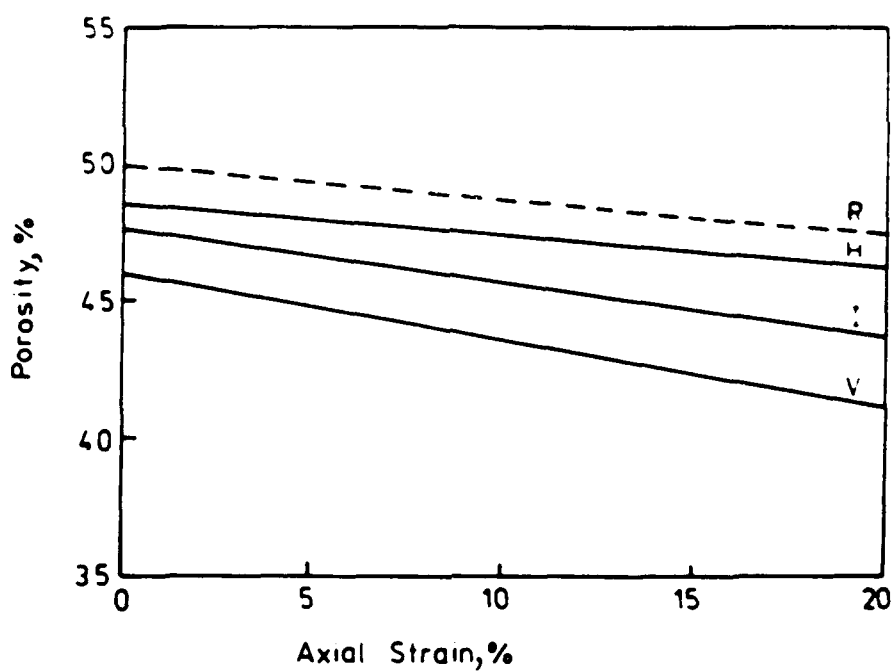Fig. 5.8 Area of random clusters vs. Axial strain (SEM ncd).
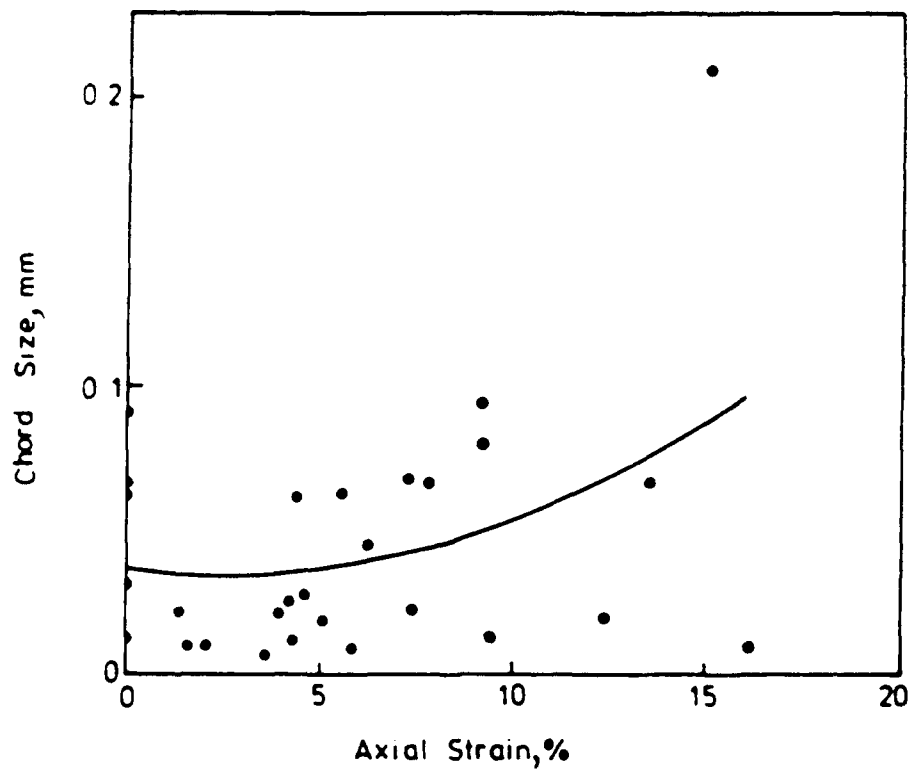
Fig. 5.9 Chord length of patches vs. Axial strain (POLMAP ncd).

Fig. 5.10 Size of domains vs. Axial strain (SEM ncd).
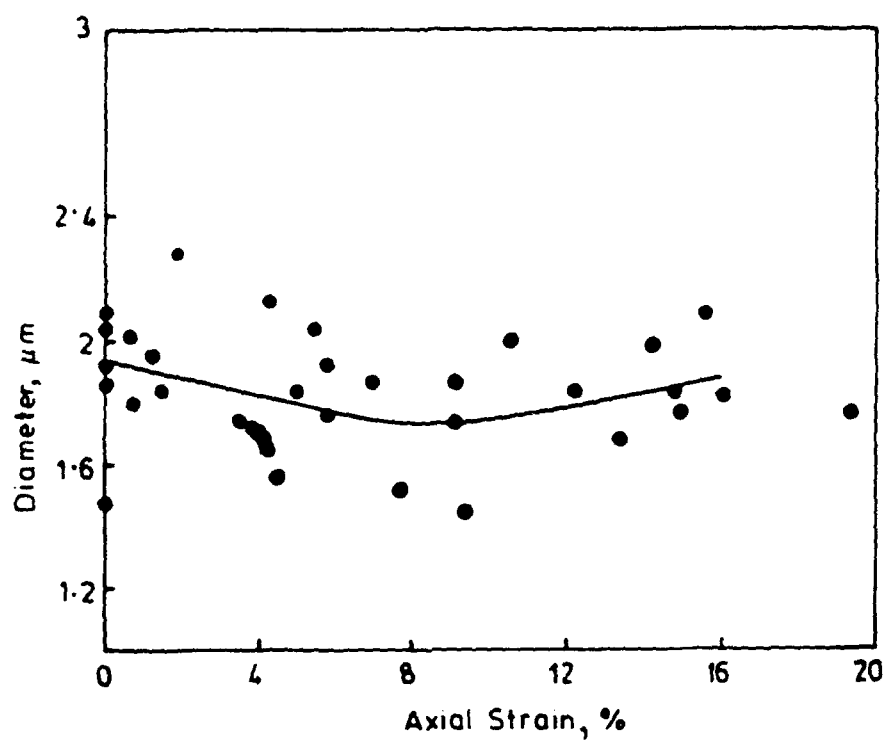
Fig. 5.11 Size of random clusters vs. Axial strain (SEM ncd).
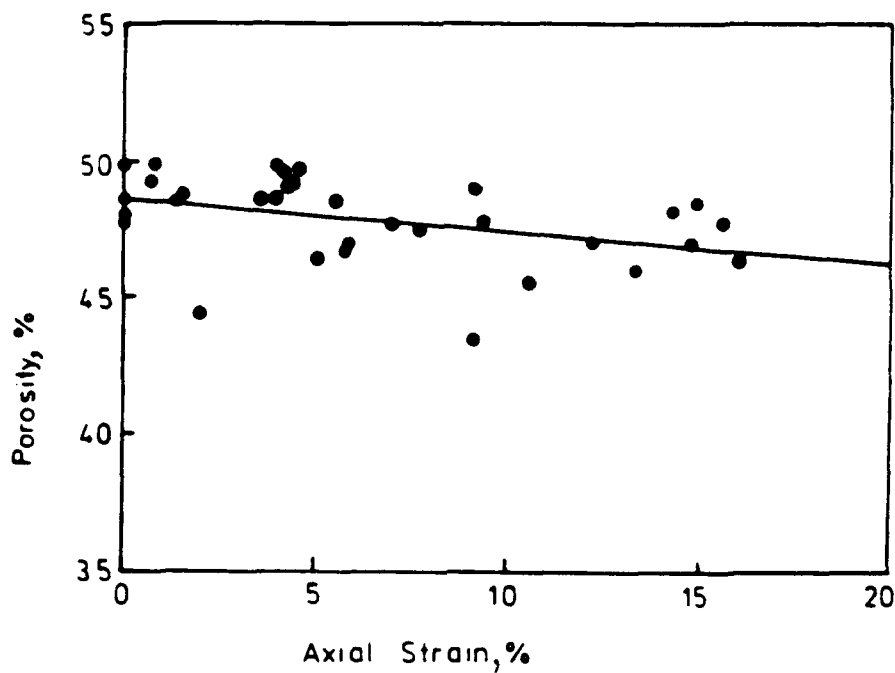
Fig. 5.12 Porosity vs. Axial strain (SEM ncd).
Fig. 5.12.a Horizontal domains.
Fig. 5.12.b H, I, V = horizontal, inclined and vertical domains;
R = random clusters;

OVER-CONSOLIDATED DRAINED TESTS

6.1 INTRODUCTION

After completing the normally consolidated drained triaxial tests, the new methods of micro-analysis were then applied to a series of 35 over-consolidated drained triaxial tests of Speswhite Kaolin after preparation in the medium pressure filter presses. In brief: the slurry was mixed at 140 % moisture content, i.e. 300 % Liquidity Index; consolidated uniaxially to 700 kPa; consolidated triaxially to 700 kPa; allowed to rebound triaxially to 100 kPa; strained at 5 % per day; impregnated with Araldite AY18; and prepared for microscopy. All the samples were examined in the SEM; but some thin sections were lost in the post, so the optical microscopy was performed on 18 samples. Apart from rebound, both the normally consolidated and over-consolidated series of drained tests were identical.

6.2 STRESS-STRAIN BEHAVIOR

Fig. 6.1 illustrates the deviator stress vs. axial strain for a typical sample from the over-consolidated drained series. There was a steady rise of deviator stress to about 8 % axial strain, at about which strain failure occurred, there being a small amount of variability from sample to sample. The volumetric strain was small, well less than 1 % expansion, and there was some difficulty in measuring it exactly. It should be taken that it rose steadily from the start, perhaps leveling off after about 1-2 % axial strain.

6.3 SCANNING ELECTRON MICROSCOPY

Visual examination of the scanning electron micrographs showed that the structure of the samples was composed mainly of diffuse domains, which tended to merge together. As indicated below, there were a few random clusters; but there were virtually no inter-domain voids in these samples. Thus, the hypothesis that shear deformation is accommodated by slip of domains into the inter-domain voids is irrelevant here; but there could still have been slip of the domains into the looser and presumably weaker random areas.

Failure planes, when they occurred, were slickensided as usual and cut through the previously-existing structure non-conformably; however, attention here is concentrated on the 'pre-peak' deformation.

6.4 PREFERRED ORIENTATION

Fig. 6.2 shows the preferred orientation vs. axial strain obtained from the polarizing micro-photometric analysis, PMPA. Here and in the graphs following, each point is the end point of one test. The results in this figure are the moduli of the algebraical average of the five values of orientation obtained from the five fields measured by this technique, and they are expressed as inclinations from the horizontal. Fig. 6.3 shows the corresponding values obtained from scanning electron microscopy. All the values in both graphs are low: i.e. the preferred orientation started close to the horizontal and remained close to the horizontal throughout. Thus, the hypothesis that the particles would gradually rotate into the direction of the failure plane is eliminated.

6.5 STRENGTH OF ANISOTROPY

Figs. 6.4, 6.5, and 6.6 show the strength of anisotropy vs. axial strain measured by PMPA, POLMAP, and SEM, respectively. Each point is the arithmetical average of Anisotropy Index for 5, 4, and 24 fields, respectively.

In the first and last of these three graphs, the Anisotropy Index starts at a moderate value and ends at a moderate value. This is in accordance with the hypothesis that, during shear deformation, strongly anisotropic samples become less anisotropic and weakly anisotropic samples become more anisotropic; these samples appear to be on the borderline. The values from POLMAP tend to be higher throughout.

All three graphs appear to show a very slight increase in anisotropy, and the standard deviations for SEM appear to show a very slight decrease in variability within the samples.

6.6 RANDOM CLUSTERS

Random clusters of clay plates were also mapped in the scanning electron micrographs. Fig. 6.7 shows the area of random clusters vs. axial strain. The total random area is fairly small, and there appears to be a slight decrease, which would agree with the slight increase in anisotropy.

6.7 SIZES OF FEATURES

Fig. 6.8 shows the average chord length of the areas mapped using POLMAP vs. axial strain, the trend, if any, being slightly upwards or concave down.

Fig. 6.9 illustrates the average size of the domains mapped in the scanning electron micrographs vs. axial strain. Trend lines are shown for horizontal and vertical domains. There appears to have been a very slight increase in the sizes of these domains.

6.8 POROSITY

Fig. 6.10 illustrates the porosity of some of the features mapped in the scanning electron micrographs vs. axial strain. The results here were obtained from the scanning electron micrographs after Wiener filtering and thresholding to obtain a binary 'solid-or-pore' image. There appears to have been a very slight decrease in porosity with strain; and this occurred more in the vertical domains than in the horizontal ones.

6.9 SUMMARY

Up to 8 % axial strain say: the lateral strain was almost negligible; the preferred orientation remained horizontal; the strength of anisotropy appeared to increase slightly; the area of random clusters appeared to decrease; the sizes of the domains appeared to increase slightly; and the sizes of the areas mapped by optical microscopy scarcely varied. All this suggests very slight bedding down of the microstructure, with groups of particles turning somewhat closer to the horizontal, and perhaps some oriented domains pushing into random areas. The mechanisms here are very similar to those in the normally consolidated drained series in the same range of axial strain, and they are again distinct from the formation of failure planes.

-----oooooOooooo-----
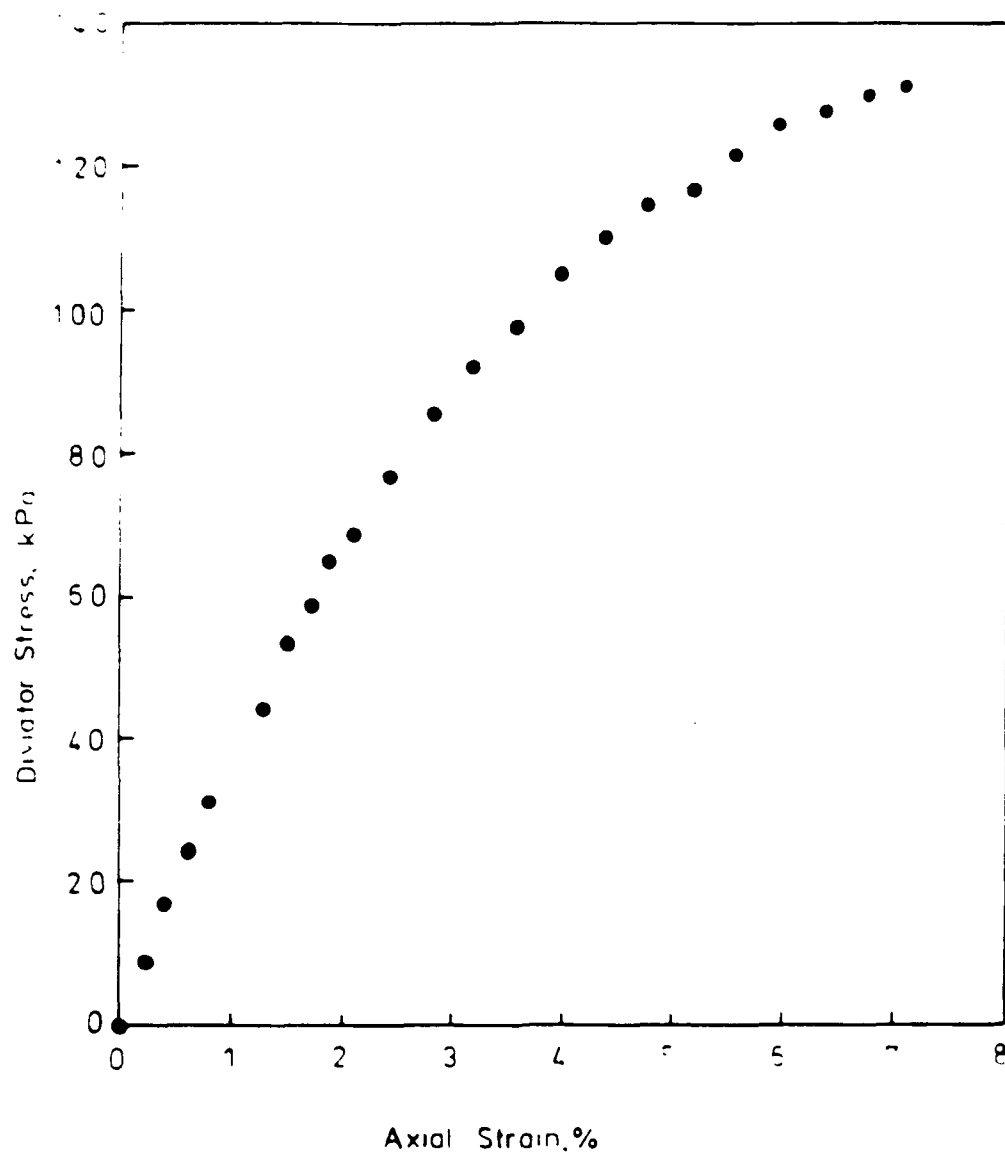
Fig. 6.1 Deviator stress vs. Axial strain (oc).
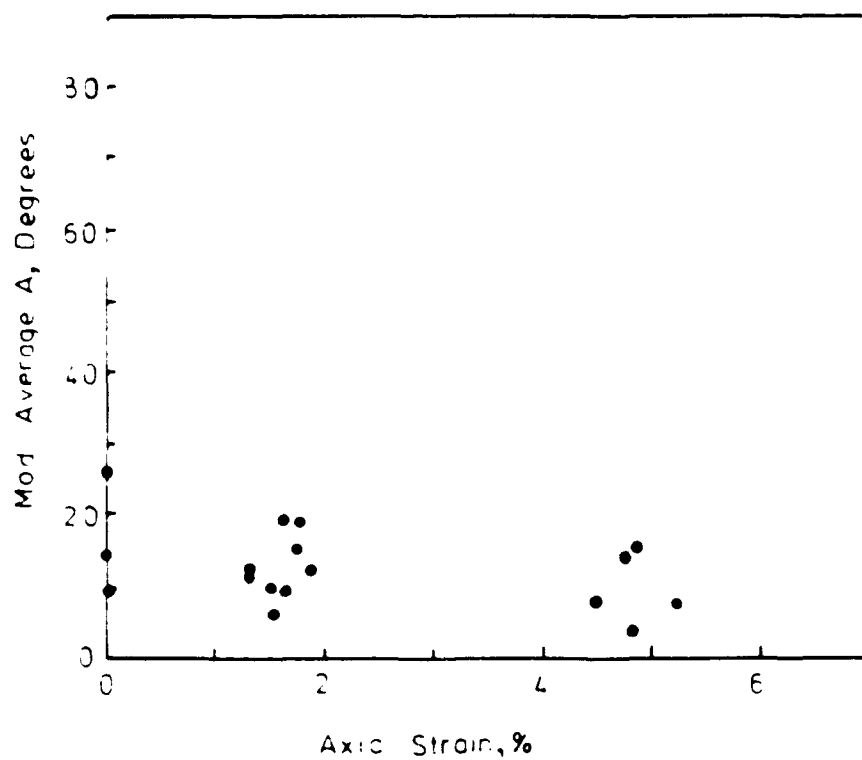
Fig. 6.2 Orientation vs. Axial strain (PMPA oc).
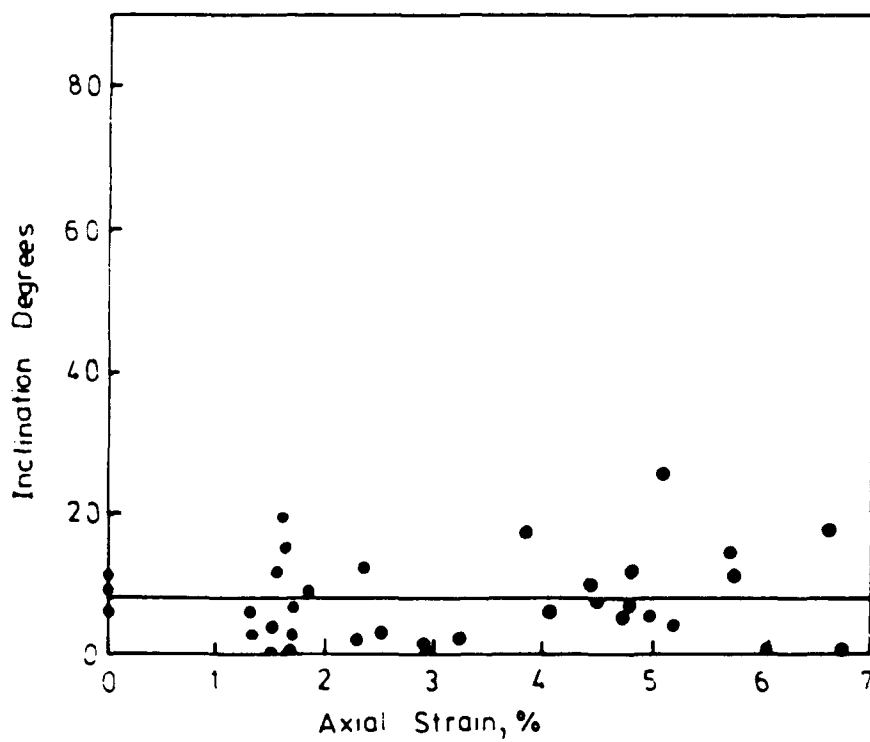
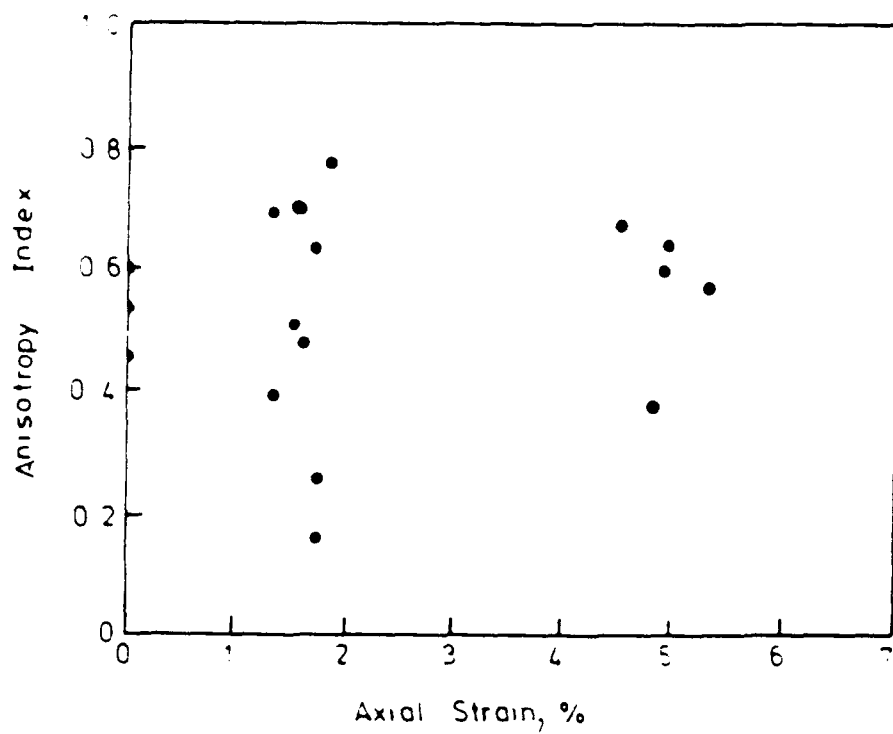Fig. 6.3 Orientation vs. Axial strain (SEM oc).

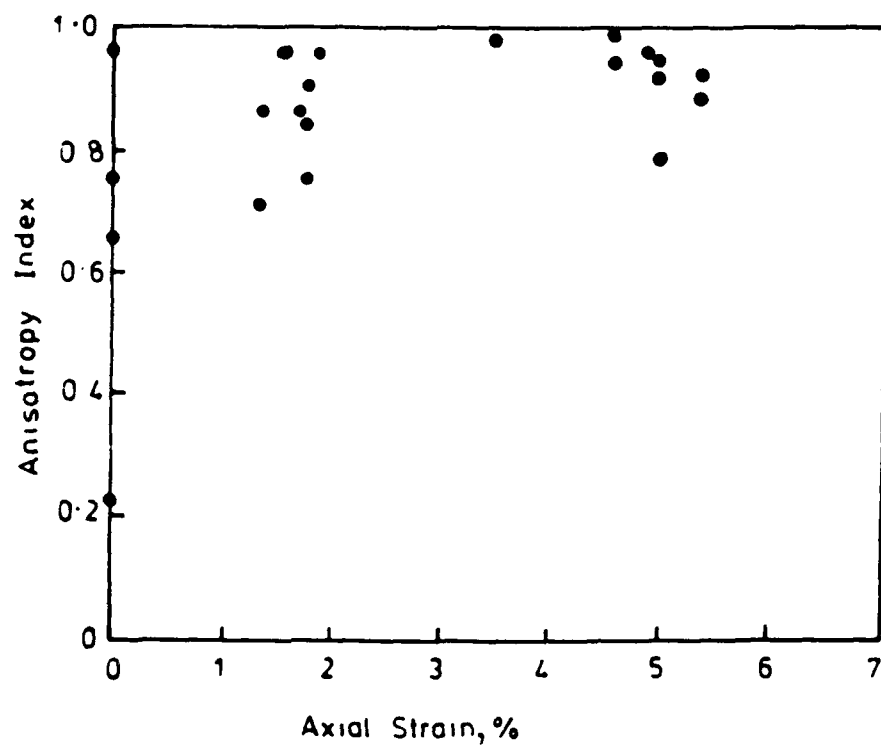Fig. 6.4 Anisotropy Index vs. Axial strain (PMPA oc).

Fig. 6.5 Anisotropy Index vs. Axial strain (POLMAP oc).
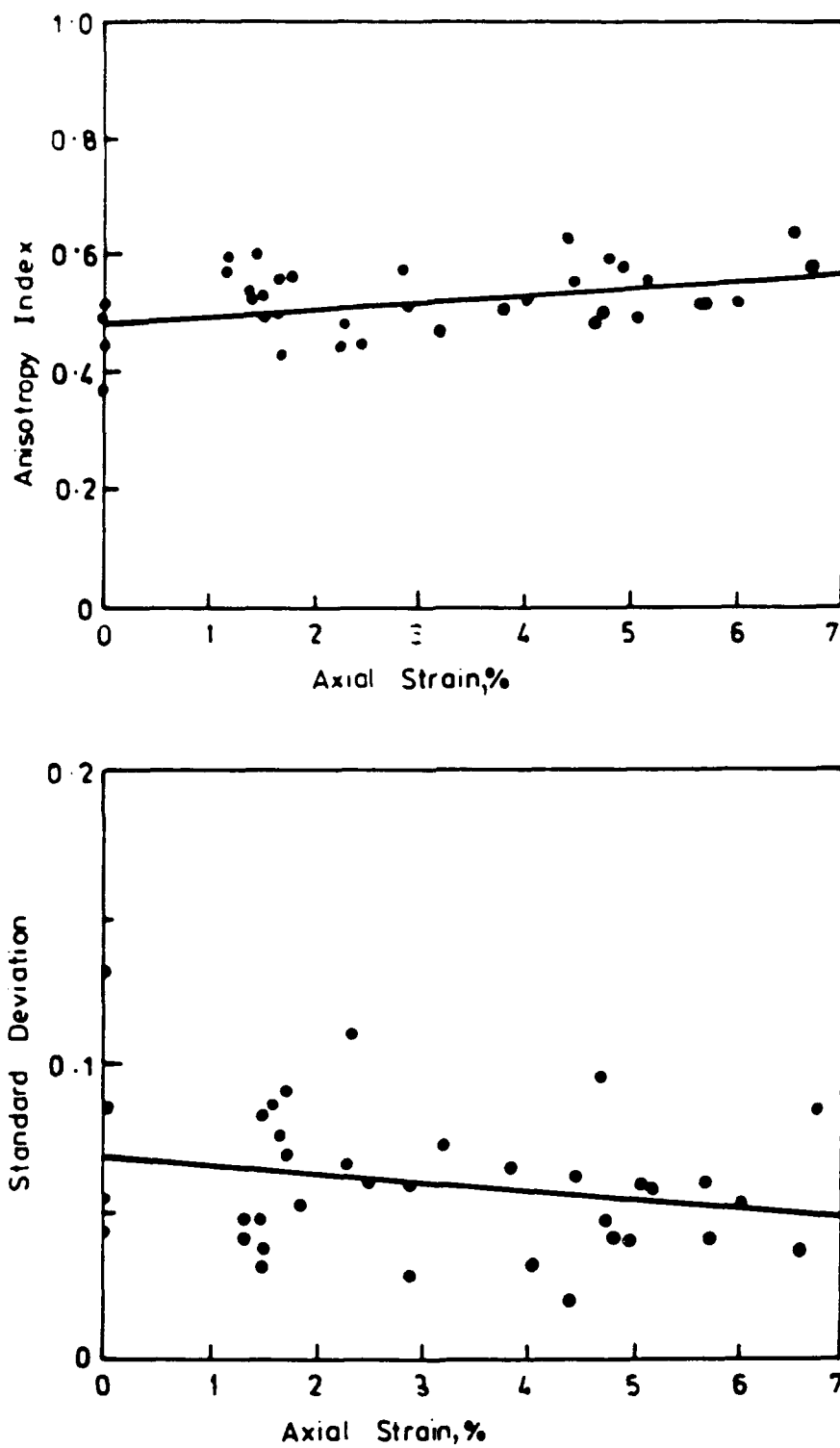
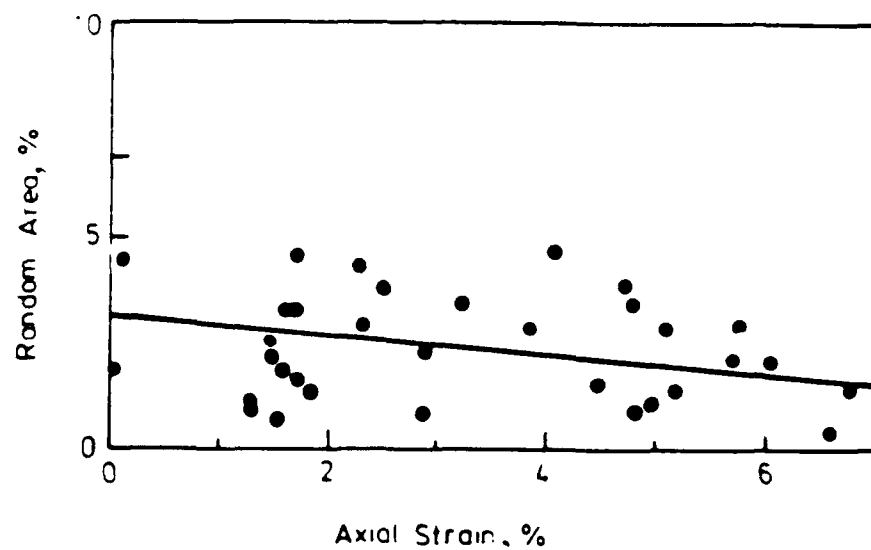Fig. 6.6   Index of Anisotropy vs. Axial strain (SEM oc).

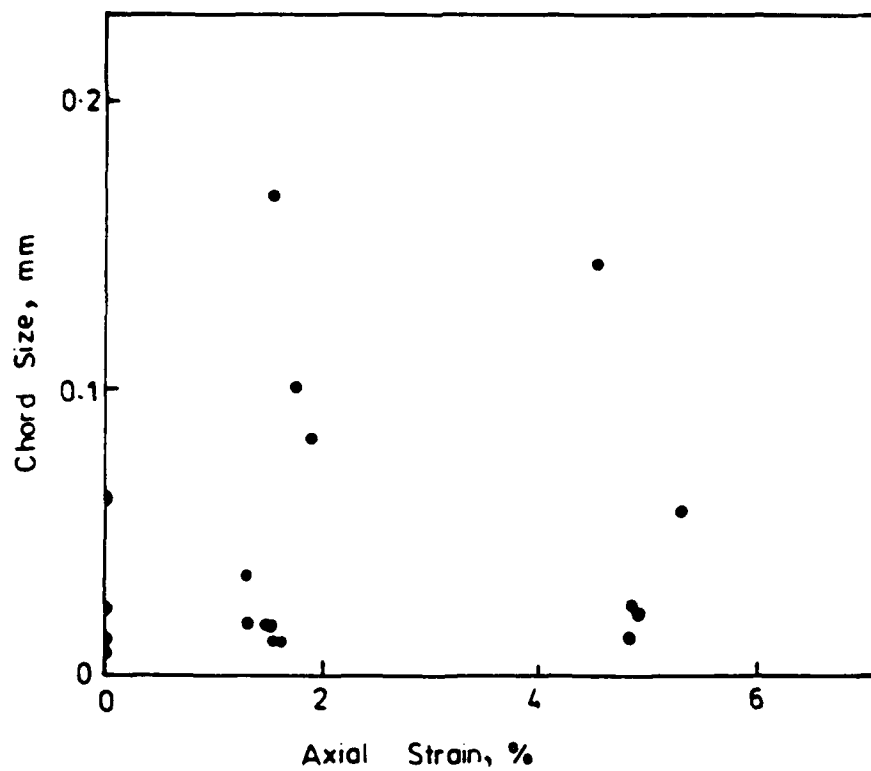Fig. 6.7 Area of random clusters vs. Axial strain (SEM oc).

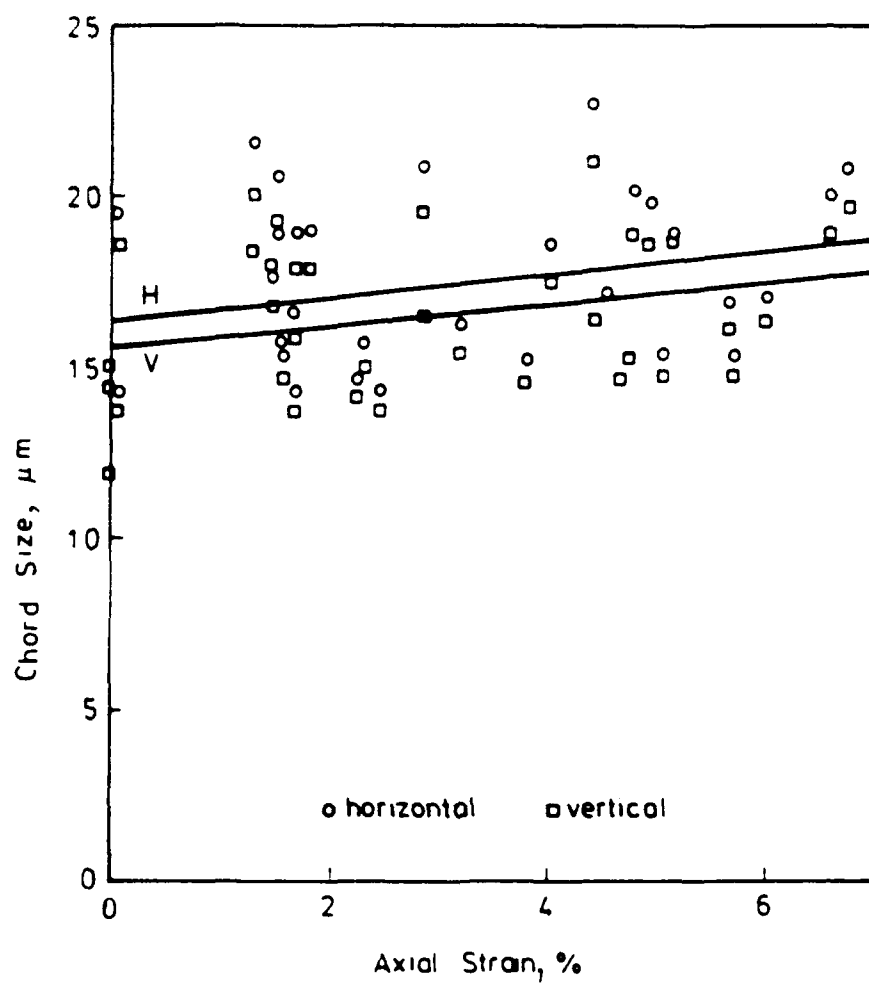Fig. 6.8 Chord length of domains vs. Axial strain (POLMAP oc).

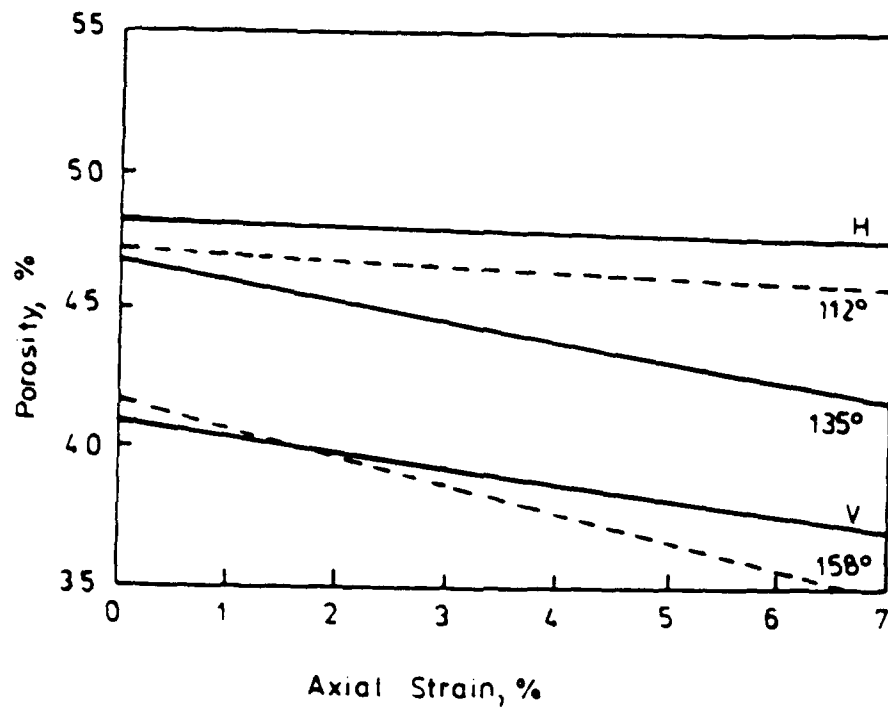Fig. 6.9   Size of domains vs. Axial strain (SEM oc).

Fig. 6.10   Porosity vs. Axial strain (SEM oc).

NORMALLY-CONSOLIDATED UNDRAINED TESTS

7.1 INTRODUCTION

The third series of tests to be considered is a series of 35 normally con-
solidated undrained triaxial tests of Speswhite Kaolin after preparation in
the original low pressure filter presses. The kaolin, although nominally
identical to that used in the other two series, was slightly different. In
brief: the slurry was mixed at 120 % moisture content, i.e. 2.56 % Liquidity
Index; consolidated uniaxially to 100 kPa; consolidated triaxially to 650 kPa;
strained at 0.15 mm/min under 50 kPa backpressure; impregnated with Vestopal
W; and prepared for microscopy.

7.2 STRESS-STRAIN BEHAVIOR

Fig. 7.1 illustrates the deviator stress vs. axial strain for three typical
samples from the normally consolidated undrained series. the results being
much as expected, i.e. a steady rise of deviator stress to a peak value at say
8 % axial strain. followed by a more-or-less steady stress to say 16 % axial
strain, at about which strain failure occurred. Confidence Limits for the
whole series are shown on the diagram: the spread of these at high strains is
due in part to the smaller number of samples which were tested to these high
strains.

7.3 VISUAL EXAMINATION

Visual examination in the polarizing microscope showed that a certain
anisotropy had developed during the preparation of the filter cake and that
most of the particles had turned into the horizontal direction: but, after
triaxial consolidation, a blotchy appearance could be seen between crossed
polars, and the particles were arranged somewhat randomly.

Visual examination of the scanning electron micrographs showed that the struc-
ture of the samples was composed mainly of diffuse domains, which tended to
merge together. As indicated below,there were a few random clusters: but there
were virtually no inter-domain voids in these samples. Thus, the hypothesis
that shear deformation is accommodated by slip of domains into the inter-
domain voids is irrelevant here; but there could still have been slip of the
domains into the looser and presumably weaker random areas.

Failure planes, when they occurred, were slickensided as usual and cut through
the previously-existing structure non-conformably; however, attention here is
concentrated on the 'pre-peak' deformation.

The measurements discussed below were taken on fields as follows:

PMPA   1.5 mm diameter
POLMAP   0.47 mm square
SEM   0.025 mm square

7.4 PREFERRED ORIENTATION

Fig. 7.2 shows the preferred orientation vs. axial strain obtained from the
polarizing micro-photometric analysis, PMPA. Here and in the graphs following,
each point is the end point of one test. Here and in the following graphs,
quadratic regressions have been added. Although these regressions were not
shown to be significant, presumably because these graphs show a larger scatter
than had been anticipated from previous studies when the experiment was
planned, many of the graphs show the same trends. The results in Fig. 7.2 are
the moduli of the algebraical average of the five values of orientation
obtained from the five fields measured by this technique, and they are
expressed as inclinations from the horizontal. The values for the averages of
the five moduli were slightly higher, and their trend was slightly upwards,
Fig. 7.3. The trends for the sets of four measurements obtained from POLMAP
are shown in Fig. 7.3. Fig. 7.4 shows the values obtained from scanning elec-
tron microscopy using intensity gradient analysis followed by consistency
ratio smoothing, PICCON; and Fig. 7.5 shows the values obtained from the
porosity/density maps by using intensity gradient analysis on these maps, PIC-
POR. All the values in these four graphs are low; i.e. the preferred orienta-
tion started close to the horizontal and remained close to the horizontal
throughout. Thus, the hypothesis that the particles would gradually rotate
into the direction of the failure plane is eliminated; on the contrary, the
trend being concave up suggests that during the early stage of the tests, up
to 8 % axial strain say, the particles are turning towards the horizontal, and
that during the late stage of the tests, from 8 - 16 % axial strain say, some
of the particles may be turning away from the horizontal.

7.5 STRENGTH OF ANISOTROPY

Figs. 7.6, 7.7, 7.8, and 7.9 show the strength of anisotropy vs. axial strain
measured by PMPA, POLMAP, PICCON and PICPOR, respectively. Each point in the
first two graphs is the arithmetical average of Anisotropy Index for 5 and 4
fields, respectively; and each point in the other two graphs is the composite
value of Consistency Ratio for 25 fields.

In all four graphs, the Anisotropy Index or Consistency Ratio starts at a mod-
erate value and ends at a moderate value. This is in accordance with the
hypothesis that, during shear deformation, strongly anisotropic samples become
less anisotropic and weakly anisotropic samples become more anisotropic; these
samples appear to be on the borderline.

All four graphs do seem to show a strengthening of anisotropy during the early
stages of the tests, and a weakening of anisotropy during the late stages of
the tests.

The values from POLMAP were interesting in that the between-samples
variability seemed to increase with strain; this point is discussed further
below.

Another interesting feature is that the strength of anisotropy based on the
density maps of PICPOR is much lower than that based on the orientation maps
of PICCON: this raises the suggestion that the anisotropic mechanical proper-
ties of the samples may be due to the anisotropy of density rather than to the
anisotropy of orientation. This point deserves further study.

7.6 SIZES OF FEATURES

Fig. 7.10 shows the average chord length of the areas mapped using POLMAP vs.
axial strain, the trend apparently being concave downwards; however, the
observers were not altogether convinced that the strong downward trend of the
quadratic regression did represent what they had seen.

Figs. 7.11 and 7.12 illustrate the average size of the features mapped in the
scanning electron micrographs by PICCON and PICPOR, respectively. Strain
appears to have had negligible effect on the sizes of these features; thus,
both the hypothesis that the domains would increase in size and the hypothesis
that the domains would break up and decrease in size with shear appear to be
eliminated.

7.7 POROSITY

The relationship between porosity and strength of anisotropy was investigated
on a pixel-by-pixel basis. For all the pixels in all 25 images of each set,
the local values of Consistency Ratio and of porosity were taken from the
smoothing filter; and regressions of one on the other were calculated. It was
found that the more strongly oriented domains were the denser.

A trial analysis by hand on a few micrographs suggested that the denser parts
of the samples contained larger domains than did the looser parts.

Taken together, these observations suggested the possibility that the micro-
deformations were concentrated in the looser parts of the samples, the denser
parts remaining unaltered.

7.8 BETWEEN-SAMPLES VARIABILITY

Figs. 7.13 and 7.14 show the between-samples standard deviations for strength
of anisotropy and for chord sizes obtained from the optical microscopy calcu-
lated by placing the samples in groups with approximately equal strains cor-
responding to the vertices on the graphs. These graphs suggest that the
variability between samples increased as strain increased.

7.9 SUMMARY

During the early stage of shear deformation, up to 8 % axial strain say: the
preferred orientation remained close to the horizontal; the strength of
anisotropy seemed to increase; the sizes of the domains apparently remained
constant; and the sizes of the areas mapped by optical microscopy sometimes
increased.

During the late stage of shear deformation, from ? to ?% axial strain say:
the preferred orientation remained horizontal, but the strength of anisotropy
seemed to decrease: the sizes of the domains apparently remained constant, but
the sizes of the areas mapped by optical microscopy seemed sometimes to
increase: and the between-samples variability apparently increased.

This suggests that particles or domains are beginning to rotate away from the
horizontal, but with equal quantities turning upwards and downwards: and that
these rotations caused slight disruption to the structure. The optical micro-
scopy suggests that there may perhaps have been a tendency to medium-scale
organization, with domains in one part tending all to turn one way, and with
domains in an adjacent part tending all to turn the other way.

In summary, therefore, the observations suggest that three different
mechanisms were acting: one in the early stage of shear deformation as the
samples bedded down: the other in the late stage of shear deformation as the
samples began to be disrupted: and both these mechanisms were distinct from
the formation of failure planes. There may also have been some form of struc-
tural instability, such that samples which were nominally identical actually
behaved somewhat differently.

The questions of the relative importance of anisotropy of density and
anisotropy of orientation and of the relative roles of the denser and looser
parts of the structure might well form the subject of further studies.
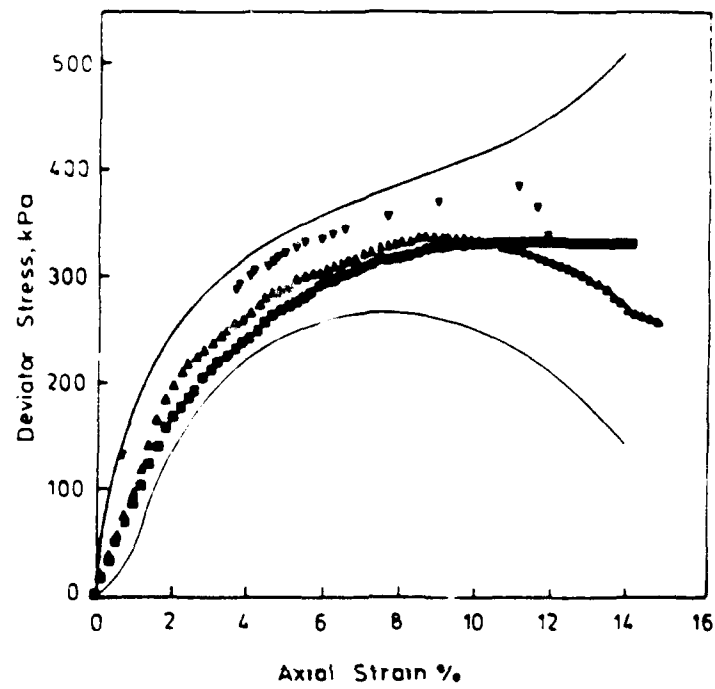

-----ooooo0ooooo-----

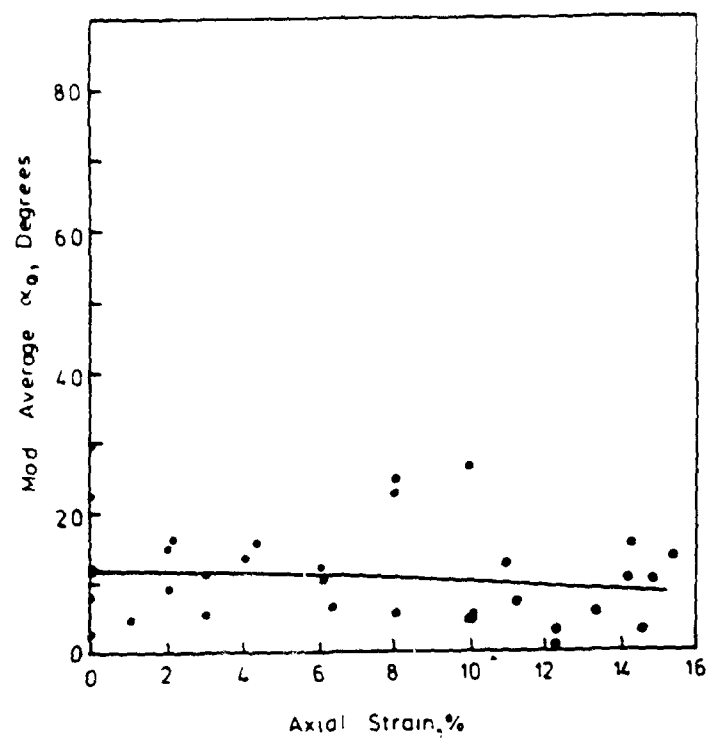Fig. ⁻.1   Deviator stress vs. Axial strain (ncu).

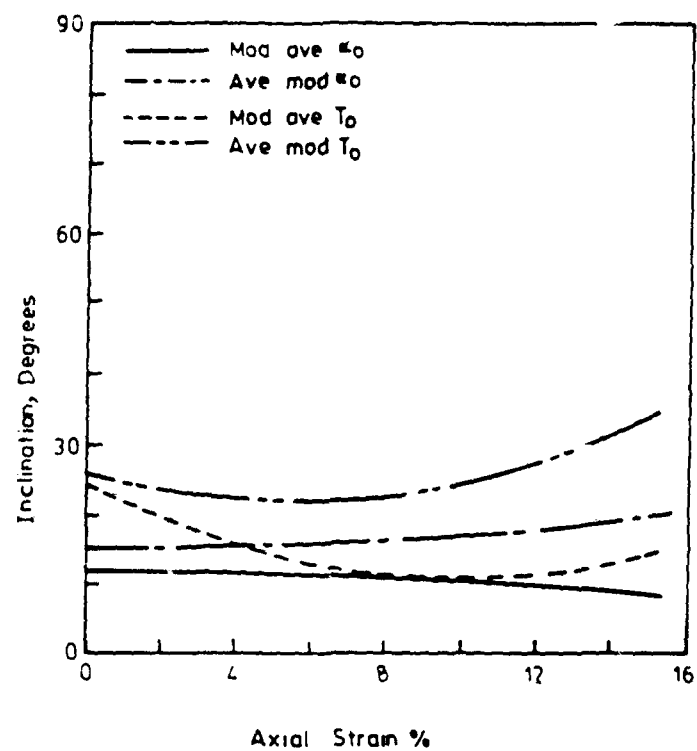Fig. 7.2 Orientation vs. Axial strain (PMPA ncu).

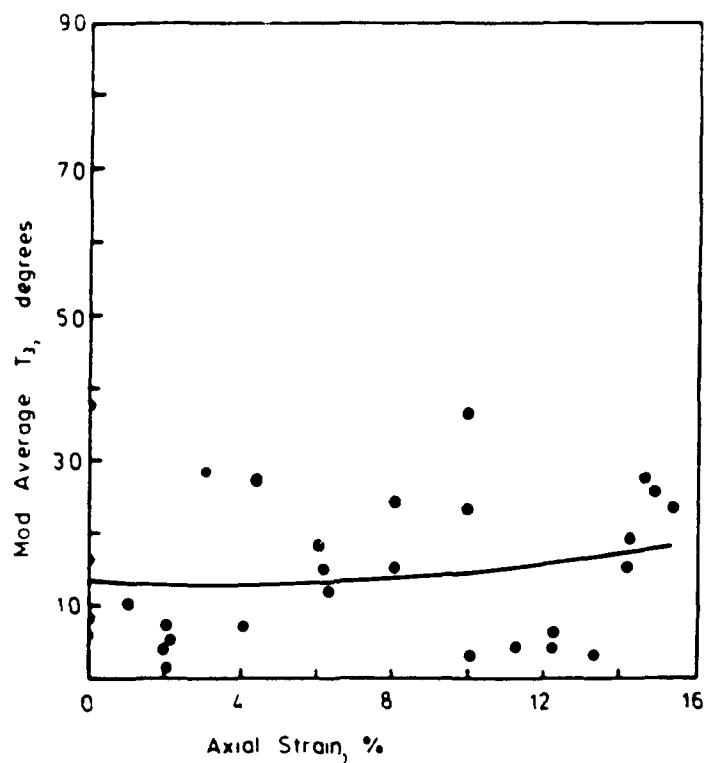Fig. 7.3 Orientation vs. Axial strain (PMPA and POLMAP ncu).

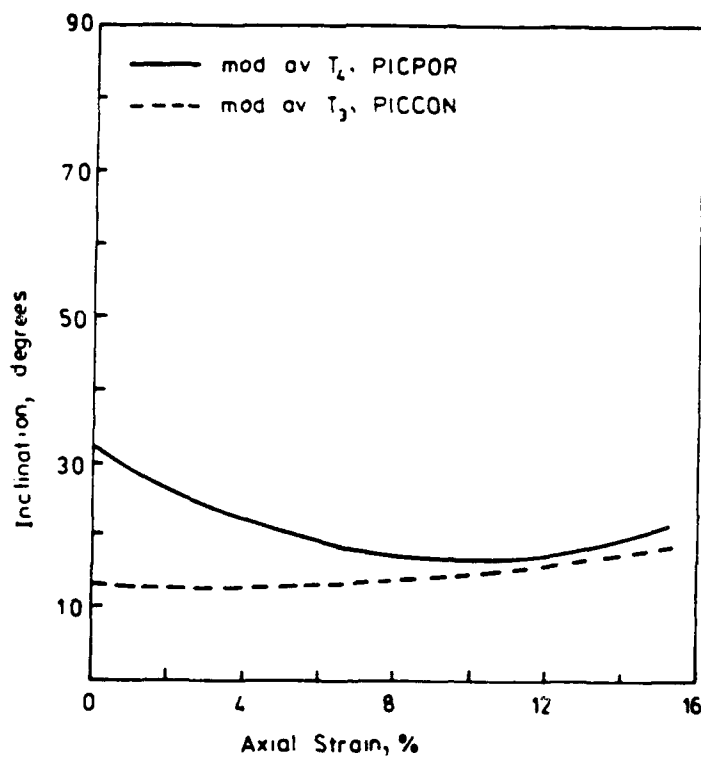Fig. 7.4 Orientation vs. Axial strain (SEM PICCON ncu).

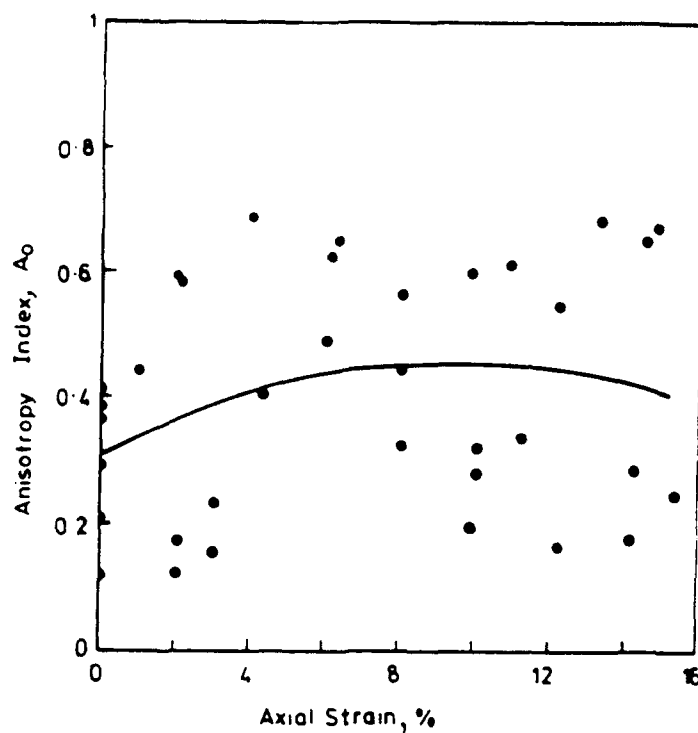Fig. 7.5 Orientation vs. Axial strain (SEM PICPOR ncu).

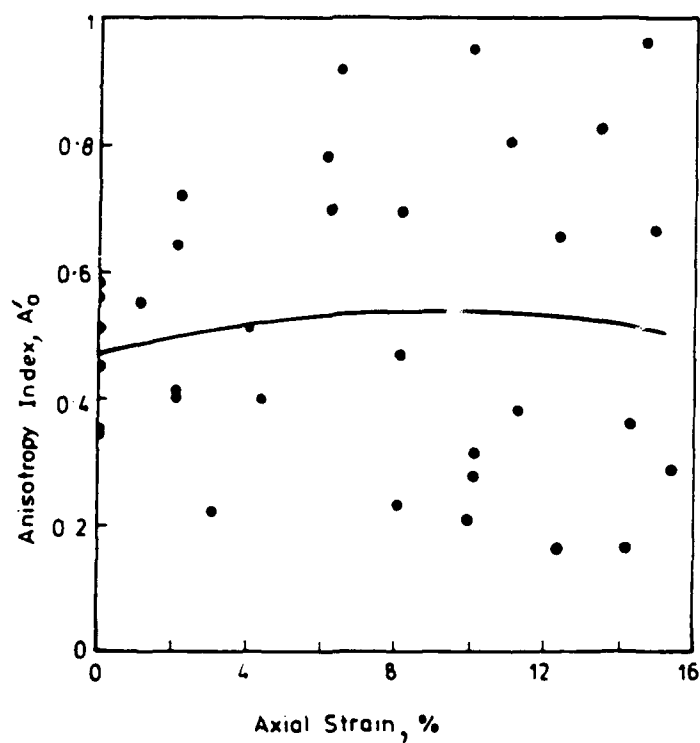Fig. 7.6   Anisotropy Index vs. Axial strain (PMPA ncu).

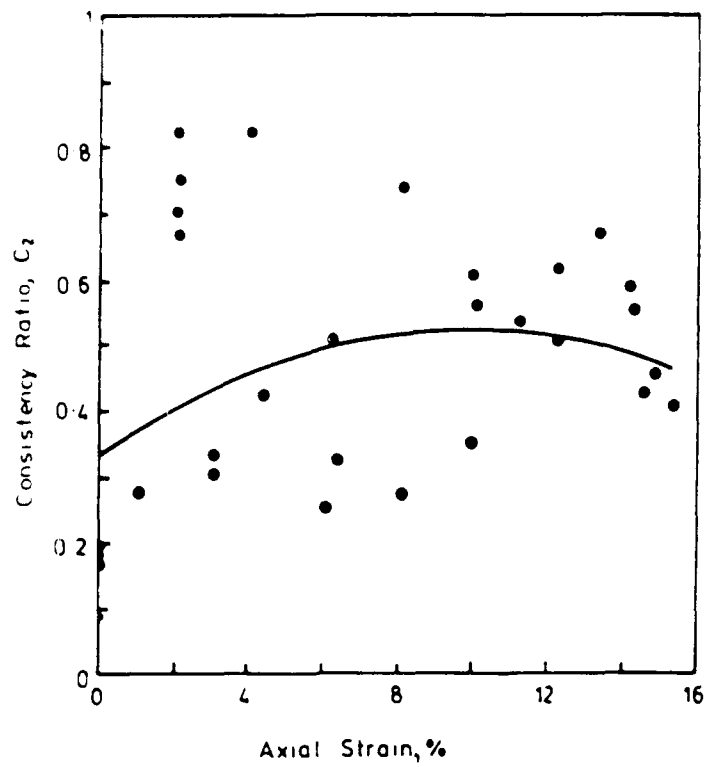Fig. 7.7   Anisotropy Index vs. Axial strain (POLMAP ncu).

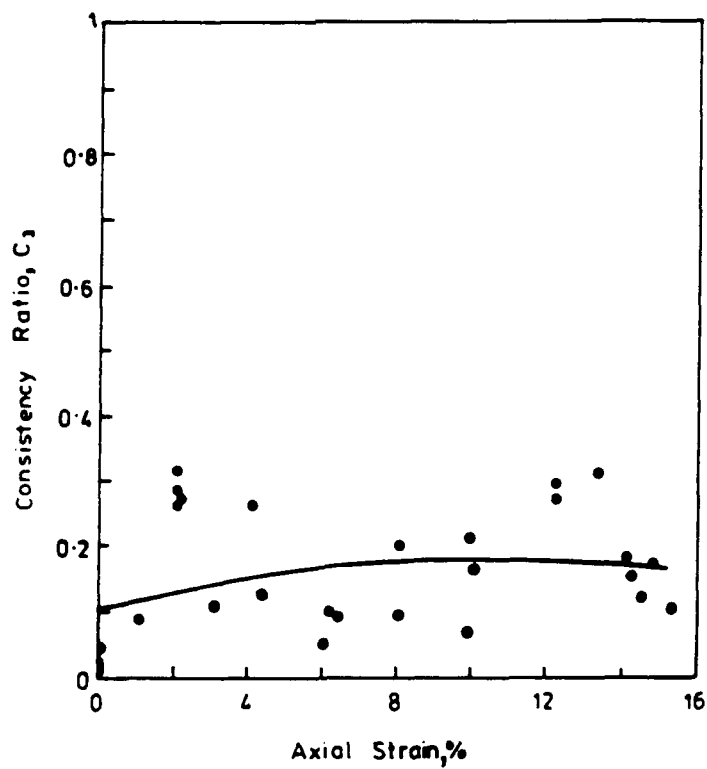Fig. 7.8 Consistency Ratio vs. Axial strain (SEM PICCON ncu).

Fig. 7.9 Consistency Ratio vs. Axial strain (SEM PICPOR ncu).
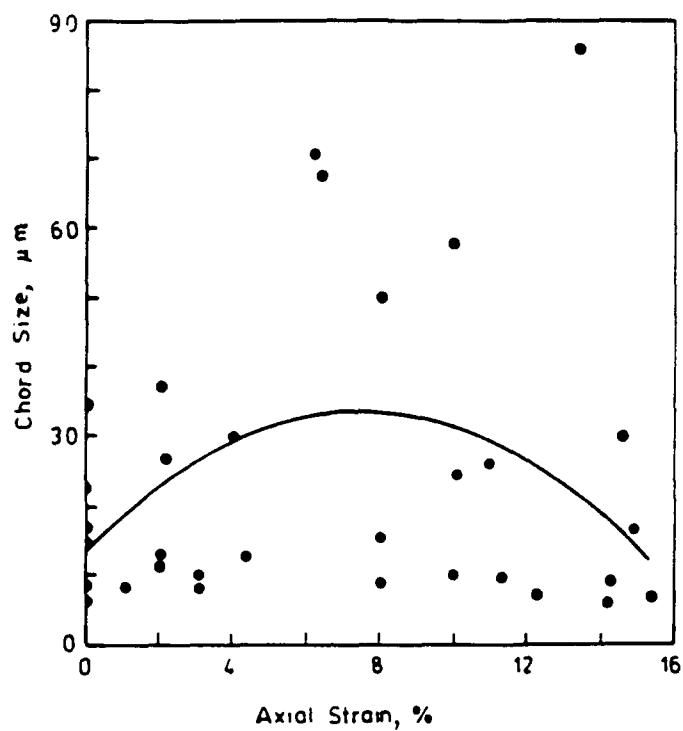
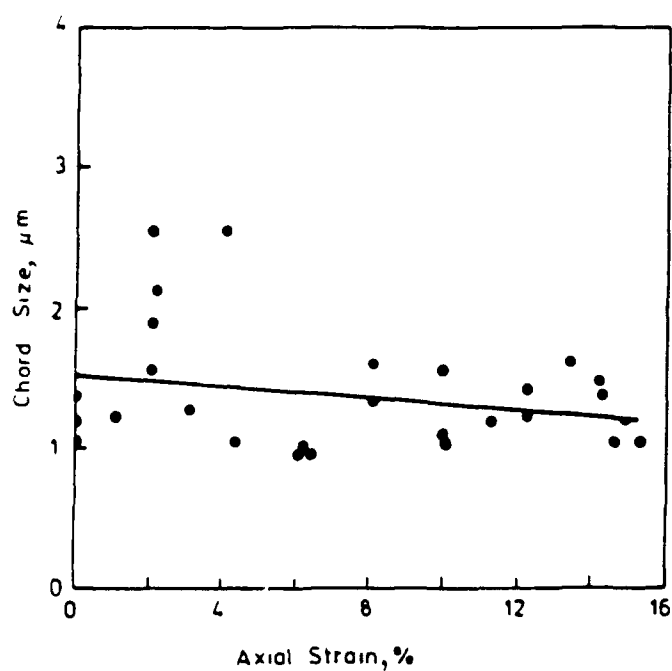Fig. 7.10   Size of patches vs. Axial strain (POLMAP4 ncu).

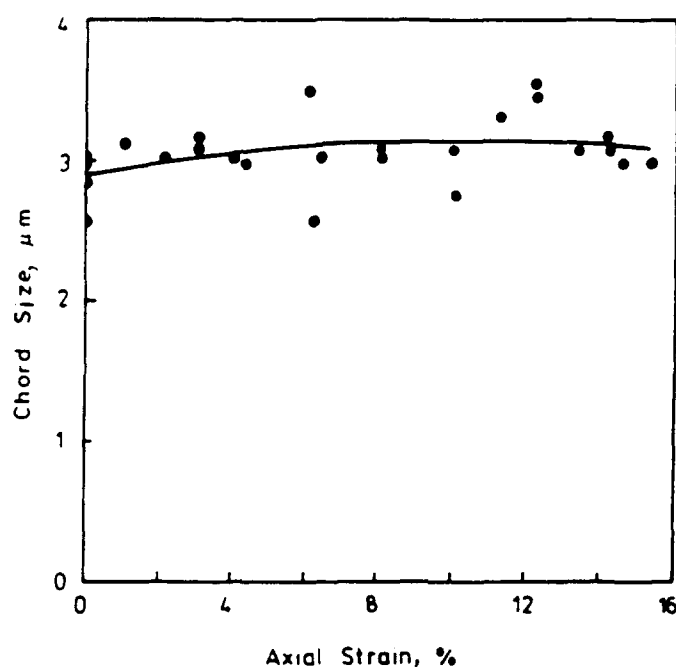Fig. 7.11 Size of domains vs. Axial strain (SEM PICCON ncu).

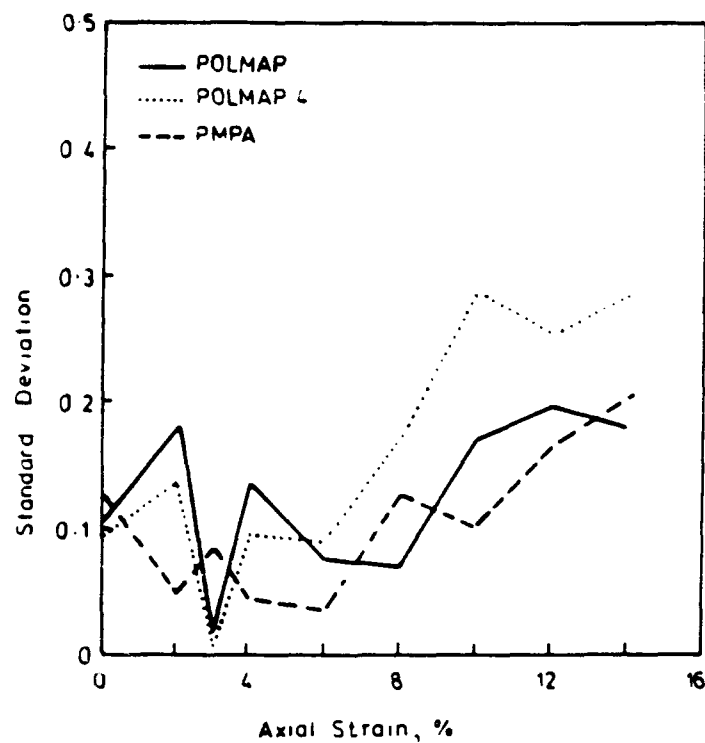Fig. 7.12 Size of features vs. Axial strain (SEM PICPOR ncu).

Fig. 7.13 Between-samples standard deviation of anisotropy vs. Axial strain
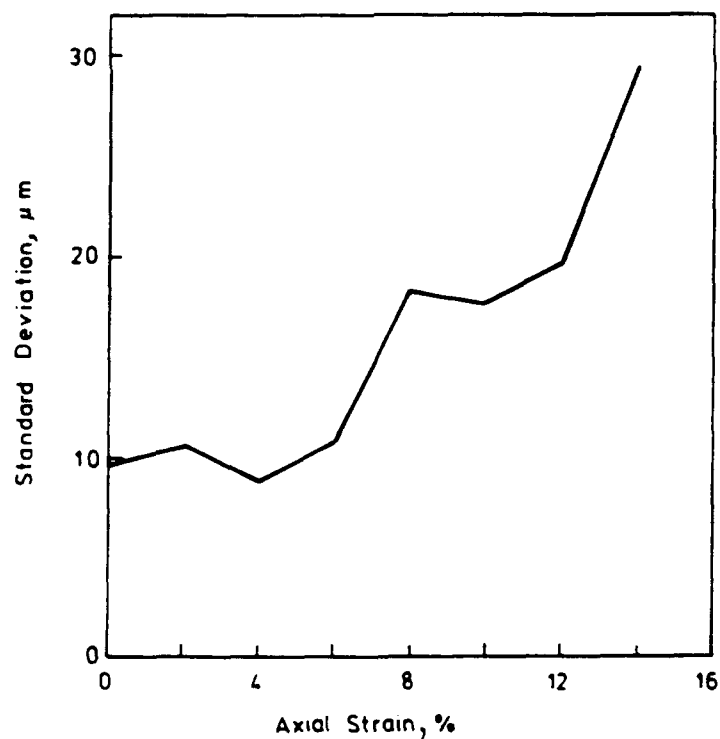(PMPA, POLMAP, POLMAP4 ncu).

Fig. 7.14 Between-samples standard deviation of size of patches vs. Axial
strain (POLMAP4 ncu).

Appendix 1

PUBLICATIONS ARISING FROM THIS GRANT

The following publications and other reports arose directly or indirectly from AFOSR 87-0346.

Bai, X. 1992. *Microstructural deformation of clay.* Glasgow Ph.D. Thesis.
Bai, X. 1993. *Microstructural deformation of clay.* Geotechnique 43. 343.
Bai, X., Smart, P., and McConnachie, I. 1991. *Mapping clay microstructure.* Supplement to Proceedings of Royal Microscopical Society vol.27 no.1 p.19.
Bai, X., Smart, P., and Leng, X. In press. *Polarising microphotometric analysis.* Geotechnique.
Bai, X., Smart, P., and Leng, X. In preparation. *Microstructural deformation of undrained kaolin.*
Costa, L. da F., Leng, X., Sandler, M.B., and Smart, P. 1991a. *Semi-automated analysis of clay samples.* Review of Scientific Instruments 62. 2163-2166.
Costa, L. da F., Leng, X., Sandler, M.B., and Smart, P. 1991a. *Analysis of clay microstructure by transputer.* Applications of Transputers 3 vol.1 pp.317-322. IOS Press, Amsterdam.
Hounslow, M.W., and Tovey, N.K., In press. *Segmentation of pores in back-scattered images of sediments and soils, and their relationship to domain structure.* Scanning Microscopy Supplement 6.
Leng, X. 1992. *Analysis of some textured images by transputer.* Glasgow Ph.D. Thesis.
Leng, X. 1993. *Analysis of some textured images by transputer.* Geotechnique 43. 345.
Leng, X., Hounslow, M.W., Bai, X., Luo, D., Costa, L. da F., Xue, X., Tovey, N.K., and Smart, P. 1993. *Image analysis of clay microstructure.* Proc. Conf. Image Processing: Applications in Civil Engineering, Hawaii. National Engineering Federation, New York. In press.
Leng, X., and Smart, P. 1991. *Improved methods of textural analysis.* Applications of Transputers 3 vol.1 pp.323-328. IOS Press, Amsterdam.
Leng, X., and Smart, P. 1992a. *Preferred orientation in three dimensions.* Report. Civil Engineering Department, Glasgow University, Glasgow G12 8QQ.
Leng, X., and Smart, P. 1992b. *Image analysis of clay scanning electron micrographs.* Proc. 13 Int. Cong. X-ray Optics and Microanalysis. Manchester. Inst. Phys. Conf. Ser. No.130 Chapter 5 pp.371-374.
Luo, D., MacLeod, J.E.S., Leng, X., and Smart, P. 1992. *Automatic orientation analysis of particles of soil microstructures.* Geotechnique 42. 97-107.
Smart, P. 1991. *Microstructural classification of clayey sediments.* Geo-Marine Letters 11. 170-171.
Smart, P., and Leng, X. 1990a. *Textural analysis by transputer.* Applications of Transputers 2 pp.240-247. IOS Press, Amsterdam.
Smart, P., and Leng, X. 1990b. *Topcontouring programs.* Report. Civil Engineering Department, Glasgow University, Glasgow G12 8QQ.
Smart, P., and Leng, X. 1991. *Textural analysis by transputer.* SERC/DTI Transputer Loan Initiative Reports 10, 1-15. SERC. Didcot.
Smart, P., and Leng, X. 1992. *Textural analysis.* Image Processing by Transputer Chapter 4 pp.73-95. IOS Press, Amsterdam.

Smart. P.. and Leng, X. 1993. *Present developments in image analysis. Scanning Microscopy. In press.*

Smart. P.. Leng, X., and Bai. X. 1992. *Image analysis of soil microstructure.* Géotechnique et Informaqtique. Colloque International. Paris. pp.905-912. Presses de l'Ecole National des Ponts et Chausses. Paris.

Smart. P., and Tovey, N.K. 1987. *Microanalysis of deformation of soils.* AFOSR Soil Mechanics Seminar. Boston. pp.9-12.

Smart. P., and Tovey, N.K. 1988. *Theoretical aspects of intensity gradient analysis.* Scanning 10. 115-121.

Smart. P., and Tovey, N.K. 1988. *Microfabric of the deformation of soils.* 1st Annual Report AFOSR 87-0346. 44 pp. plus 2 reprints.

Smart. P., and Tovey, N.K. 1989. *Microfabric of the deformation of soils.* 2nd Annual Report AFOSR 87-0346. 41 pp. plus 1 reprint.

Smart. P., and Tovey, N.K. 1991. *Microfabric of the deformation of soils.* 3rd Annual Report AFOSR 87-0346. 65 pp. plus 3 reprints.

Smart. P., and Tovey, N.K. 1992. *Microfabric of deformation of soils.* AFOSR Contractors' Meeting Particulate Mechanics Subarea. Albuquerque pp.16-19.

Smart. P.. and Tovey, N.K. 1993. *Microanalysis of deformation of soil.* US AFOSR Particulate Mechanics Research Task Summaries Project 2302C p.24.

Smart. P.. Tovey, N.K.. Hounslow. M.W.. Leng, X.. and Bai. X. In preparation. *Microstructural deformation of drained kaolin.*

Smart. P.. Tovey, N.K.. Leng, X., Hounslow. M.W.. and McConnachie. I. 1988. *Automatic analysis of microstructure of cohesive sediments.* Microstructure of fine-grained sediments. (Proc. NORDA Workshop. Stennis Space Centre). pp.359-366. Springer Verlag. New York. 1991.

Tovey, N.K. 1990. *Compaction. deformation and translocation: engineering applications. Microfabric in soils under load: image analysis.* European Training Course on Soil Micromorphology, pp.19-33. Winand Staring Centrum. Wageningen.

Tovey, N.K. 1991a. *Microfabric of Hong Kong Marine soils.* Microstructure of fine-grained sediments. (Proc. NORDA Workshop. Stennis Space Centre). pp.519-530. Springer Verlag, New York. 1991.

Tovey, N.K. 1991b. *New algorithms for image analysis of fibrous materials.* Proc. European Research Symposium on Image Analysis for Pulp and Paper Research and Production. Grenoble pp.10-1 to 10-3.

Tovey, N.K. 1990. *Compaction. deformation and translocation: engineering applications. Microfabric of soils under load: image analysis.* International Training Course on Soil Micromorphology. pp.143-157. Agricultural University, Wageningen.

Tovey, N.K. 1992. *Evidence from soil microfabric and mineralogy.* The Logging and Interpretation of Transported Soils in Offshore Boreholes pp.49-60. Gelolgical Society of Hong Kong.

Tovey, N.K., Dent, D.L., Krinsley, D.H., and Corbett, W.M. In press. *Processing multi-spectral SEM images for quantitative microfabric analysis.* Scanning Microscopy Supplement 6.

Tovey, N.K., Dent, D.L., Krinsley, D.H., and Corbett, W.M. 1993. *Quantitative micro-mineralogy and microfabric of soiikls and sediments.* Proc. 9 International Meeting on Soil Micromorphology, Townsville, Australia. In press.

Tovey, N.K., and Krinsley, D.H. 1990. *A technique for quantitatively assessing orientation patterns in sand grain microtextures.* Bull. Int. Assoc. Eng. Geol. 41, 117-127.

Tovey, N.K., and Krinsley, D.H. 1991. *Mineralogical mapping of scanning electron micrographs.* Sedimentary Geology 75, '09-123.

Tovey, N.K., and Krinsley, D.H. 1992. *Mapping the orientation of fine-grained minerals in soils and sediments.* Bull. Int. Assoc. Eng. Geol. 46, 93-101.

Tovey, N.K., and Martinez, M.D. 1991. *A comparison of different intensity gradient formulae for orientation analysis of electron micrographs.* Scanning 13. 289-298.

Tovey, N.K., and Smart, P. 1986. *Intensity gradient techniques for orientation analysis of electron micrographs.* Scanning 8. 75-90.

Tovey, N.K. Smart, P., and Hounslow, M.W. 1989a. *Quantitative orientation analysis of soil microfabric.* Soil Micromorphology pp.631-639. Elsevier.

Tovey, N.K. Smart, P., and Hounslow, M.W. 1993. *Quantitative methods to determine microporosity in soils and sediments.* Proc. 9 International Meeting on Soil Micromorphology, Townsville, Australia. In press.

Tovey, N.K. Smart, P. Hounslow, M.W., and Desty, J.P. 1991a. *Automatic orientation analysis of microfabric.* Scanning Microscopy Supplement 6. In press.

Tovey, N.K. Smart, P. Hounslow, M.W., and Leng, X. 1989b. *Practical aspects of automatic orientation analysis of micrographs.* Scanning Microscopy 3. 771-784.

Tovey, N.K. Smart, P. Hounslow, M.W., and Leng, X. 1991b. *Automatic domain mapping of certain types of soil fabric.* Geoderma 53. 179-200.

-----ooooo0ooooo-----

Appendix 2

OTHER REFERENCES

Andrawes, K.X., Krishnamurthy, D.N., and Barden, L. 1975. *Fabric changes during deformation of oriented clays.* Proc. 1 Baltic Conf. Soil Mech. Found Eng. 15-23.

Bates, R.H.T., and McDonnell, M.J. 1986. *Image restoration and reconstruction.* Oxford University Press, Oxford.

Bondarik, G.K., Berexinka, G.M., Tsareve, A.M., and Ierusalimskaya, E.N. 1970. *Deformation and texture of water-saturated clay soils.* Proc. 1 Internat. Cong. Eng. Geol. 1, 165-179.

Dickson, J.W., and Smart, P. 1976. *Some interactions between stress and microstructure of kaolin.* Modification of Soil Structure (Proc. Meet. Comm. 1 IInt. Soc. Soil Sci.. Adelaide) pp.53-57. Wiley, Chichester.

Gonzalez, R.C., and Wintz, P. 1987. *Digital image processing.* Addison-Wesley. Menlo Park, California.

Guan, L., and Ward, R.K. 1989. *Restoration of randomly blurred images by the Wiener filter.* IEEE Transactions of Acoustics, Speech and Signal Processing 37. 589-592.

Kohler, R. 1981. *A segmentation system based on thresholding.* Computer Graphics and Image Processing 15. 319-338.

Lewis, B.L., and Sakrison, D.J. 1975. *Computer enhancement of scanning electron micrographs.* IEEE Transactions: Circuits and Systems C-22, 267-278.

Joyce Loebl. 1985. *Image analysis - principles and practice.* Joyce Loebl Ltd., Gateshead.

McConnachie, I., 1974. *Fabric changes in consolidated kaolin.* Geotechnique 24, 207-222.

McKyes, E., and Yong, R.N. 1971. *Three techniques for fabric viewing as applied to shear distortion of a clay.* Clays Clay Min. 19, 289-293.

Mitchell, J.K. 1956. *The fabric of natural clays and its relation to engineering properties.* Proceedings of the Highway Research Board 35, 693-713.

Omer, B.M.A. 1978. *A study of a layered clay from Grangemouth.* Glasgow Ph.D. Thesis.

Proctor, J. 1975. *A statistical analysis of consolidated kaolin.* Glasgow M.Sc. Thesis.

Shibakova, V.S. 1970. *Effect of clay texture upon its shearing strength.* Proc. 1 Internat. Cong. Eng. Geol. 1, 419-435.

Smart, P. 1966a. *Optical microscopy and soil structure.* Nature 210, 1400.

Smart, P. 1966b. *Particle arrangements in kaolin.* Proc. 15th National Conference on Clays and Clay Minerals pp. 241-254.

Smart, P. 1966c. *Soil structure, mechanical properties and electronmicroscopy.* Cambridge Ph.D. Thesis.

Smart, P. 1985. *Optical microscopy in geotechnical engineering.* Presented at Int. Working Meeting on Soil Micromorphology. Paris.

Smart, P. 1993. *Microstructure, manipulation.* Encyclopedia of Soil Science. Part 1. 2nd Edition. Dowden, Hutchinson and Ross. Stroudsburg. Pennsylvania.

Smart, P., and Dickson, J.W. 1979. *Deformation and shear of normally consolidated flocculated kaolin.* Mechanisms of Deformation and Fracture. Proc. Interdisciplinary Conf., Luleå pp.129-136. Pergammon, Oxford.

Smart, P., and Tovey, N.K. 1981. *Electron microscopy of soils and sediments: examples.* Oxford University Press, Oxford.

Smart, P., and Tovey, N.K. 1982. *Electron microscopy of soils and sediments: techniques.* Oxford University Press, Oxford.

Stroke, G.W., Haliou, M., Saffir, A.J., and Evins, D.J. 1971. *Resolution enhancement in scanning electron microscopy by a posteriori holographic image processing.* Scanning Electron Microscopy 1971, 57-64.

Tchalenko, J.S. 1967. *Influence of shear and consolidation on the microscopic structure of some clays.* University of London Ph.D. Thesis.

Tovey, N.K. 1980. *A digital computer technique for orientation analysis of micrographs of soil fabric.* J. Micros. 120, 303-315.

Webster, R., and Oliver, M.A. 1990. *Statistical methods in soil and land resource survey.* Oxford University Press, Oxford.

Wu, T.H. 1958. *Geotechnical properties of glacial lake clays.* Proc. Am. Soc. Civil Eng. 84, SM3, 1732-1 to 1732-34.

-----ooooooOooooo-----